NORTHWESTERN UNIVERSITY

MICRO/NANOSCALE FRICTION

AND

APPLICATION OF SURFACE WETTABILITY IN MEMS

A DISSERTATION

SUBMITTED TO THE GRADUATE SCHOOL
IN PARTIAL FULFILLMENT OF THE REQUIREMENTS

for the degree

DOCTOR OF PHILOSOPHY

Field of Department of Mechanical Engineering

By

BO HE

EVANSTON, ILLINOIS

December 2008

ABSTRACT

Micro/Nanoscale Friction and Application of Surface Wettability in MEMS

Bo He

Micro/nanoscale friction behavior has drawn a great deal of attention because it can reveal friction behavior at the interface level and ultimately lead to the discovery of the origin or real mechanism of friction. Surface wettability is an important property of solid surfaces and has been widely used in fundamental material research for surface characterization. Significant progress has been made in both research areas owing to the development of modern fabrication and surface characterization techniques.

One part of the work reported in this dissertation experimentally investigates the micro/nanoscale friction behavior of Ag-Bi alloys at elevated temperatures using nanoindentation-scratching techniques. Friction measurements have been conduced in both steady-state and transient thermal environments. The steady-state friction results are correlated with the material hardness obtained at each corresponding temperature. The transient friction measurements depict distinct friction transition behavior at the melting point due to different alloy compositions. A critical bismuth composition is experimentally identified.

Surface texture effects on friction at the macro- and microscales are studied using nanoindentation-scratching techniques on a polymer surface. It is found that surface textures significantly reduce friction due to reduced contact area at the macroscale, while this effect is less profound at the microscale. Friction on substrates with anisotropic textures is investigated

and correlated with numerical simulation results.

This dissertation research also develops theoretical models of the contact angle on rough hydrophobic surfaces, and conducts matching experiments. Three major aspects have been covered: multiple equilibrium energy states, contact angle hysteresis, and contact angle anisotropy. The matching experiments agree with the theoretical predictions and lead to a design criterion for a robust superhydrophobic surface. A novel MEMS device, a roughness switchable membrane device, is then designed based on the theoretical analysis. It consists of a thin poly(dimethylsiloxane) (PDMS) membrane bonded on the top of a rough PDMS substrate. Contact angle measurements have been conducted on the device surface, which demonstrates that the surface wettability can be switched from medium hydrophobic to superhydrophobic through pneumatic actuation.

DEDICATION

I dedicated this dissertation to my family, especially to my wife Yan Xie. Without her understanding and support, most of all love, the completion of this work would not have been possible.

ACKNOWLEDGMENTS

I would first like to express great thanks to my advisor, Dr. Jane Wang. She is the one that recruited, trained and released me with all the professional skills I have today. Dr. Wang sets only the highest standards for herself, and is fully dedicated to hard work and to new ideas in science and technology. This is the mark of a true scientist. Not only has Dr. Wang given me endless help in my research, she has also guided me in both my personal and professional life. I will never forget that it was Dr. Wang who helped me get through the hardest time in my life in 2003. Her encouragements ignite my motivations in science as well as in my everyday life, and will continue to drive me until the day I finally finish my studies.

I am also grateful to Dr. Junghoon Lee and my co-advisor Dr. Neelesh Patankar. It was Dr. Lee who helped me get admitted and get my graduate assistantship, giving me the chance to come to Northwestern University to pursue my doctorate degree. I also benefited tremendously from the experience of working with Dr. Patankar. His rich theory and rigorous logic served for me as an example of what a scientist should be.

I would also like to thank my committee members, in particular Dr. Yip-Wah Chung, for their invaluable help. Dr. Chung is an amazing scholar. Whenever I have turned to him with research problems, he has always been able not only to provide the answers I am looking for, but also to explain them in a way that is simple and easy to understand.

Many thanks go to my colleagues and friends. Dr. Jae-Hyun Chung, who is now a professor at University of Washington, has been of utmost importance to me. Being my first friend at Northwestern University, he not only helped me acclimate to the new circumstance but

also gave me many useful suggestions in my research. I also want to thank Dr. Xinqi Chen, Dr. Shaoning Lu, Mr. Hualong Yu, Mr. Wei Chen, and Mr. Peng Liu. Their help and friendship are invaluable.

Finally, I would like to express my infinite gratitude to my family for their support and understanding. My parents frequently called me from overseas and their encouragement and advice guided me through many difficulties. Most importantly of all, none of this would have been possible without my wife, Yan Xie, who knows me best and has shared the rainy and sunny days with me throughout all the years of my study.

TABLE OF CONTENTS

LIST OF TABLES

LIST OF FIGURES

CHAPTER ONE: INTRODUCTION

1.1 Introduction

Nanoindentation is a common technique for measuring mechanical properties of surfaces and thin films. In a typical nanoindentation experiment, one obtains a plot of the load versus indentation depth (loading and unloading), from which material properties such as Young's modulus and hardness can be obtained, using the known geometry of the indentation tip. This depth sensing indentation technique, based on Oliver and Pharr's work [1], can determine material properties without measuring the contact area precisely by using imaging techniques such as atomic force microscopy (AFM) and scanning electron microscopy (SEM).

Most nanoindentation systems are designed to allow lateral translation of the tip. In this way, scratch and friction experiments can be performed at the nano- and microscales [2-9]. These types of experiments can be used, for example, to test wear-resistant coating [10-14], conduct indentation creep studies [15-17], or determine material fatigue behavior [18-20].

In engineering applications, surfaces of many components are subject to both environmental temperature and frictional heating. The latter often occurs at the asperity level and may result in a dramatic change in the surface contact status [21-22]. Due to the lack of appropriate high-temperature instrumentation, most of the friction data in existing literature has been acquired at room temperature and on the macro level. Data regarding asperity level (micro-meter and nano-meter scales) friction at elevated temperatures is missing from current literature.

Surface textures have been used in engine components [23-24] and mechanical seals [25-26]. Many studies have shown that surface textures can retain oil and entrap wear particles [27-

29]. For hydrodynamic lubrication in particular, surface textures may support the formation of lubricating oil film [30-33]. At the nano/microscale when adhesive forces are significant, surface textures can help lower friction by reducing the real area of contact [34-36].

Friction anisotropy can be defined as the dependence of friction on the structure of the surfaces and their orientation to one another, or to the sliding direction. Most of the data in open literature describes friction anisotropic behavior at the atomic scale; however, data concerning this phenomenon at the macro scale is included in the work done by Singh *et al.* and Menezes *et al*. [37-38], in which it was reported that friction anisotropy is observed on ground metallic surfaces under lubricating conditions, which attributes to the surface texture effect on lubricant flow and pressure. Here, the friction anisotropy work at the atomic scale is summarized as a reference.

When two surfaces are brought into contact with each other, the interfaces undergoes either elastic or plastic deformation. Under elastic deformation condition, surface lattice commensurability, or alignment of the surface atomic lattices with respect to one another is the primary cause of friction anisotropy [39-41]. It has been demonstrated under plastic deformation condition, bulk properties of the crystal lattice such as the orientation of slip planes or anisotropy of the bulk mechanical properties leads to friction anisotropy [42-43]. Carpick *et al*. hypothesize that the large friction anisotropy observed on N-(2-ethanol)-10, 12-pentacosadiynamide (PCEA) monolayer film is due to anisotropic film stiffness [44-45].

Wettability is one of the most important properties of solid surfaces, and is often used in fundamental material research to characterize a surface. Many applications, such as the manipulation of the hydrophobic interactions in protein adsorption [46], surface-tension-induced microfluidic manipulation [47-48], and reduction of fluid resistance [49], make use of this

property. The wettability of a solid surface is affected by two factors: surface energy and surface roughness. Surface energy is an intrinsic property of a material that can be controlled by chemical modification, such as fluorination [50]. The focus of this study is on the other factor that can affect wettability – surface roughness.

The effect of surface roughness on wettability and, in particular, on contact angle was modeled more than half a century ago [51-52]. The two well known theories, Cassie and Wenzel's theories, predict different contact angles for a droplet on the same rough surface. Neither the aforementioned experiments nor previous literature are conclusive regarding which of the two theories correctly models the contact angle on a rough surface. Patankar's latest analysis shows that both cases are possible on the same rough surface, corresponding to the two different formulas [53].

Superhydrophobic surfaces not only have a high contact angle (>150°), but also offer minimum contact angle hysteresis so that water drops are almost spherical on these surfaces and can easily roll off. This is usually referred to as the lotus effect, as it is known from experiments with lotus leaves that a Cassie drop shows less hysteresis than a Wenzel drop [54]. Thus, it is important to design superhydrophobic rough surfaces in such a way that a Cassie drop is formed, as a Wenzel drop is expected to show much larger hysteresis due to the wetting of the grooves [55-56]. Johnson & Dettre hypothesized, based on the principle of energy barriers, that a Cassie drop should have lower contact angle hysteresis compared to a Wenzel drop. This was qualitatively supported by their experiments with roughened wax surfaces [57].

When a droplet resides on a superhydrophobic surface, one of the two things can happen. If the roughness geometry is isotropic, the drop shape is almost spherical and the contact angle of the drop with the rough surface is nearly uniform along the contact line; if the roughness

geometry is not isotropic, i.e., parallel grooves, then the contact angle is no longer uniform along the contact line. Bico *et al*. reported that the contact angles observed perpendicular and parallel to the direction of the grooves are different. The exact mechanism for anisotropic wetting and the resultant shape of the drop was not discussed [58].

The ability to control surface wettability, and hence surface tension force, promises a powerful actuation mechanism for micro-electro-mechanical systems (MEMS) because of the large magnitude of the surface tension force, compared to pressure or inertia force, at micro scale. Recently, much attention has been paid to its possible applications in microfluid handling technique. Many novel devices have been reported, notable examples being a liquid-based micro optical switch which is operated by thermally induced surface tension difference (thermocapillary effect) [59]; a liquid handling system which can move micro scale liquid metal droplets by the electrical control of surface tension (electrocapillary effect) [47-48]. However, there are apparent disadvantages of using the above mechanisms in many applications. The optical switch needs considerable power to generate enough surface tension difference to move the liquid. In the rotating liquid micromotor, the electrical potential may affect particles such as biomolecules in the solution.

1.2 Research Overview

This dissertation summarizes my work in two areas: first, investigation of nano/microscale melting and texture effect on friction; second, modeling of microscale surface wetting and its application in MEMS. It is organized in the following format:

In Chapter Two, high-temperature friction behavior at nano/microscales is investigated

using nanoindentation-scratching techniques. The micro-melting effect on friction of silver-bismuth alloys is studied. It is found that the molten materials serve different functions depending on alloy compositions. A critical bismuth composition is experimentally determined, below which the molten material can hardly reduce friction at the nano/microscales.

Chapter Three presents a study of the surface texture effect on friction of poly(dimethylsiloxane) (PDMS) at both macro- and microscales. Friction reduction observed on textured surfaces can be attributed to reduced contact area. JKR analysis reveals that the adhesion force has less effect on contacts under higher normal loads. Friction anisotropic behavior is identified and possible mechanisms are discussed.

Chapter Four investigates three major aspects of hydrophobic contact angles on rough substrates: multiple equilibrium energy states, contact angle hysteresis, and contact angle anisotropy. Theoretical predictions are compared with matching experiments. The analysis of multiple equilibrium energy states leads to the establishment of a design criterion for a robust hydrophobic rough surface on which the contact angle will not change as a result of an external disturbance. The study of contact angle hysteresis and anisotropy helps develop a better understanding of wetting mechanisms. Methodologies are then proposed to quantify hydrophobic contact angles on rough substrate.

Chapter Five describes a roughness based wettability switchable membrane device for hydrophobic surfaces. The device is made using microfabrication techniques and consists of a thin poly(dimethylsiloxane) (PDMS) membrane bonded on the top of a rough PDMS substrate. It is demonstrated that the surface wettability of the membrane device can be switched from a medium hydrophobic to a superhydrophobic state by deflecting the membrane using a pneumatic

method. This technology could enable a microscale liquid droplet transport mechanism by surface roughness effect without using thermocapillary or electrocapillary effect.

CHAPTER TWO: NANO/MICROSCALE HIGH TEMPERATURE FRICTION

2.1 Introduction

Surface tribological properties are significant factors that need to be considered in the design of machine components under relative motion. In engineering applications, many tribological components, such as engine bearings, are subject to both environmental temperature and frictional heating. The latter often occurs at the asperity level and may result in a non-uniform surface modification [21-22]. This dramatic change in contact conditions can greatly influence the surface tribological performance.

Yield strength and hardness of most materials are temperature-dependent [60-67]. Therefore, the interface of machine components subject to high temperatures may behave much differently from that at room temperature. Failure to take material behavior at service temperature into account can lead to a significant performance reduction or even a failure.

In the past two decades, owing to the development of new sensors and actuators that allow instrumented indentations to be routinely performed on a submicron scale, nanoindentation-scratching technique has become ubiquitous for mechanical property measurements of surfaces. Investigation of the material behavior at the asperity level (nano- and microscales) can reveal its origin and the associated phenomena.

However, most of the measurements carried out using nanoindentation have been limited to room temperature because instruments for slow measurement of nanoscale displacements are

generally highly sensitive to thermal expansion. There is little data in the open literature about nano/microscale friction at elevated temperatures mainly due to the lack of appropriate instrumentation. In this work, a recently developed nanoindentation-scratching system, NanTest 600 (Micro Materials Ltd, UK), was utilized, which enables high temperature operations of indentation and scratch tests.

2.2 Background

2.2.1 Nanoindentation

Indentation methods are the most commonly applied means to test the mechanical properties of materials. Traditionally, a hard indenter is pressed into the specimen surface with a known force, and the hardness is estimated using the applied force divided by the projected area.

Hardness = Force / Area

Thus indentation involves the imaging of the residual indent to determine the area of the contact. At the small scale, the size of the residual impression is often only a few microns, which makes it very difficult to obtain a direct measure using optical techniques. A Scanning Electron Microscope (SEM) or Atomic Force Microscope (AFM) can be used to measure the area of contact; however, they are both time consuming processes, as it is difficult to find and image a sub-micrometer indent [68].

The development of nanoindentation using a depth-sensing method can overcome the above-mentioned obstacles. Using this method, load and displacement of the indenter are continuously recorded during the indentation. Oliver and Pharr first proposed a method (hereafter referred to as Oliver-Pharr method) to calculate hardness and elastic modulus by

analyzing the data recorded during the indentation process [1]. Figure 2.1 shows a typical load-depth curve of an indentation test. h_c, h_{max}, and h_o denotes the contact depth, maximum depth, and the corresponding depth when the tangential line of the unloading curve at the maximum load intersects with the displacement-axis, respectively.

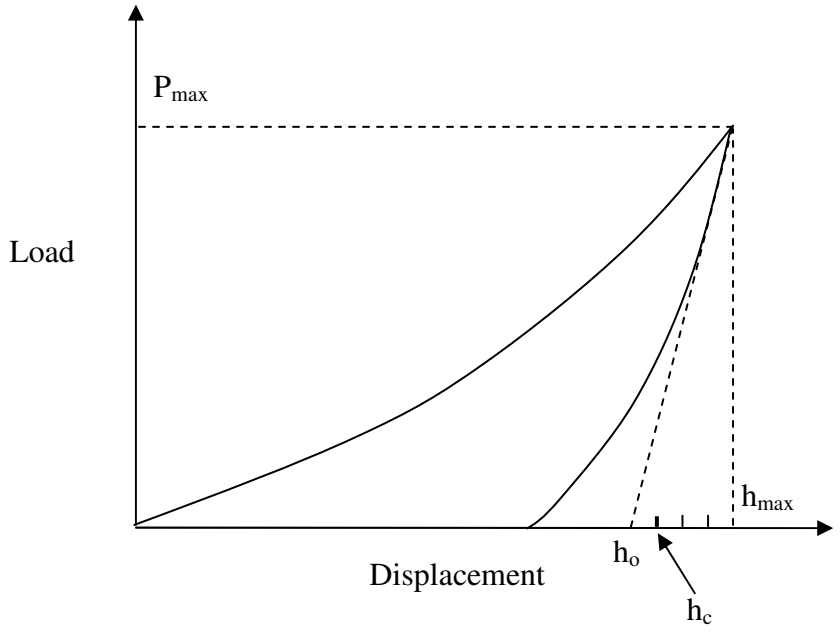

Figure 2.1 Schematic plot of a typical load-displacement curve

The Oliver-Pharr Method uses a polynomial to approximate the unloading curve. The contact depth h_c is determined using the following formula [1]:

$$h_c = h_{\max} - \varepsilon(h_{\max} - h_o) = h_{\max} - \varepsilon \frac{P_{\max}}{(dP/dh)\big|_{\max}} \tag{2.1}$$

ε is 0.75 for a three-sided pyramid Berkovich tip. $(dP/dh)\big|_{\max}$ is the slop of the unloading curve at the maximum load, which is defined as the stiffness of the contact. Once the contact depth is determined, the known geometry of the indenter then allows the size of the area of contact to be determined. This procedure also allows for the Young's modulus of the specimen material to be obtained from the measured contact stiffness.

$$S = \left.\frac{dP}{dh}\right|_{\max} = 2E^* \sqrt{\frac{A_c}{\pi}} \tag{2.2}$$

where A_c is the contact area and E^* is the reduced modulus given by

$$\frac{1}{E^*} = \frac{1-\nu_{tip}^2}{E_{tip}} + \frac{1-\nu_{sample}^2}{E_{sample}} \tag{2.3}$$

where υ is the Poisson ratio.

To summarize, hardness and modulus can be determined using the following two equations:

$$H = \frac{P_{\max}}{A_c} \tag{2.4}$$

$$E^* = \frac{1}{2}\frac{\sqrt{\pi}}{\sqrt{A_c}}\left.\frac{dP}{dh}\right|_{\max} \tag{2.5}$$

Since the total (measured) compliance = contact compliance + machine compliance, the machine compliance must be subtracted from the data for accurate mechanical property measurement. The machine compliance can be measured by indenting a standard sample with known material properties such as fused silica.

As previously discussed, the real area of contact is determined by knowing the geometry of the indentation tip. The area function of the indentation tip can be obtained using the Oliver

and Pharr iterative method, which involves indenting the standard fused silica sample at a range of maximum loads.

Many different phenomena can occur under the indenter, and are arbitrarily divided into two categories: material-based and geometry-based [68].

Material-based phenomena include:

- Pile-up/Sink-in → ratio of yield strength to stiffness
- Phase transformation
- Dislocation
- Time dependent effects such as creep and viscoelasticity
- Fracture

Geometry-based phenomena include:

- Effect of surface roughness
- Effect of inhomogeneities: thin films/multi-phase materials
- Indentation size effect

2.2.2 High Temperature Nanoindentation-Scratching System

As previously mentioned, mechanical property measurements on a small scale have been limited to room temperature. One factor responsible for this is that in most nanoscale instruments the displacement transducer is placed above the specimen, thus leading to unacceptably high thermal drift at higher temperatures.

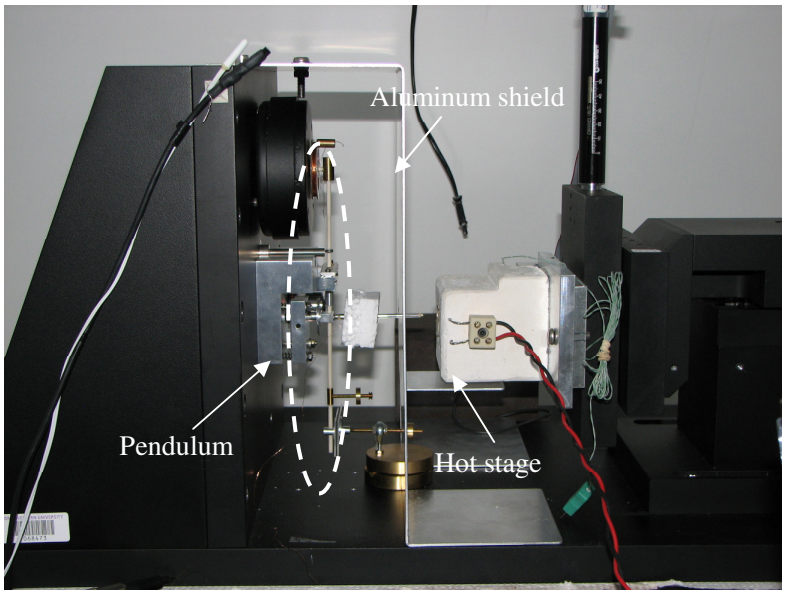

(a) Experiment set-up

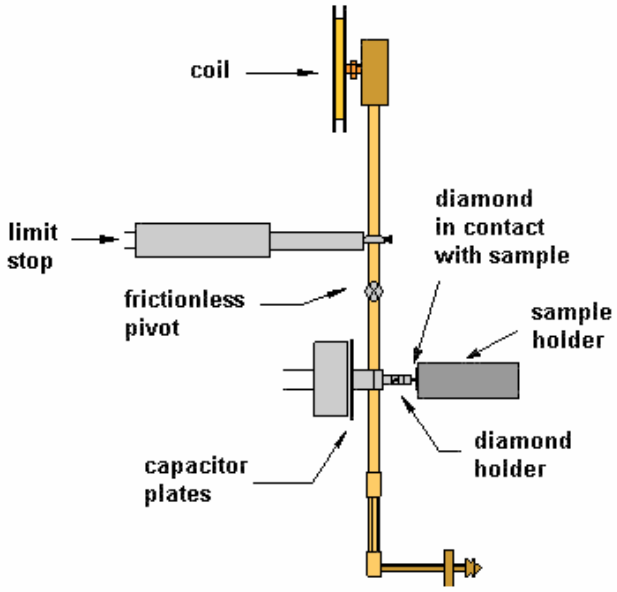

(b) Schematic of the pendulum system

Figure 2.2 Schematic of the NanoTest pendulum system in contact with a sample [69]

The nanoindentation system used in this work obviates this problem using a novel transducer arrangement as shown in Figure 2.2, where the specimen is mounted vertically, opposite to the displacement transducer. This arrangement allows the heated zone to be above the highly sensitive displacement transducer and thus greatly minimizes thermal drift. The entire system is mounted on top of an air table inside a cabinet in order to avoid environmental vibration and minimize temperature drifting [69-70].

In indentation mode, a current in the coil causes the pendulum to rotate so that the diamond tip indents the sample surface. Displacement of the indentation tip is measured by means of the parallel capacitor. In scratching mode, the specimen moves parallel to the pendulum against the loaded indenter.

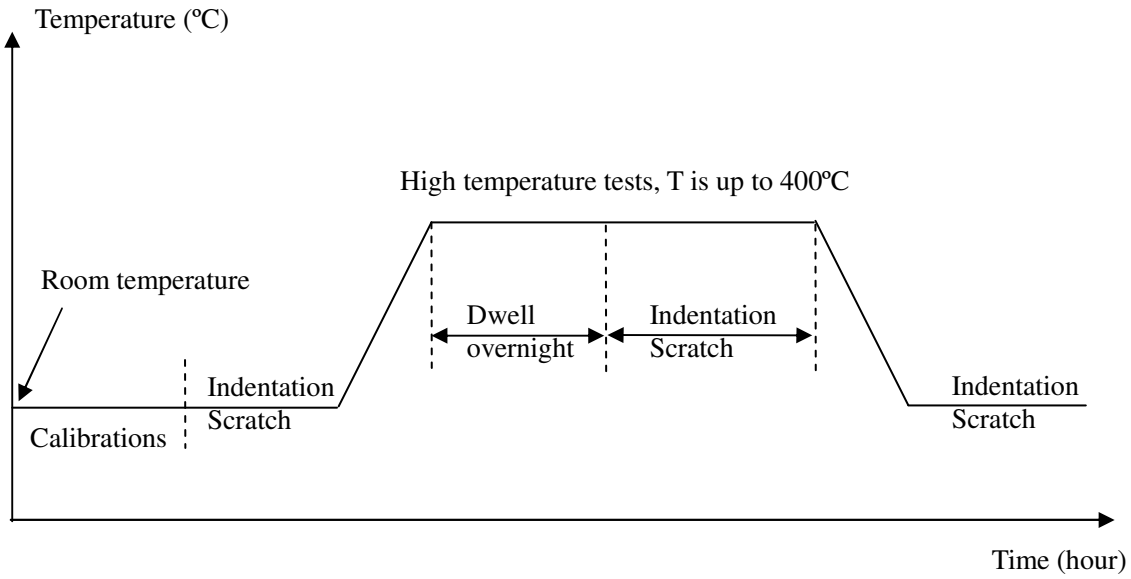

Figure 2.3 High temperature measurement procedures

In high temperature measurements, an aluminum shield is interposed between the pendulum and the hot stage to preclude any significant radiant heating of the pendulum. The diamond holder passes through a small hole in the aluminum plate in such a way that the close proximity of the two surfaces limits heating of the diamond holder (Figure 2.2 (a)). In indentation mode, both the indentation tip and sample stages are heated up to the same temperature, and thus heat flow between them does not occur upon contact. In scratching mode, the sample stage is heated up to the desired temperature and the scratching tip is brought into close proximity (25μm) and usually left overnight before experiments in order to reach the same temperature as the stage.

2.3 Experiment Details

Detailed operation procedures for the NanoTest system can be found in its manual. Figure 2.3 summarizes the operation procedures for high temperature indentation and scratch tests.

How accurately the friction value is obtained at elevated temperatures strongly depends on how thermal drift is minimized and accounted for in the data collected. In order to minimize the effect of thermal drift, the following methods have been applied: placing the sample vertically, using an aluminum thermal shield, and leaving samples at the desired temperature overnight before the experiment. To account for the remaining thermal effect in the data collected, two important calibration procedures are required: depth calibration in the indentation tests, and friction transducer calibration in the scratch tests.

For depth sensing indentation, with the known diamond area function, the real contact area is determined by tip penetration depth. In NanoTest 600, the depth calibration relates the

change in capacitance to a known distance moved by a sample in contact with the pendulum. Depth calibrations have been conducted at all working temperatures in the indentation tests in order to preclude any errors arising from possible small changes in equilibrium capacitor spacing at elevated temperatures. A thermal couple is glued near the sample on the hot stage and connected to a reading unit. The recorded temperature is hereafter referred to as the measured surface temperature and plotted as the X coordinates in Figure 2.4 and 2.6. Figure 2.4 shows the deviation of the depth calibration factors (unit in nm/bit) at elevated temperatures to the value at room temperature. It can be seen that the deviation is within 6% and therefore it can be concluded that the precautions taken greatly reduce thermal drift in high-temperature indentation tests. The calibration factors are applied to the penetration depth data obtained at the corresponding temperatures to account for the small thermal effect. It is noted that the depth calibration factors obtained at elevated temperatures are always smaller than that at room temperature. This suggests that other unknown factors that affect calibration results may remain in the system, which leaves the way open for possible future investigation.

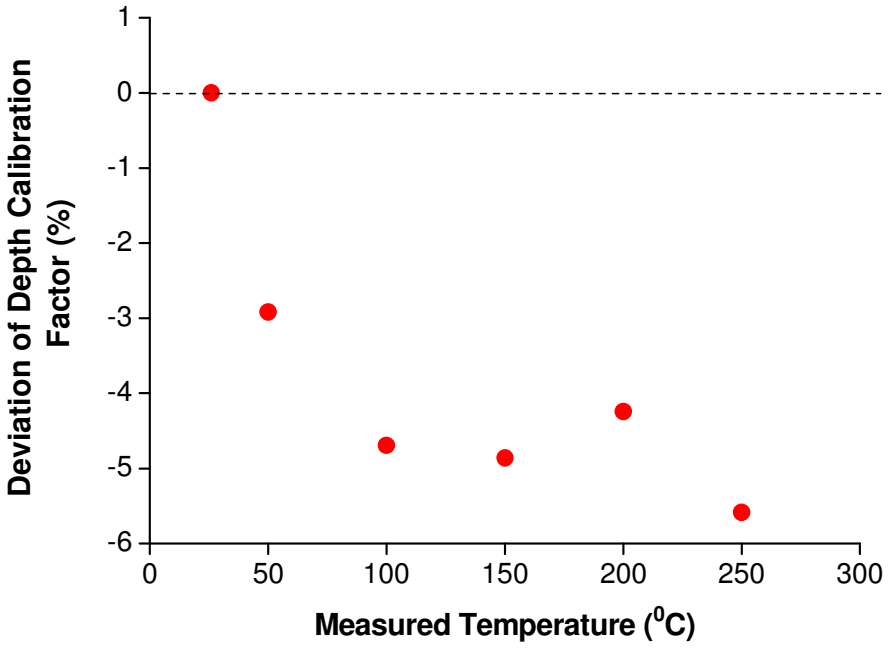

Figure 2.4 Deviations of the depth calibration factors at elevated temperatures to the value at room temperature

A different measurement setup (hereafter referred to as friction transducer) is used in the high temperature scratch tests as shown in Figure 2.5. Instead of connecting the tip directly to the pendulum, a Rockwell diamond tip is affixed using high temperature cement into one end of a quartz tube. The other end of the tube, onto which two piezoresistive sensors are attached, is connected to the pendulum through a diamond holder. Since both normal and transverse forces (friction) are recorded in the scratch tests, two separate measurement channels are needed in order to avoid cross-talk. In the measurement, the normal and transverse forces are measured by capacitive and piezoresistive sensors, respectively. The quartz tube also serves as an insulator to keep heat from the tip to the pendulum, and thus further reduces the thermal effect. Calibrations

of the friction transducer at elevated temperatures are conducted by hanging three different masses (known) at the end of the Rockwell tip in order to correlate the relation of the external force with the voltage reading given by the piezoresistive sensors. Figure 2.6 shows the maximum deviation of the calibration factor which is less than 8% to the value at room temperature. Thermal effect is thus greatly reduced, and the calibration factors are applied into the friction data collected at the corresponding temperatures to rectify the signal due to thermal effect. Again, it is observed that the friction transducer calibration factors obtained at high temperature are smaller than that obtained at room temperature.

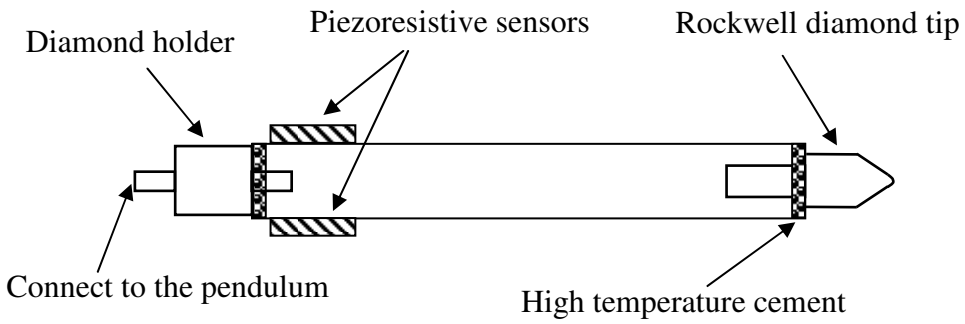

Figure 2.5 Schematic of the friction transducer for high temperature scratch tests

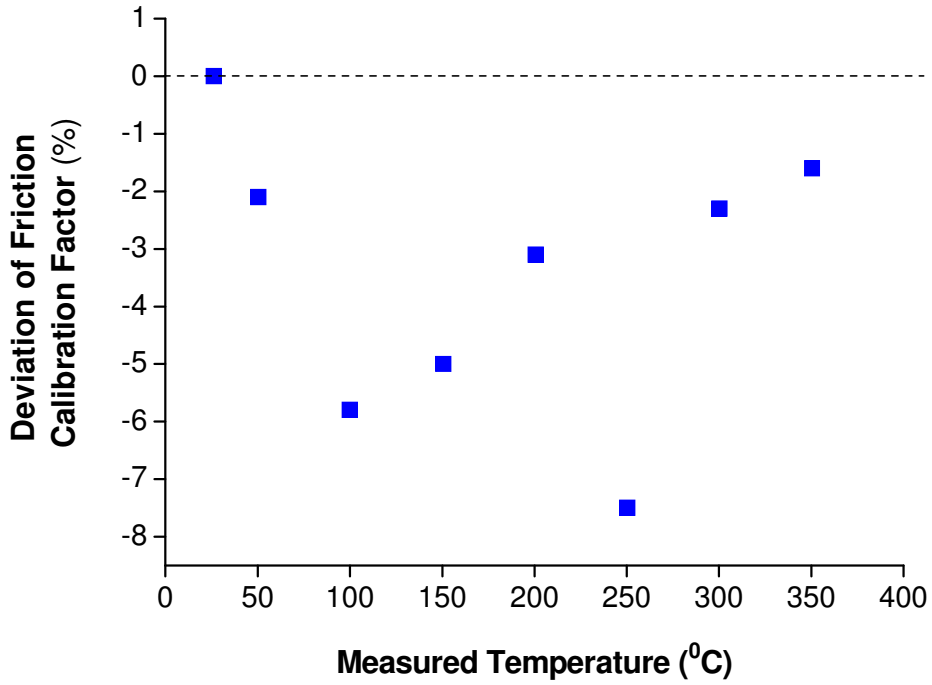

Figure 2.6 Deviations of the friction transducer calibration factors at elevated temperatures to the value at room temperature

2.4 Micro-Melting Effect on Friction of Low Melting-Point Ag-Bi Alloys

2.4.1 Introduction

The material interface of a friction pair may undergo a rise in temperature high enough to cause microscale or nanoscale melting. When such melting occurs, a liquid material appears in the interface, either continuously or discontinuously. Liquid metal/alloy has been utilized for interface friction reduction when the temperature is too high to use a conventional fluid lubricant [71-72]. In such cases, alloys with a low-melting temperature are attractive substitutes for lead-

based low-friction materials; however, scuffing, or even seizure, may also happen in such an interface. Melt lubrication is a sacrificial process; first, some part of a surface becomes soft, and then the liquid is free to move. Therefore, the demands for low frictional shear and high surface strength appear to be a dilemma. It is important to investigate how melting affects interface fiction in both transient and steady states, which is the information necessary for the development of new low-friction materials.

Low-melting alloys of tin, indium, or bismuth, are likely to be chosen for lead or lead-based alloy replacement. In the printed circuit board (PCB) industry, tin-silver-copper alloys have been developed as lead-replacement solder materials for electronic element assembly, for which solder joint strength, fatigue resistance and high temperature life should all be considered [73-75]. Many lead-free alloys with enhanced properties have been invented for automotive applications, such as high strength aluminum-tin alloys for engine bearings [76-78], and copper-tin-bismuth-molybdenum carbide bearing alloys for highly loaded engine bearings [79]. These alternative materials usually have a low melting phase.

Here, a systematic study of friction behavior, involving a group of silver-bismuth alloys with different compositions as liquid lubricants, is reported. Friction measurements are conducted under both ramping and constant temperature conditions, which simulate transient and steady-state thermal environments. The ramping temperature tests study the friction-temperature relationship, while the constant temperature tests investigate the relationship between friction behavior and microstructure and material properties. Hardness at different temperatures measured through indentations is correlated to the steady-state friction behavior of the materials. A friction transition at the melting point is identified and correlated to the alloys' phase transformation.

2.4.2 Experiment Description

Instrumentation

Most of the measurements reported in this work have been conducted using the high-temperature nanoindentation-scratching system (NanoTest 600, Micro Materials Ltd, UK). Details of the system can be found in the previous section.

Material and Methods

The nominal compositions of the three tested alloys (alloy 1-3) are listed in Table 2.1. The starting materials are pure (99.99 weight percentage) elements of silver and bismuth, both obtained from Alfa Aesar, Ward Hill, MA. Each alloy was made by melting in evacuated quartz tubes with inner diameter of 8 mm. Then, discs 2mm thick were cut from the as-solidified rods. Specimens for optical metallography were prepared by standard procedures. They were first grounded with a SiC sand paper down to 180 grit and then polished with 0.1μm diamond paste. Surface roughness was then characterized using a phase-shift interferometer (MicroXAM, ADE Phase-Shift, Tucson, AZ). Roughness results are given in Table 2.1.

Table 2.1 Composition and surface roughness of three Ag-Bi alloys before and after melting (magnification: 20, imaged area: 431.6μm×321.0μm)

	Composition weight percentage (%)		Surface roughness (original sample) R_q (nm)	Surface roughness (after melting) R_q (nm)
	Bi	Ag		
Alloy 1	97.5	2.5	84.9 ± 16.3	
Alloy 2	70	30	36.4 ± 5.6	
Alloy 3	50	50	55.2 ± 11.6	264.6 ± 62.1

Figure 2.7 shows the phase diagram [80] of the Ag-Bi system and the compositions of the three alloys tested. The eutectic temperature is 262.5℃. Alloy 1 is very close to the eutectic composition but is slightly bismuth-rich, and alloys 2 and 3 have a silver content of 30 and 50 wt.%, respectively. As given in the equilibrium phase diagram, alloy 1 melts completely at about 264˚C while alloys 2 and 3 start melting at 262.5˚C and remain in two-phase liquid+solid (silver) state till about 435˚C and 535˚C, respectively.

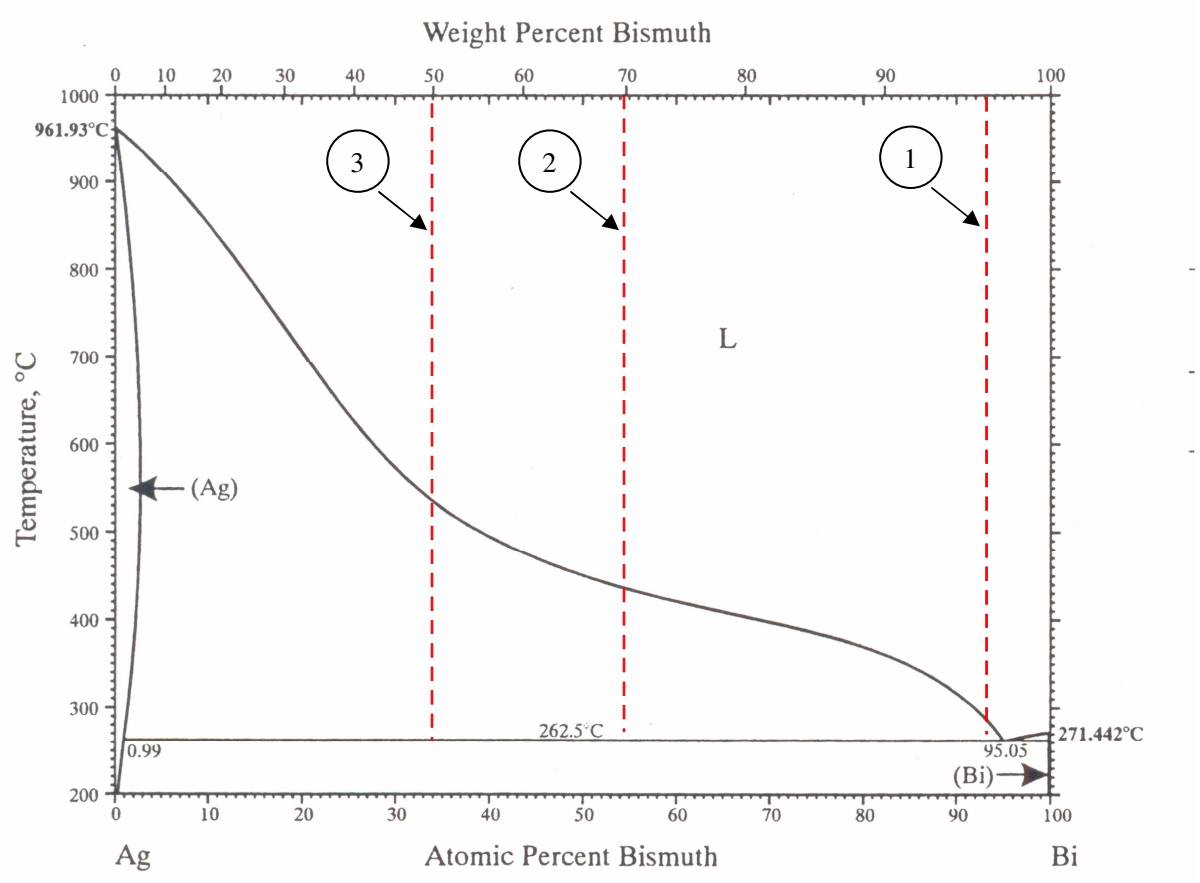

Figure 2.7 Ag-Bi alloy phase diagram and compositions of three alloys tested [80]

Friction testes were conducted using a Rockwell diamond tip (tip radius, R ≈ 25μm). The friction transducer was calibrated at each working temperature to minimize signal drift due to temperature change. In the ramping temperature experiments, temperature was increased from room temperature to a temperature above the melting point, and friction was measured (one single scan) at the vicinity of the melting point (250ºC-280ºC). Three samples were tested for each alloy. In the constant temperature experiments, measurements were made at temperatures increasing from room temperature to 250ºC (before melting) in 50ºC increments. The normal loads and scanning speed were 10mN and 1μm/s, respectively. Five scratches were made at different locations under each temperature, and the results were averaged. The friction data obtained at room temperature was used as a reference line for comparison.

Material properties were measured through indentation tests at elevated temperatures using a Berkovich tip. The maximum load and loading/unloading rate were 10mN and 0.2mN/s, respectively. Both the sample and the tip were heated up to the desired temperatures and left overnight for thermal stabilization. Depth calibration was conducted at each temperature to rectify the output signal due to possible thermal drift. Measurements were made at temperatures increasing from room temperature to 250ºC (before melting) in 50ºC increments. Ten indents were made at each temperature at different locations and then results were averaged. Hardness was also measured after the samples were cooled down to room temperature for comparison.

2.4.3 Results and Discussion

Figure 2.8 shows the microstructures of polished Ag-Bi alloys 1-3. The silver phase (irregular in shape and dispersed in a bismuth matrix) is displayed in white in the pictures. It can

be seen that when the bismuth phase is dominant in alloy 1, the silver phase shows isolated, stripe-like shapes. As the weight percentage of silver increases, the silver phase aggregates and becomes connected, showing an island-like structure (alloy 3).

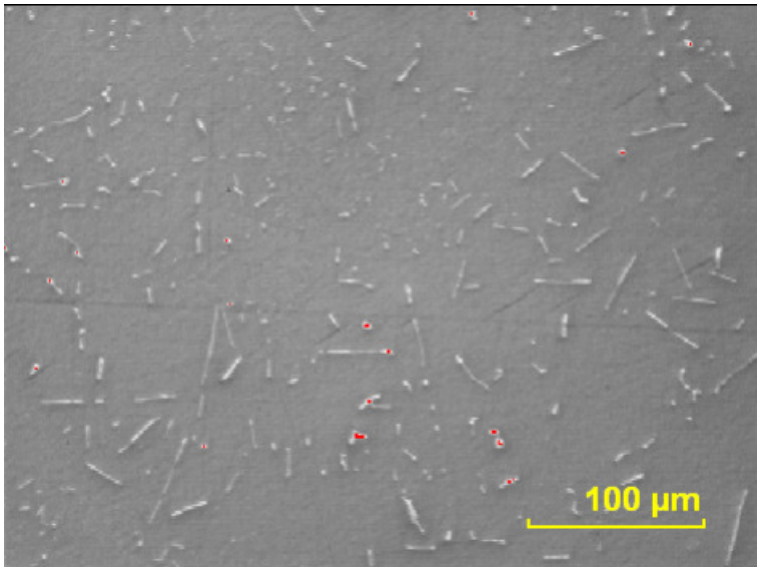

(a) Alloy 1: 97.5wt%Bi-2.5wt%Ag

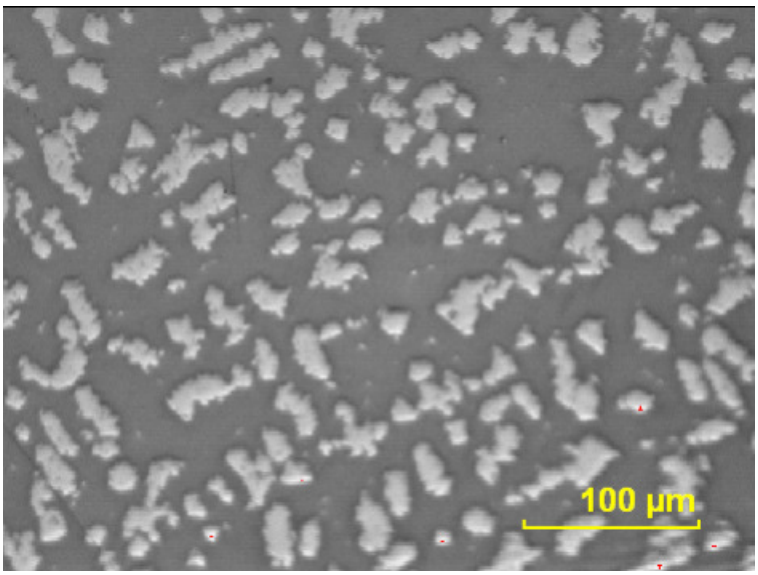

(b) Alloy 2: 70wt%Bi-30wt%Ag

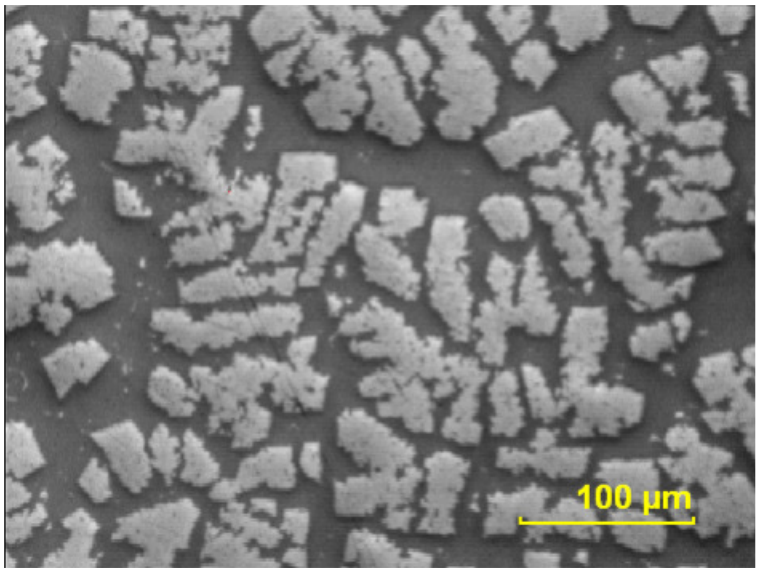

(c) Alloy 3: 50wt%Bi-50wt%Ag

Figure 2.8 Optical images of the microstructures of polished Ag-Bi alloys 1-3

Figure 2.9 (a) – (c) shows the scanning electron microscopic (SEM) images of Ag-Bi alloys 1-3 before high temperature tests and Figure 2.9 (d) shows the SEM image of alloy 3 after the test. Figure 2.9 (d) and Table 2.1 indicate that the surface of alloy 3 is roughened after melting. In our experiments, samples were polished before each test to ensure a low initial surface roughness. After melting, due to the presence of the solid phase (Ag) in the molten material, the melted bismuth (liquid) cannot move freely at the interface — its motion can be hindered by the solid, resulting in an overall increased surface roughness. The sample surface can become smoother after melting if it is originally very rough because sharp asperity disappears after melting. Similar behavior has been observed in a single element material after melting [35]. This change in roughness should be taken into account if an alloy is to be repeatedly used at elevated temperatures. For alloys 1 and 2, a large amount of liquid appears at

the interface after melting (see Ag-Bi phase diagram). Due to the vertical placement of the sample, the surfaces become uneven after the tests and thus are difficult to image using SEM.

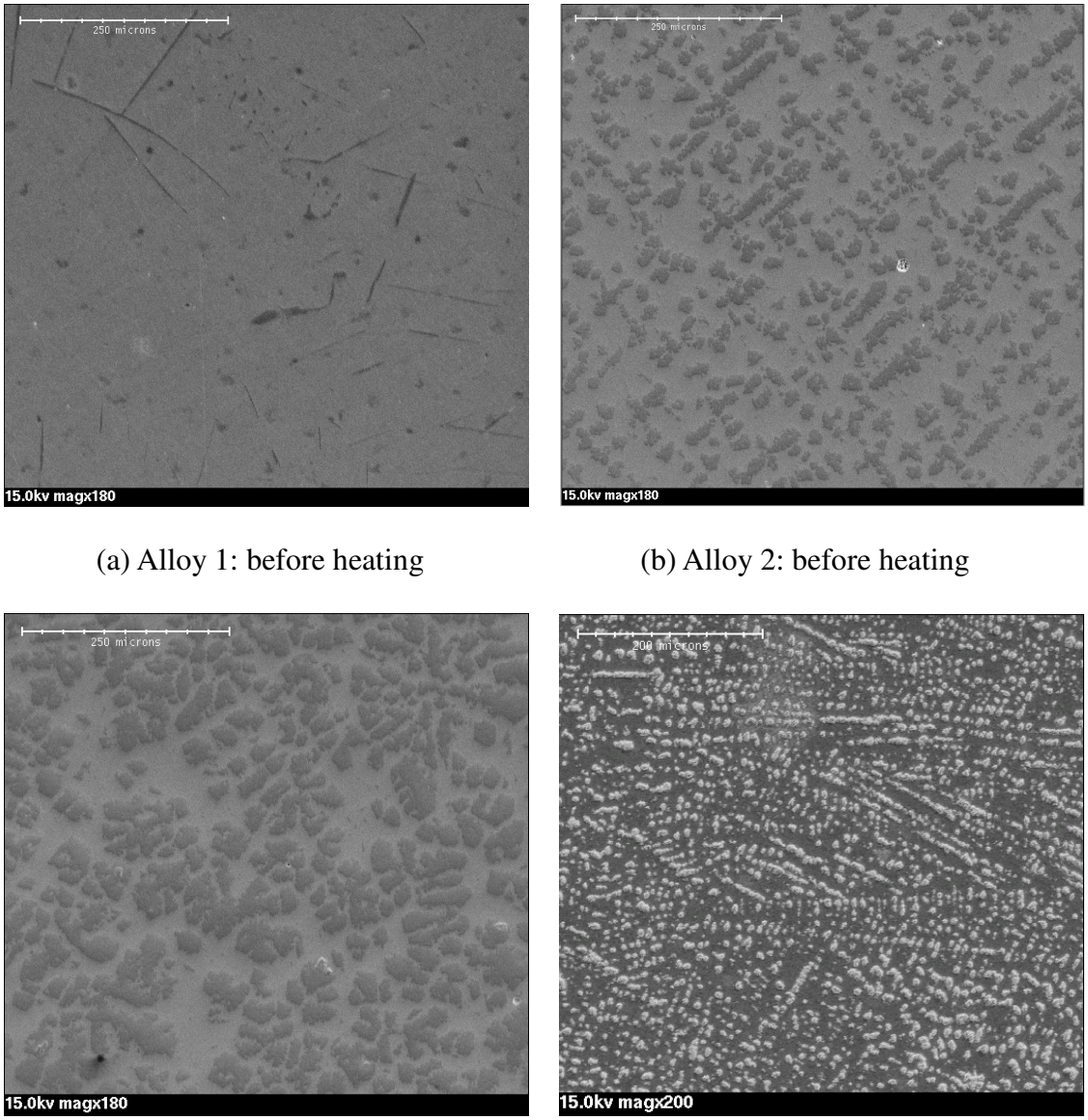

(a) Alloy 1: before heating

(b) Alloy 2: before heating

(c) Alloy 3: before heating

(d) Alloy 3: after melting

Figure 2.9 SEM images of Ag-Bi alloys 1-3 before heating and Ag-Bi alloy 3 after heating (scale bar = 250 micron)

Figure 2.10 compares the measured hardness of alloys 1-3 at elevated temperatures (before melting). As expected, it decreases with increasing temperature. It is known that the bismuth oxide – bismite (Bi_2O_3) – is much harder than bismuth [81]. Therefore, the effect of (thin) bismuth oxide on hardness at elevated temperatures can be neglected, and thermal softening is considered to be the dominant effect. This can be explained by the Hall-Petch effect. It is well known that when dislocations encounter obstacles the dislocation's motion is impeded causing the stress to continue the deformation process to increase (increasing hardness). Grain boundaries constitute such an obstacle. In most cases, the grain size of a material increases and the number of grain boundary decreases at elevated temperatures. In addition, high temperature also causes dislocations to move more actively. Therefore, it is much easier for dislocations to slip through grain boundaries at high temperature, and thus the material becomes softer [82-83]. Due to increasing silver content, alloy 3 is the hardest while alloy 1 is softer than alloy 2.

It is often observed that hardness decreases as indentation depth increases, even for tests of homogeneous materials. This is known as the indentation size effect. The following characteristic form summarizes the depth dependence of hardness (Figure 2.11) [84-85]:

$$\frac{H}{H_0} = \sqrt{1 + \frac{h^*}{h}} \tag{2.6}$$

where H is the hardness for a given depth of indentation, h, H_0 is the hardness in the limit of infinite depth, and h^* is a characteristic length that depends on the shape of the indenter, the shear modulus and H_0. It should be noted that our nanoindenter is a load-control system therefore all the indentation tests were conducted under the same load and the indentation depth may vary at different temperatures. The size effect may affect our hardness measurement results although the exact effect remains uncertain.

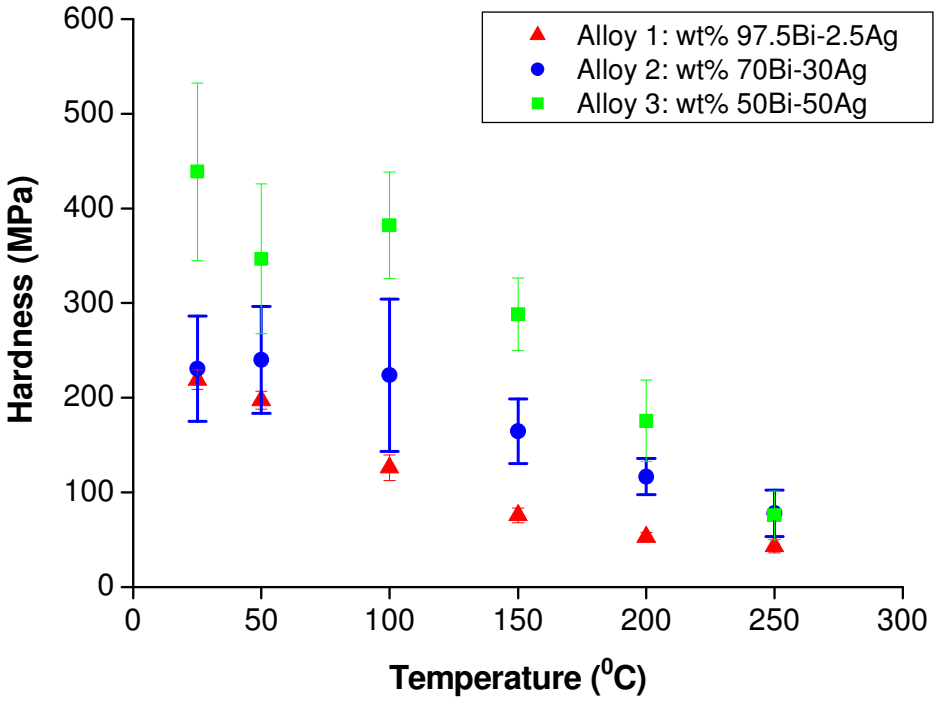

Figure 2.10 Hardness measurements of Ag-Bi alloys 1-3 as a function of temperature

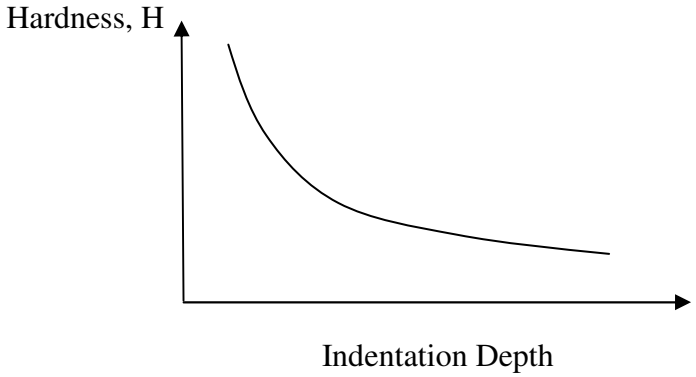

Figure 2.11 Schematic of the depth dependence of hardness

Constant-temperature friction.

Figure 2.12 shows the steady-state friction results measured at elevated temperatures. It reveals that the coefficient of friction (COF) initially remains almost constant up to about 100˚C, and then increases with temperature in the range of 100˚–250˚C. Figure 2.12 also plots the friction coefficient as a function of temperature based on the theoretical predictions. This is explained in more detail in the following.

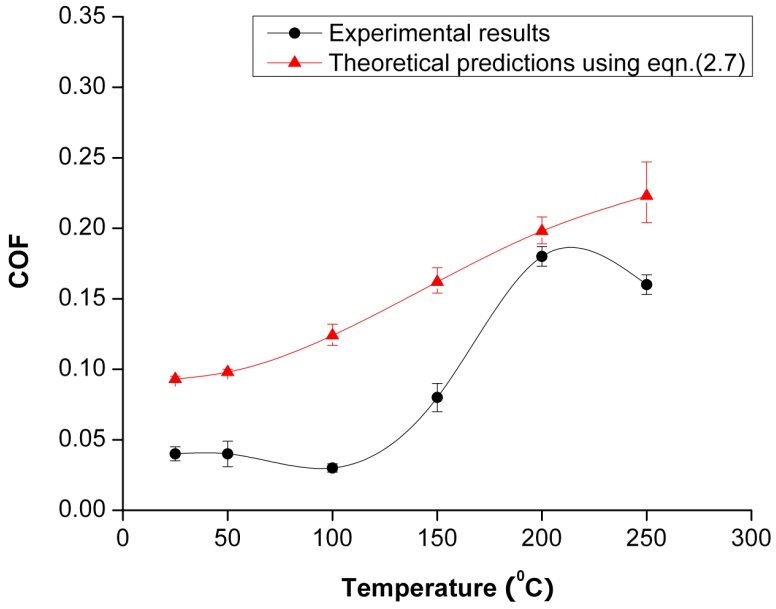

(a) Alloy1: 97.5wt%Bi-2.5wt%Ag

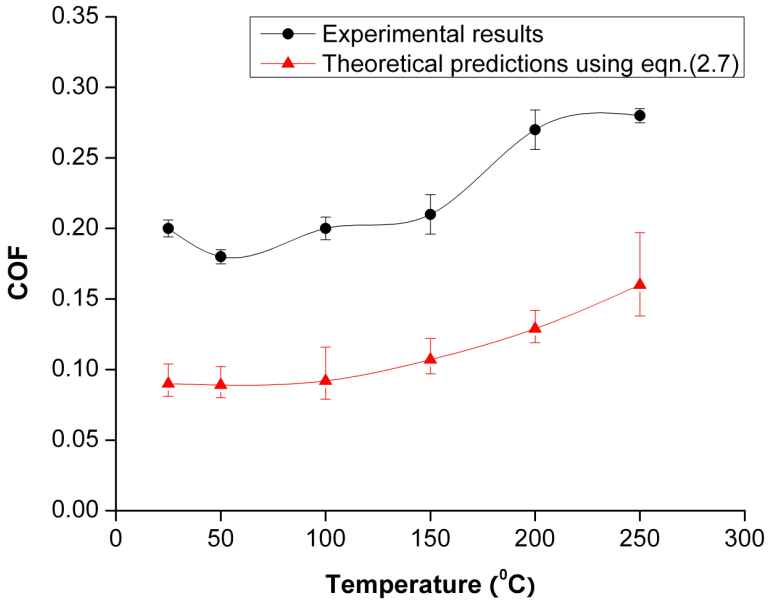

(b) Alloy2: 70wt%Bi-30wt%Ag

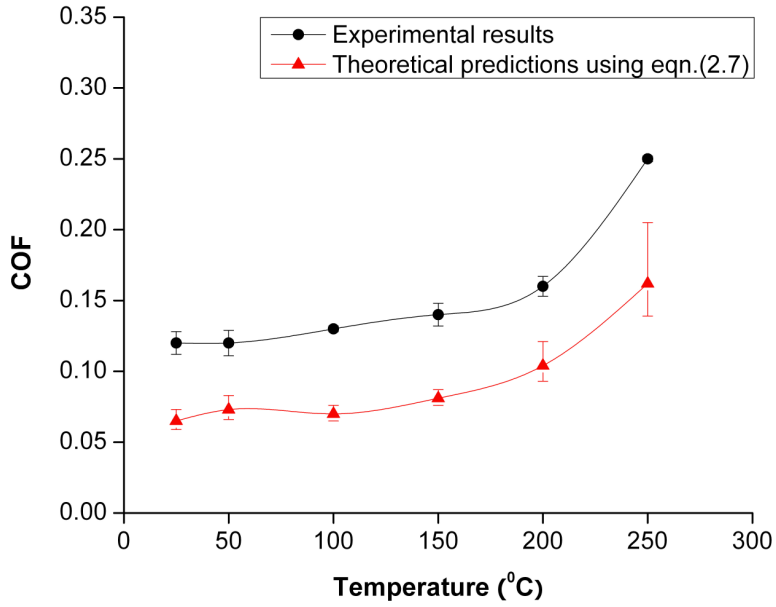

(c) Alloy3: 50wt%Bi-50wt%Ag

Figure 2.12 Constant temperature friction measurement results and theoretical predictions

Scratching friction under a constant load of this alloy group may be explained by ploughing. The Rockwell tip used in the experiments has a conical shape with a spherical extremity. Figure 2.13 shows the SEM pictures of the tip, where the diamond tip is brazed on the base material made of stainless–steel. The radius of curvature of the sphere end is about 25μm and the tip angle, 2θ, is about 90° (see Figure 2.14).

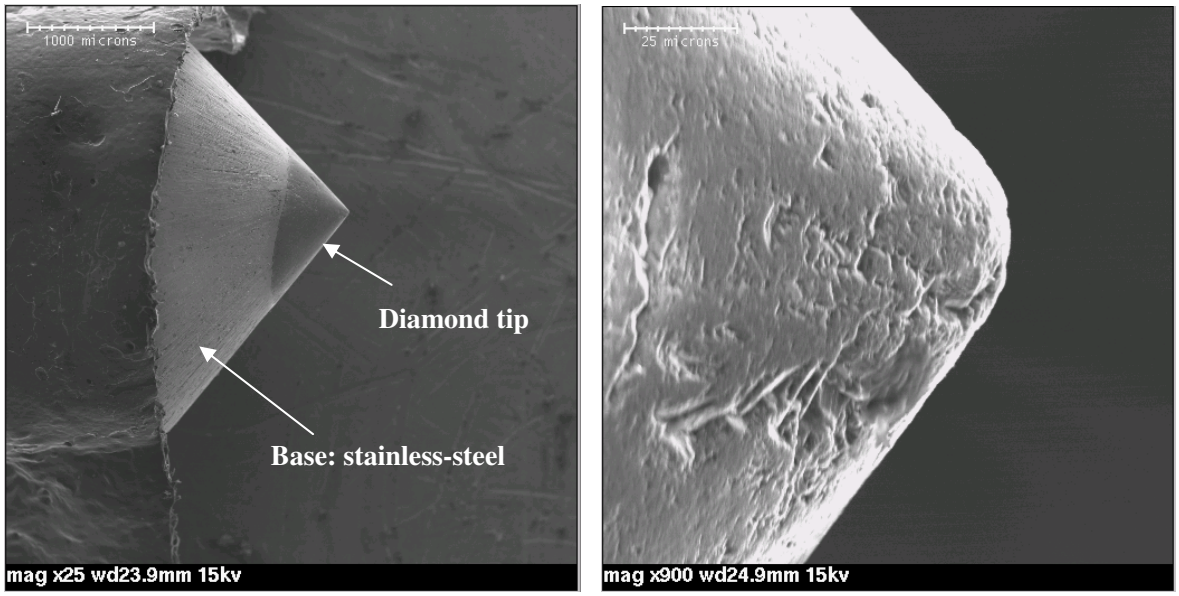

(a) Rockwell tip (b) Enlarged view

Figure 2.13 SEM pictures of the Rockwell diamond tip used in the experiments

The expression for the sliding of a perfectly spherical tip was given by Goddard *et al.* [86].

$$\mu = \frac{2}{\pi}\left(\frac{R}{a}\right)^2\left(\sin^{-1}\left(\frac{a}{R}\right) - \frac{a}{R}\sqrt{1-\left(\frac{a}{R}\right)^2}\right) \tag{2.7}$$

where a is the contact radius and R is the radius of the spherical tip (Figure 2.14). This equation assumes that the contact area is a half disc. It can be easily verified that the right hand side of the equation (2.7) is a monotonically increasing function of a. Hence, a larger contact radius will result in a higher friction coefficient.

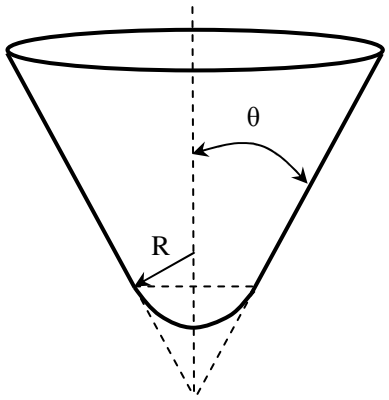

Figure 2.14 Sketch of the Rockwell tip geometry

Hardness of the material can be estimated using the applied force divided by the projected contact area (equation (2.4), $H = \frac{P}{A}$). The contact radius, a, can be estimated by

$$A = \frac{\pi a^2}{2} = \frac{P}{H} \quad \Rightarrow \quad a = \sqrt{\frac{2A}{\pi}} = \sqrt{\frac{2}{\pi}\frac{P}{H}} \tag{2.8}$$

With known hardness measured at each temperature (Figure 2.10), the contact radius can be easily obtained and thus the ploughing friction coefficient can be determined using the above equation (2.7). It is seen from Figure 2.12 that the experimental results and theoretical predictions show the same trend, that is, when temperature is less than 100ºC, the COFs remain constant; when temperature is above 100C, the COFs increase with increasing temperature.

The contact radius, *a*, becomes larger when tip penetrates deeper into the substrate. High temperature leads to a larger penetration depth because the substrate becomes softer. The heat effect on hardness may be less profound when the temperature is less than 100ºC; and therefore both the hardness and friction coefficients remain constant. When the temperature is in the range of 100ºC to 250ºC, thermal softening becomes more prominent which leads to a larger contact radius and thus a higher friction coefficient.

The deviation between theoretical predictions and experimental results may be due to defects on the tip (see Figure 2.13(b)), or tip wear after repeated use, both of which lead to uncertainty of the tip geometry. The wear debris generated during sliding can also affect friction. It is noted that the above analysis may not be applicable when the tip penetration depth is larger than the radius of the curvature of the sphere end (25μm). The maximum contact radius obtained using equation (2.8) is about 12μm which indicates the maximum penetration depth is much less than the radius of the curvature of the tip.

Figure 2.15 also compares the hardness measured at randomly selected locations in alloys 1-3 at room temperature before and after the constant high-temperature tests (without melting). Data reveals that the hardness of the heated sample after cooling is close to that of the samples before heating (in most cases). As discussed before, thermal softening is the major cause for a decrease in hardness at elevated temperatures due to larger grain size and fewer grain boundaries.

Grain size depends on the cooling rate [87]. In our experiments, the samples were left in ambient room temperature during cooling. Therefore, the grain size may not change drastically before and after heating due to the slow cooling rate. The analysis suggests that the hardness before and after high temperature tests should be similar, which in general agrees with the experiment results.

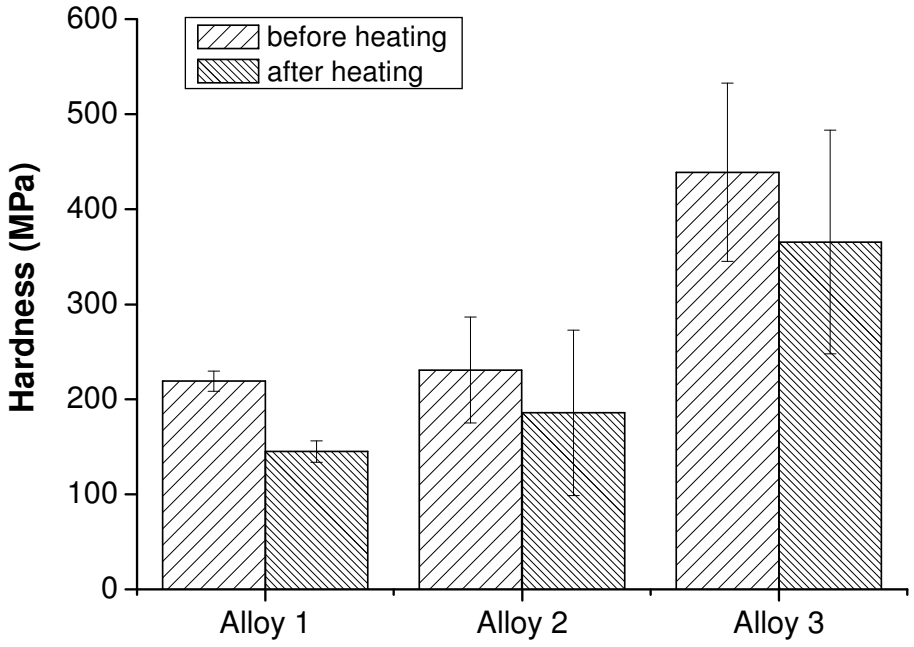

Figure 2.15 Hardness of alloys 1-3 measured at room temperature before and after heating (cooled down to the room temperature)

It is important to note that that the hardness data of alloys 2 and 3 shows much larger deviation than that of alloy 1. This is mainly due to the difference in alloy composition. Alloy 1

is almost a single-phase material. During indentation, the tip is mostly likely contacting the same phase, and therefore the measurement is more consistent and has much less deviation. On the contrary, alloys 2 and 3 are two phase alloys. The tip may randomly hit different phases in multiple indentations, which accounts for larger variation. Figure 2.16 shows the optical micrographs of the indentations made on silver and bismuth phases separately (The size of the indent is about 8μm). The indent circled in Figure 2.16 (a) was not used in the data average for indentation hardness on Bi-phase only (Figure 2.16) because the tip might have hit the silver phase. The five indents made on the silver phase (Figure 2.16(b)) were used for the data average although some indents may seem a littler bigger so that the information from Bi phase may be sampled a bit. The results from the silver and bismuth indentations shown in Figure 2.16 are plotted in Figure 2.17, where data variation ranges are much less compared to that of the general data average. Because the silver phase is harder than the bismuth phase, the higher the silver concentration is in an alloy, the harder the alloy. This also explains why a larger data variation was observed in alloys 2 and 3 than in alloy 1 in Figure 2.10. Indentation on selected phases at elevated temperatures with the assistance of a microscope is limited due to the potential damage to the microscope. Therefore, the indentation locations were randomly selected and the measured hardness shown in Figure 2.10 is a general average.

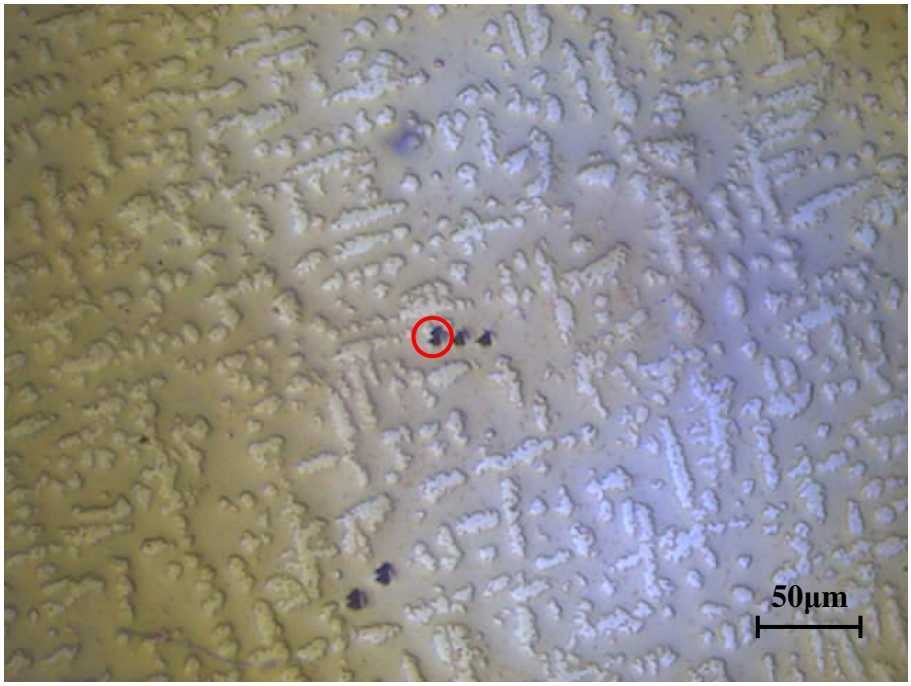

(a) On the bismuth phase only

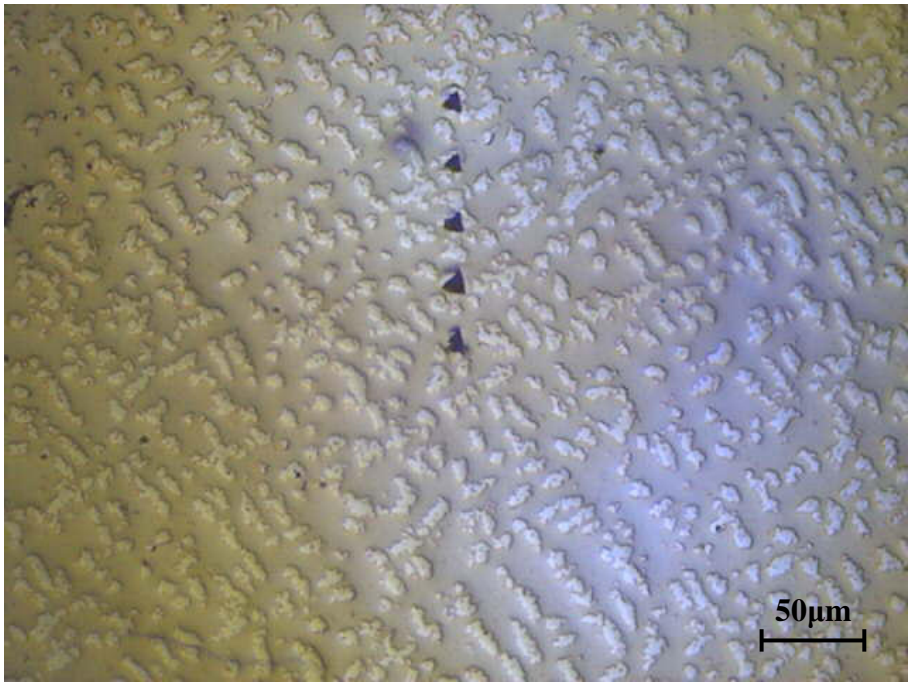

(b) On the silver phase only

Figure 2.16 Indents on different phases in alloy 1. Note that the indent circled in (a) was not used in the result analysis

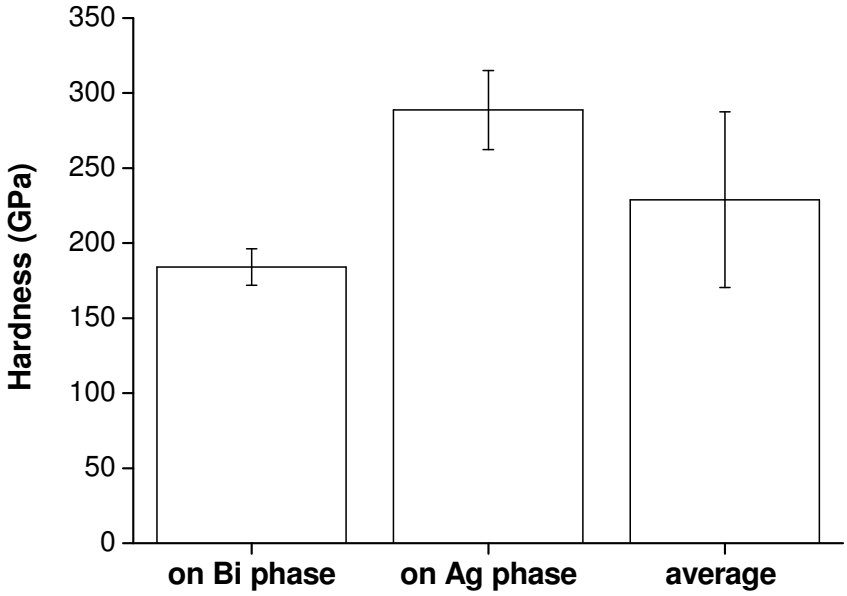

Figure 2.17 Indentation test results on different phases in alloy 1

Ramping-temperature friction

Figure 2.18 shows the ramping temperature friction measurement results. Here, temperature variation is also given corresponding to the sliding distance, and the melting temperature of each alloy is marked clearly. Friction after melting is due to the relative motion of the diamond tip and solid Ag-Bi substrate in the presence of a liquid alloy (melt) between them. A large friction drop can be observed in the case of alloy 1 and alloy 2 when the melting starts (262.5˚C according to the equilibrium phase diagram), while the COF continuously increases for alloy 3 even after the melting starts as the temperature climbs across the melting point of the material.

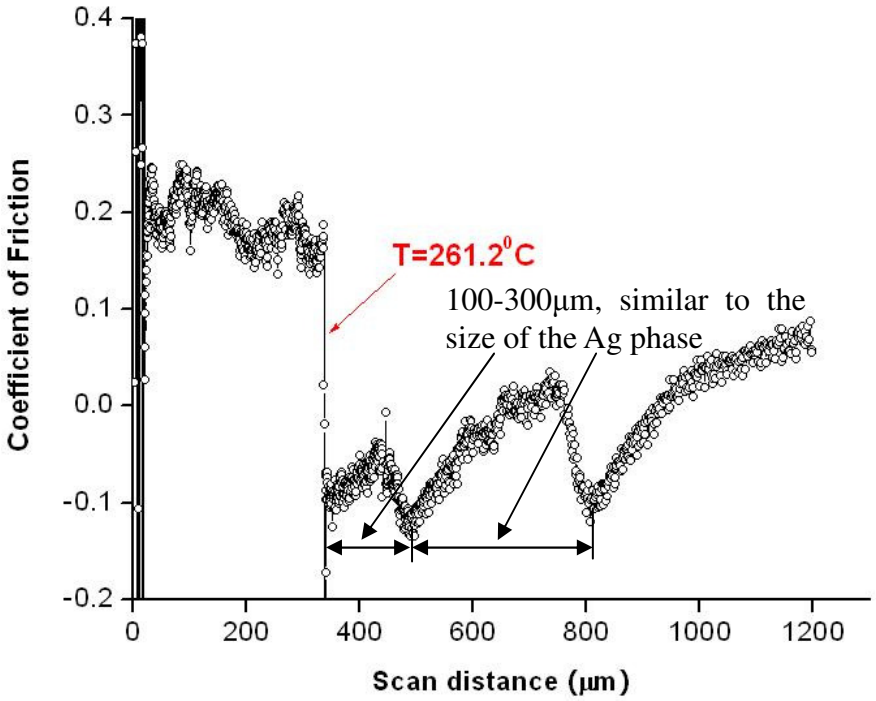

(a) Alloy1: 97.5wt%Bi-2.5wt%Ag

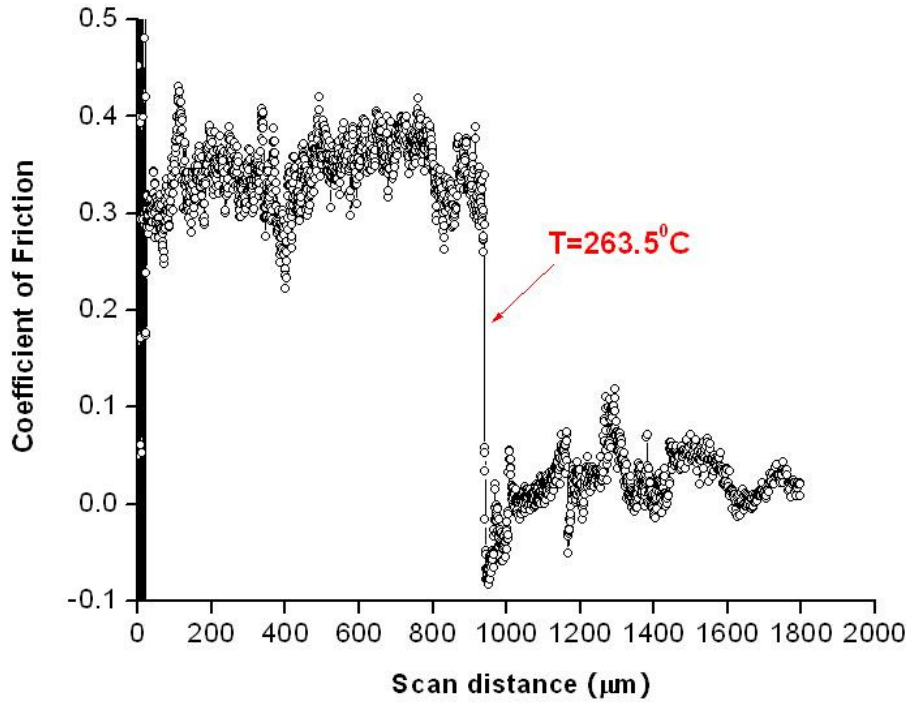

(b) Alloy2: 70wt%Bi-30wt%Ag

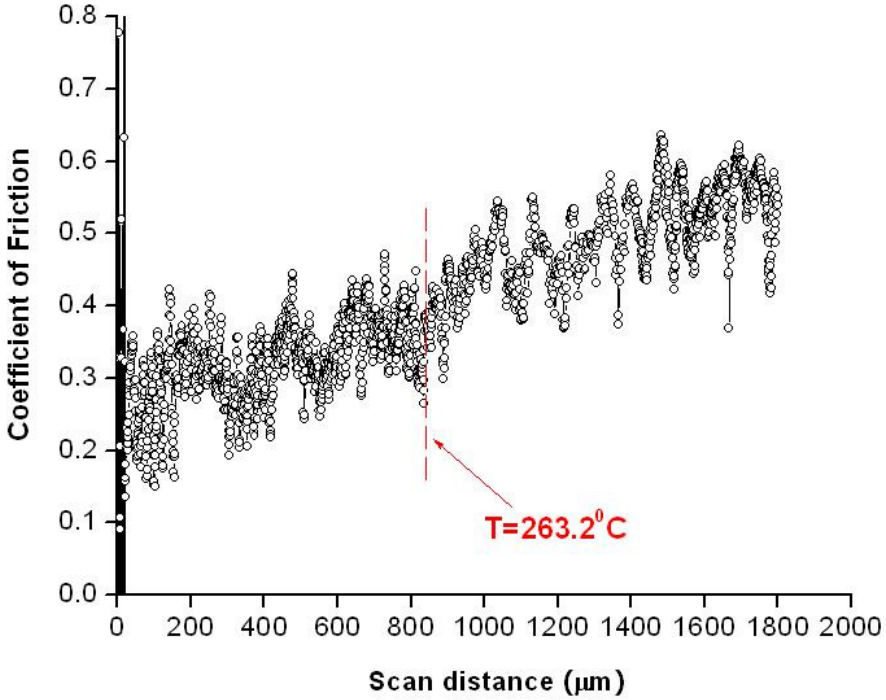

(c) Alloy3: 50wt%Bi-50wt%Ag

Figure 2.18 Ramping temperature friction measurement results

The distinct friction transition behaviors of these three alloys are due to the difference in solid/liquid compositions in the surface. Note that in this group of tests, temperature rose from 250ºC to 280ºC while scratch tests were conducted. According to the phase diagram of Bi-Ag alloys, melting in this temperature range results in a mixture of liquid and α phase. The latter is a solid solution of bismuth in silver while both remain in the solid state. The amount of the liquid metal depends on the alloy composition and the temperature. The weight percentages of the two phases can be estimated using the lever rule [87]:

$$f_\alpha = \frac{C_o - C_{Liq}}{C_\alpha - C_{Liq}} \tag{2.9}$$

where f_α is the weight fraction of the α phase in the alloy, C_o is the overall composition, C_{Liq} is the composition of the liquid phase, and C_α is the composition of the solid (α) phase.

Table 2.2 Weight fraction of three Ag-Bi alloys after melting (at 280ºC)

	Composition, weight percentage (%)	
	Liquid phase	α phase
Alloy 1	100 (approximately)	0
Alloy 2	71.8	28.2
Alloy 3	50.6	49.4

Table 2.2 lists the calculated weight fractions of the liquid and α phases of the three Ag-Bi alloys at 280ºC. For alloys 1 and alloy 2, the liquid phases are approximately 100% and 72%, respectively. The analysis shows that a lubricant layer may appear at the interface when liquid is the dominant phase in the molten material, resulting in a drastic friction drop. For alloy 3, there is about 50% solid α phase in the molten material. This larger amount of solid plays an important role and may be attributed the continuous friction increase. This will be discussed at greater length in the following.

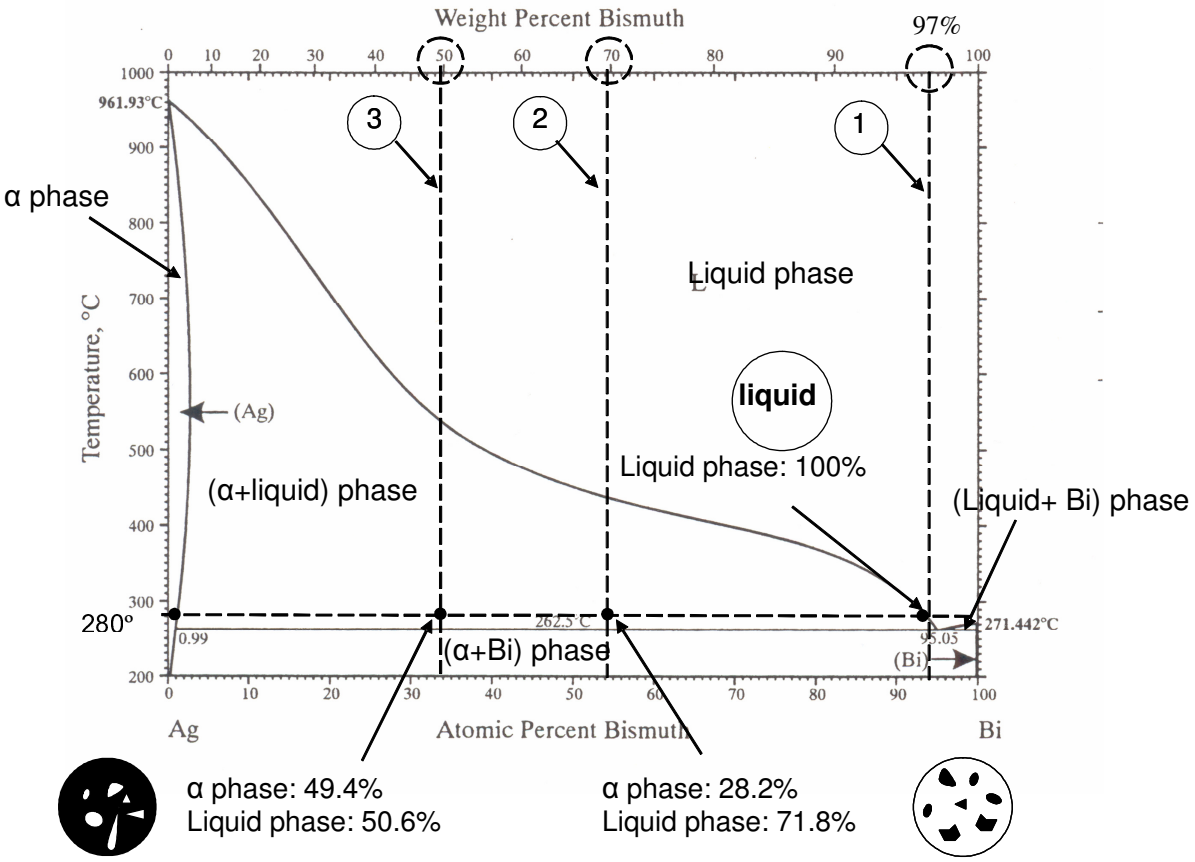

Figure 2.19 Phase diagram analysis of Ag-Bi alloys

Due to the similar densities of bismuth and silver, the weight percentage ratio is approximately equal to the volume fraction in the alloy. Therefore, distinct friction transition phenomena may also be correlated to the difference in the microstructures after melting. As is shown in Figure 2.8(a) for alloy 1, bismuth is so dominant that after melting, the entire surface should be liquid-like with small solids in isolated islands (Figure 2.19). Apparently, scratching over a liquid-like surface results in low friction. After melting, the small solids can aggregate due to liquid flow and form larger solid islands of different size. Friction varies when the tip hits the

solids in the molten material. It increases when the tip climbs up and decreases when the tip slides down [35-36; 88]. This correlation may explain the friction variation patterns (spacing ranges from 100 to 300μm) in the friction diagram of alloy 1 after melting. The same conclusion is true for alloy 2, except that the pattern in the friction diagram after melting is not as clear.

The optical image of alloy 3 (Figure 2.8(c)) reveals that the liquid (bismuth) phase is much less than the solid α phase after melting, and that the entire surface remains solid-like but with small liquid reservoirs in between (Figure 2.19). When the tip travels on the surface, no friction drop is observed. Instead, as temperature increases, the surface becomes softer and the tip may penetrate deeper into the substrate and deform more material, which leads to a continuous increase in friction. The solid-like sample surface is directly observed after the ramping temperature friction tests. The smoothness of surfaces of alloys 1 and 2 is altered by the flow of a large amount of liquid due to vertical mounting, while the surface of alloy 3 remains nearly intact although it looks blurred (not mirror-like) due to the increased surface roughness (see Table 2.1).

Figure 2.20 depicts an example of the depth profile of a ramping temperature friction measurement of alloy 3. It is noted that the depth varied after melting in the scratching process, which means that the tip might be in contact with a solid-like surface. The depth variation interval (50-200μm) closely matches the size of the bismuth phase (Figure 2.8 (c)), or liquid reservoirs produced by melting. The depth variation is likely due to the fact that the tip traveled in and out of the liquid reservoirs in the surfaces. No correlation between the depth variations and the friction change can be found, yet Zou *et al.* reported that friction changes correspond to the slope of the surface geometry [36, 88]. The depth variation behavior was not observed in alloys 1 and 2 because the surface becomes liquid-like after melting and thus the depth remains

at a minimum level.

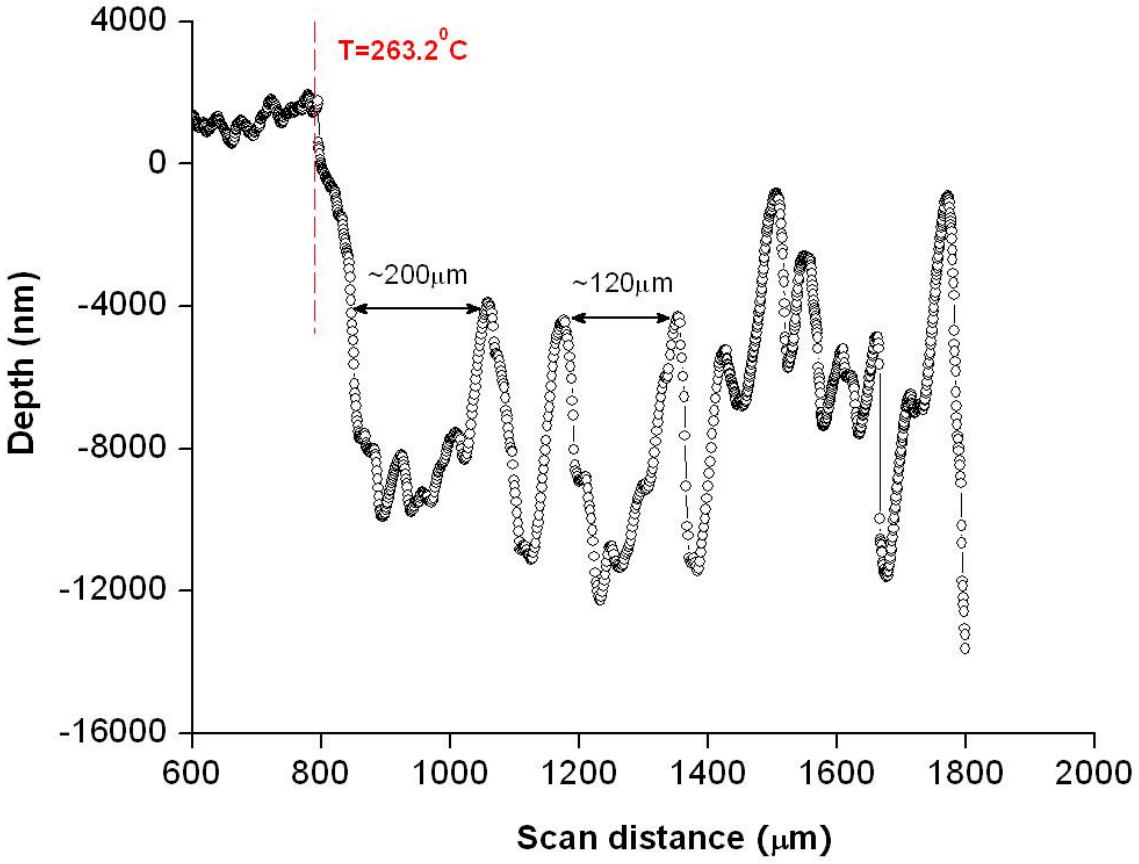

Figure 2.20 An example of the depth profile of a ramping temperature friction measurement in alloy 3

Data analyses mentioned above suggest a critical bismuth composition (between alloy 2 and 3) in the Ag-Bi alloy system, below which the molten material may hardly reduce the nano/microscale friction after melting. Two more alloys, 60%Bi-40%Ag and 65%Bi-35%Ag, were made and prepared using the same procedures described in the previous section. Figure 2.21 shows the ramping temperature friction measurement results of these two alloys. In both

cases, no friction drop is observed. Therefore, one may conclude that the critical bismuth composition for the Ag-Bi alloy system lies between 65% and 70%. As summarized in Figure 2.22, when bismuth concentration is above the critical value, the molten material is a dominant factor of friction reduction. If the bismuth concentration is less than the critical value, the solid phase contributes more to friction; and an increase in friction due to increased tip penetration depth may be observed.

2.5 Summary

The effect of melting on silver-bismuth alloy nano/microscale friction has been studied by means of high temperature nanoindentation and scratching. Ramping temperature tests for transient friction behaviors and constant temperature tests for friction-temperature correlation have been conducted. High-temperature nanoindentation hardness of these alloys has also been measured. The constant temperature results under the same load indicate that friction slightly increases as temperature approaches the melting point. The transient results reveal different friction transition phenomena for the alloys with different bismuth concentration when temperature climbs across the melting point. The molten material does not always reduce the nano/microscale friction of the silver-bismuth alloys, and the friction characteristic depends on the alloy composition. The existence of a critical bismuth concentration is identified, above which the molten material can help reduce the nano/microscale friction at the scratching interface formed with the silver-bismuth alloy.

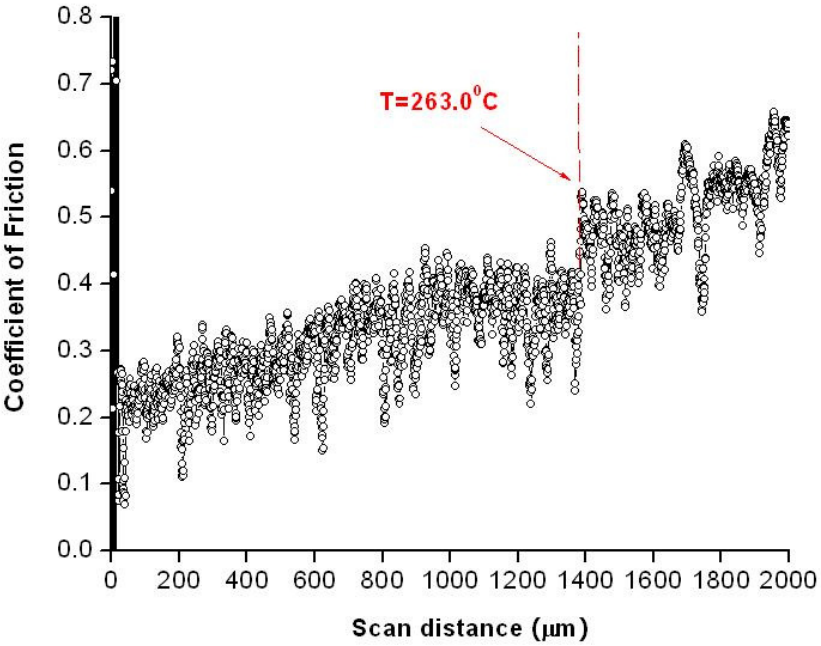

(a) 60%Bi-40%Ag

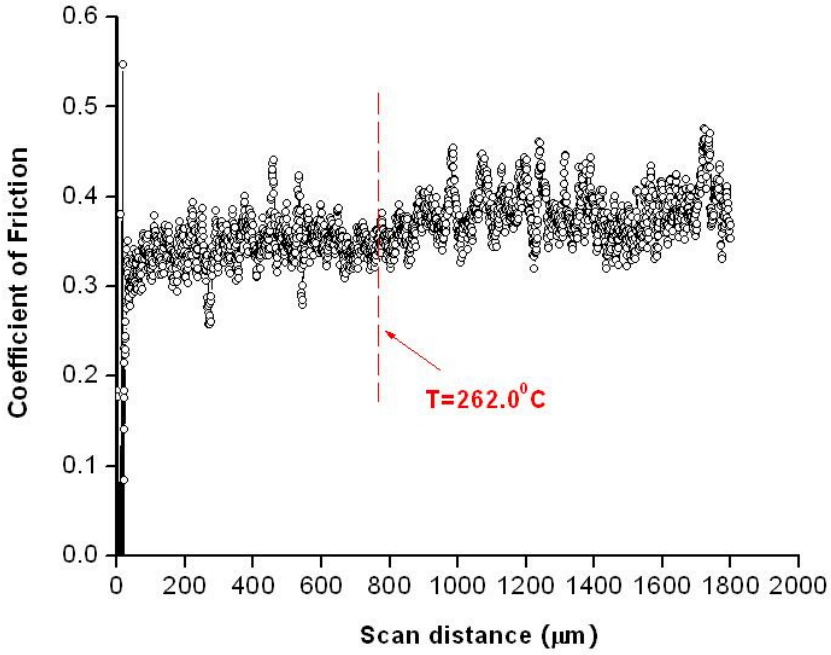

(b) 65%Bi-35%Ag

Figure 2.21 Ramping temperature friction measurement results for two additional alloys

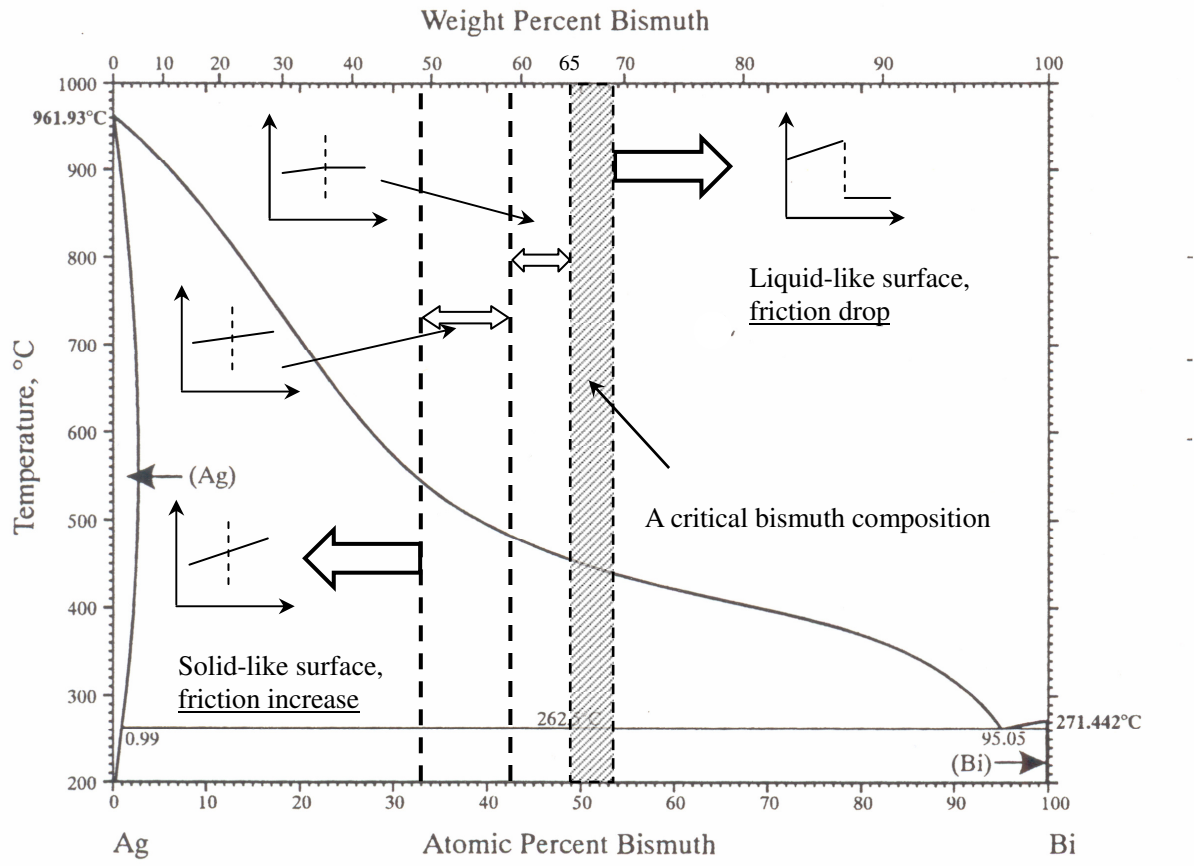

Figure 2.22 A cartoon of the friction transition behavior of the Ag-Bi alloy system at the vicinity of the melting point as a function of the bismuth composition

CHAPTER THREE: SURFACE TEXTURE EFFECT ON FRICTION OF A MICROTEXTURED POLY(DIMETHYLSILOXANE) (PDMS)

3.1 Introduction

Various techniques have been developed to produce surface texture effectively and efficiently, including milling, blasting, and energy beam processing [89-90]. Among them, the laser beam processing seems to be more effective owing to its capability to generate textures with complicated and precise geometry at a fast speed, especially in patterning metallic surfaces. However, the cost of laser manufacturing equipment is high [24]. Microfabrication techniques, originated from the microelectronics industry, can be utilized to create high-density surface textures of complicated geometry in relatively simple and cheap processes. Micromolding is one of the commonly used techniques in microfabrication. An elastomer such as poly(dimethylsiloxane) (PDMS) is usually used to cast against a patterned substrate created by a lithographic technique. The patterns on the substrate are then transferred to the PDMS surface. This technique can generate features as small as 250 nm [91]. The advantages of low cost and convenient processing, as well as biological and chemical compatibility, enable this technology to be widely adopted in microfluidic, chemical, and biological applications [92-93].

In this work, different textures are created on PDMS surfaces using the micromolding technique. Friction tests are conducted with a nanoindentation-scratching system at the macro- and microscale, respectively. The effects of surface texture and normal load on friction are investigated.

3.2 Experimental Considerations

3.2.1 Sample Fabrication and Surface Characterization

Textured surfaces with square pillars and grooves of different dimensions were fabricated by the micromolding technique [91-94]. The fabrication process is illustrated in Figure 3.1. A mask was used in the contact photolithography to create a mold with a negative-tone UV photoresist (MicroChem Corporation, SU-8 25, Newton, MA, USA) on a silicon wafer. A curing agent and the PDMS prepolymer (Sylgard 184 Silicone Elastomer Kit, Dow Corning, Midland, MI, USA) were thoroughly mixed in a 1:10 weight ratio. The prepolymer mixture was degassed in ambient for about 3 hours to remove any air bubbles in the mixture and ensure complete mixing of the two parts. The prepolymer mixture was poured into the mold and cured on a hot plate at 90°C for 1 hour. After curing, the PDMS replica was peeled from the mold and cut into small pieces for testing. For imaging purpose, additional samples were sputter-coated with a thin layer of gold (1.5nm) and imaged by scanning electron microscopy (SEM) (Hitachi S-4500). The SEM micrographs are shown in Figure 3.2. Wrinkles can be found on the surfaces, which may be due to the mismatch of the thermal expansion coefficients of the gold film and the PDMS substrate. The geometries of the textured surfaces were measured using a phase-shift white-light interferometer, and the data is listed in Table 3.1. The height of the textures was about 2.5μm (Figure 3.2(f)).

3.2.2 Test Apparatus and Methods

Friction measurements were conducted with a nanoindentation-scratching system (NanoTest 600, Micro Materials Ltd, UK), which was explained in detail in Chapter 2. In this work, all tests were conducted at room temperature. Friction testes at the macro- and microscale were conducted using a stainless-steel bearing ball (304 stainless steel, diameter D=1.6mm) and a Rockwell diamond tip (tip radius R=25μm), respectively. The normal loads were 5, 10, and 25mN, and the scanning speed was 1μm/s. Coefficient of friction (COF) is defined as the ratio of the lateral force over the normal load. Three measurements (scratches) were taken at different locations under each operating condition and the results were averaged.

(a) Spin coat photoresist SU8-25

(b) Photolithography to create the mold

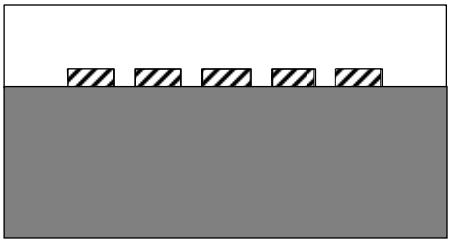

(c) Pour PDMS on the mold

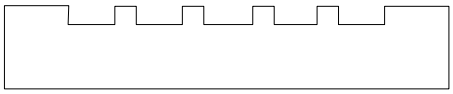

(d) Peel the PDMS polymer from the SU8 mold

Figure 3.1 Schematic of the fabrication process of the textured PDMS surfaces

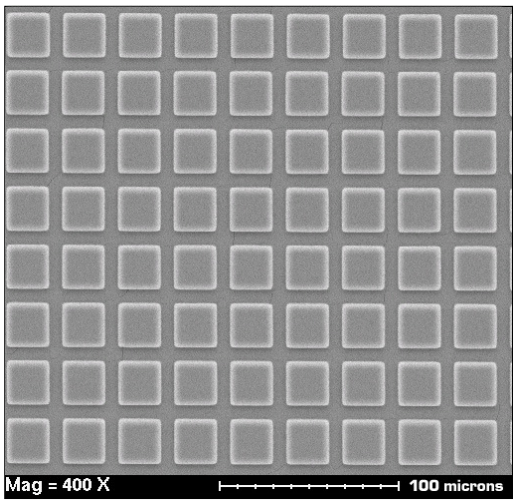

(a) P1

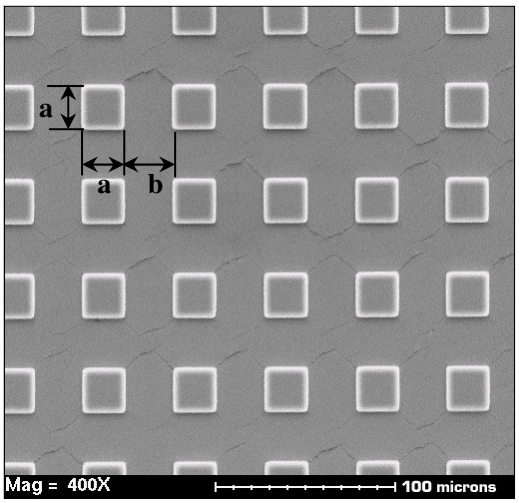

(b) P2

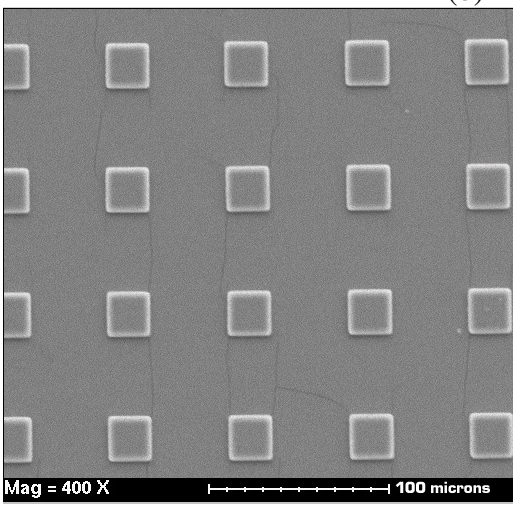

(c) P3

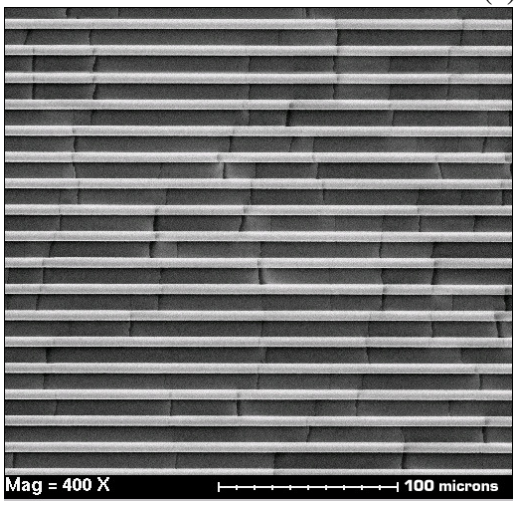

(d) G1

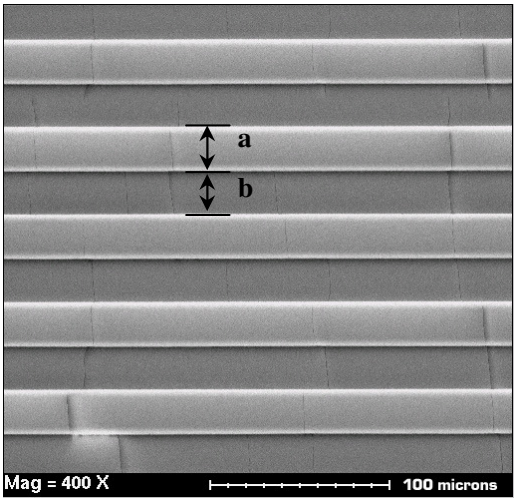

(e) G2

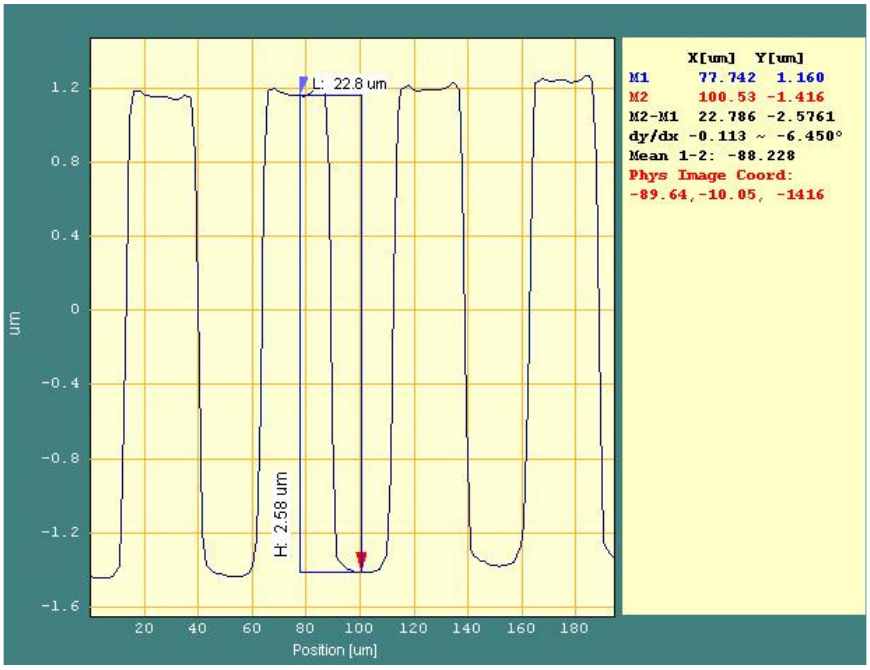

(f) Depth profile of the G2 surface (measured using a phase-shift white light interferometer)

Figure 3.2 SEM and optical images of the textured PDMS surfaces

Table 3.1 Geometry of the textured PDMS substrates

Pattern index	Size a (μm)	Spacing b (μm)	Note
P1	24.1	9.2	Pillar
P2	24.1	28.7	
P3	24.1	46.0	
G1	5.38	9.42	Groove
G2	24.1	25.5	

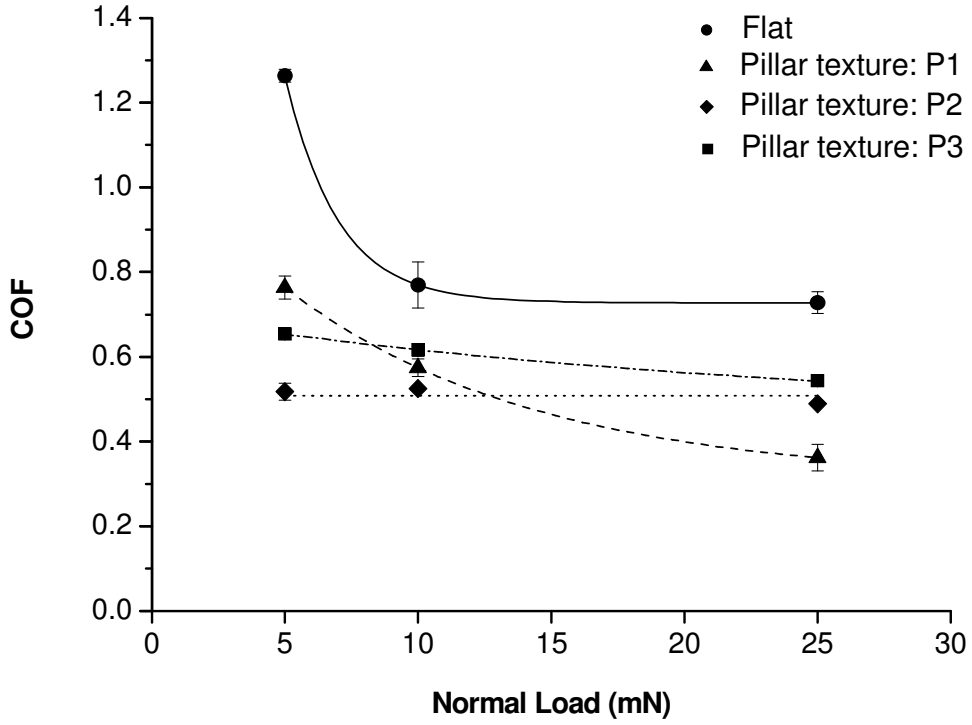

Figure 3.3 COFs for the flat and three pillar-textured surfaces (P1-P3) obtained from the macroscale tests using a bearing ball (304 stainless steel) with a scanning speed of 1μm/s

3.3 Friction Characterization of Pillar-textured Surfaces

3.3.1 Macroscale Friction

Figure 3.3 shows the relationship between the averaged COF of three measurements and the normal load for the flat and three pillar-textured surfaces (hereafter referred to as P1-P3 surfaces), measured by mating a stainless-steel bearing ball. The results suggest that surface textures have a significant effect on reducing friction under all three loading conditions. For

example, the COF for the P2 textured surface measured under the load of 5mN is only 41% of that for the flat surface, and the COF for the P1 textured surface measured under the load of 25mN is only 50% of that for the flat surface.

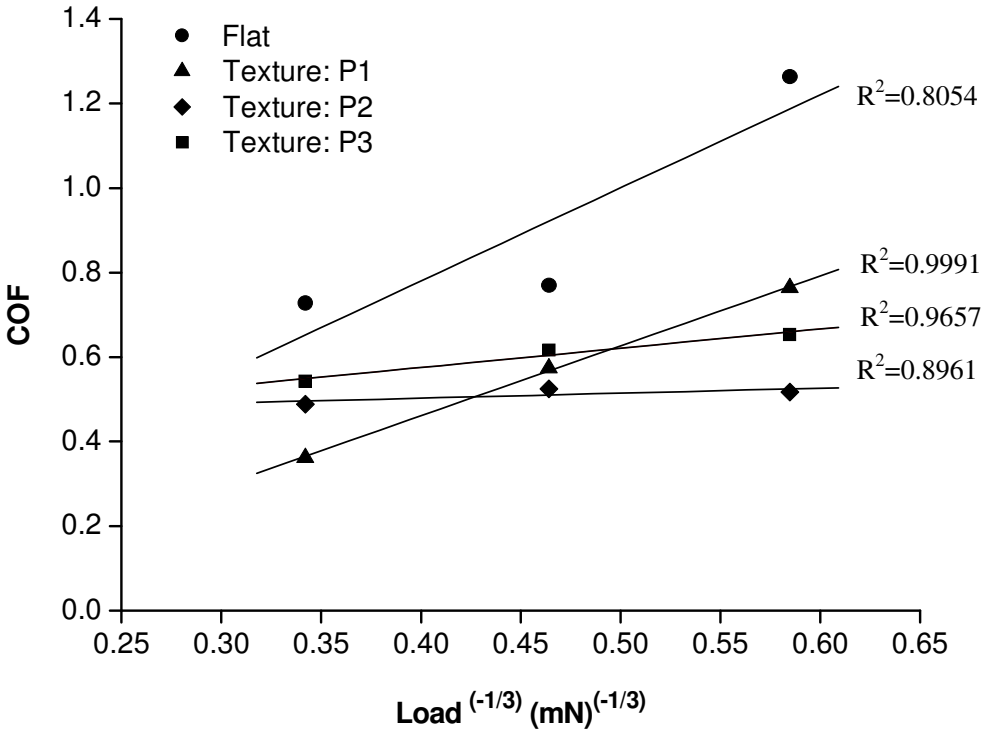

Figure 3.4 COF versus load$^{(-1/3)}$ obtained from the macroscale tests

In order to understand the effect of surface textures on COF, the relationship between COF and load$^{(-1/3)}$ is plotted in Figure 3.4, in which a linear relationship between COF and load$^{(-}$

$^{1/3)}$ can be observed for all three textured surfaces. However, for the flat surface, the deviation is larger, and COFs seem to have a weaker correlation with load$^{(-1/3)}$. It is known from the classic friction theory that the friction force at dry contact is proportional to the product of the real contact area and the shear strength of the weaker material [35]. Since the real contact area is proportional to load$^{(2/3)}$ for elastic contact, COF should be proportional to load$^{(-1/3)}$. The larger deviation of the data for the flat surface may be due to the presence of a stronger surface adhesion force which affects the real area of contact. When the surface adhesion force is considered, either the Johnson–Kendall–Roberts (JKR) or Derjaguin–Muller–Toporov (DMT) theory may be used to analyze the friction behavior. The JKR theory is usually used for large radius compliant solids, while the DMT theory is applicable for small rigid solids [95-97]. Typically, a crosslinked PDMS system meets the requirements for the JKR theory [98]. According to the JKR theory, the contact radius is

$$a = \left[\frac{R}{K} \left(P_0 + 3w_a \pi R + \sqrt{6w_a \pi R P_0 + (3w_a \pi R)^2} \right) \right]^{\frac{1}{3}} \tag{3.1}$$

where R is the equivalent radius of curvature, $\frac{1}{R} = \frac{1}{R_1} + \frac{1}{R_2}$, K is the equivalent elastic modulus of the two surfaces, $\frac{1}{K} = \frac{4}{3}\left(\frac{1-\upsilon_1^2}{E_1} + \frac{1-\upsilon_2^2}{E_2} \right)$, P_0 is the external force applied, and w_a is the work of adhesion or energy per unit contact area. The second and third terms in equation (3.1) are due to the surface adhesion force. When $w_a = 0$, equation (3.1) becomes the classic Hertz equation, $a^3 = RP_0 / K$. As a result of the surface adhesion force, the contact size is larger than the value from the Hertz model. The work of adhesion, w_a, needs to be determined for different

solid-solid contact. It is noted that there is no apparent difference in the value of work of adhesion between PDMS-PDMS, PDMS-Si, and PDMS-F system [98]. Here the value for PDMS-PDMS contacts (~40mJ/m^2) was used to estimate the ratio of the contact area due to elastic deformation and adhesion force. As a low elastic modulus material, PDMS's Young's modulus and Poisson ratio depend on the mixing ratio of the curing agent and the PDMS prepolymer [99-100]. The material used in this work was made with a mixing ratio of 1:10 (curing agent versus prepolymer) and its Young's modulus and Poisson ratio are approximately 750 KPa and 0.48, respectively. Table 3.2 lists the computation results of the contact radius of a ball-on-flat contact due to adhesion and elastic deformation, and their ratio as well. Due to the presence of the surface adhesion force, the overall contact radius can be increased by 41% of that due to elastic deformation only. Summarizing, the reason of the deviation from the COF–load$^{(-1/3)}$ relationship for the flat surface is likely due to the surface adhesive force, while the good agreement for the textured surfaces can be attributed to the fact that the surface adhesion force is greatly reduced owing to the presence of the textured voids.

Table 3.2 Comparison of the contact radius of a ball-on-flat contact due to elasticity and adhesion at the macro- and microscales ($w_a = 40\,\mathrm{mJ/m^2}$; at macroscale, R=0.6mm; at microscale, R=25μm)

		With respect to the applied load		
		$P_0=5\times10^{-3}$ mN	$P_0=10\times10^{-3}$ mN	$P_0=25\times10^{-3}$ mN
Macroscale	First (elastic) term in the JKR equation: $(P_0)\times(R/K)$	5×10^{-3} (R/K)	10×10^{-3} (R/K)	25×10^{-3} (R/K)
	Second and third (adhesive) terms in the JKR equation: $(3w_a\pi R+\sqrt{6w_a\pi RP_0+(3w_a\pi R)^2})\times(R/K)$	2.06×10^{-3} (R/K)	2.78×10^{-3} (R/K)	4.20×10^{-3} (R/K)
	Percentage of the adhesive to the elastic term	41%	28%	17%
Microscale	First (elastic) term in the JKR equation: $(P_0)\times(R/K)$	5×10^{-3} (R/K)	10×10^{-3} (R/K)	25×10^{-3} (R/K)
	Second and third (adhesive) terms in the JKR equation: $(3w_a\pi R+\sqrt{6w_a\pi RP_0+(3w_a\pi R)^2})\times(R/K)$	3.17×10^{-4} (R/K)	4.44×10^{-4} (R/K)	6.96×10^{-4} (R/K)
	Percentage of the adhesive to the elastic term	6%	4%	3%

The three textured substrates are designed in such a way that they have approximately the same pattern size but different spacing in order to address the geometry effect of surface textures. A three-dimensional thermomechanical model developed by Liu and Wang [21], which considers the existence of surface roughness (texture) and friction-induced deformation, was used to determine the real contact area. Table 3.3 lists the numerical results of the contact area for the flat and three pillar-textured surfaces under 5, 10, and 25mN at the macroscale. Among the three textured geometries, the P3 surface has the largest contact areas, while P1 surface has the smallest ones under all three loading conditions, which suggests that the maximum and minimum COF occurs on the P3 and P1 surfaces, respectively. The experiment results (Figure 3.3) show that this is only true for the case under 25mN normal load, while at lower normal loads the COF

on the P1 surface is not always the smallest, for example under 5mN the COF on the P1 surface is the largest among the three textured surfaces. The difference between the experimental and simulation results of the friction behavior on the P1 surface is likely due to the effect of the adhesion force, which has more contributions to the overall contact area at lower loads especially on the surface with higher texture density, while the effect is minimal at higher loads (see Table 3.2).

Table 3.3 Numerical results of the contact area for the flat and pillar-textured surfaces under different normal loads at the macroscale

Contact area (mm^2)	**Normal load (mN)**		
	5	**10**	**25**
Flat surface	6.7066×10^{-2}	1.0659×10^{-1}	1.9575×10^{-1}
P1 (spacing=9.2μm)	3.6024×10^{-2}	5.7041×10^{-2}	1.1155×10^{-1}
P2 (spacing=28.7μm)	4.5335×10^{-2}	7.9294×10^{-2}	1.5995×10^{-1}
P3 (spacing=46.0μm)	5.4992×10^{-2}	8.9456×10^{-2}	1.7476×10^{-1}

Figure 3.3 also reveals that COF reduces with increasing load (except for the case of P2), which may be explained by either the classic theory (COF is proportional to load$^{(-1/3)}$) or the surface effect. The latter has been explained in details using an orientation/alignment mechanism [101-104]. It is known that the crosslinking reaction is usually incomplete, leading to an imperfect PDMS network. Some free chains are not chemically bonded to the network and can

be aligned along the friction direction which permits easy sliding of the mating surface under a shear loading. These long chains at the interface experience higher shear stress at high normal loads, which favors the orientation and leads to a lower COF. When the normal load is low, the PDMS interfacial layer is less compressed, and the resulting lower shear stress may limit the orientation effect. Free chains favor adhesion to the mating ball, resulting in a higher COF. However, it is not conclusive whether the bulk effect (deformation) or the surface effect is dominant.

3.3.2 Microscale Friction

Figure 3.5 shows the friction results for the flat and three different pillar-textured PDMS surfaces under 5, 10, and 25 mN normal loads using a Rockwell diamond tip. Although the textured surfaces offer lower COFs under 5 and 10mN loads, COFs between the flat and textured surfaces are approximately the same under 25mN. The COF on the P1 textured surface measured at the load of 5mN is about 62% of that on the flat surface.

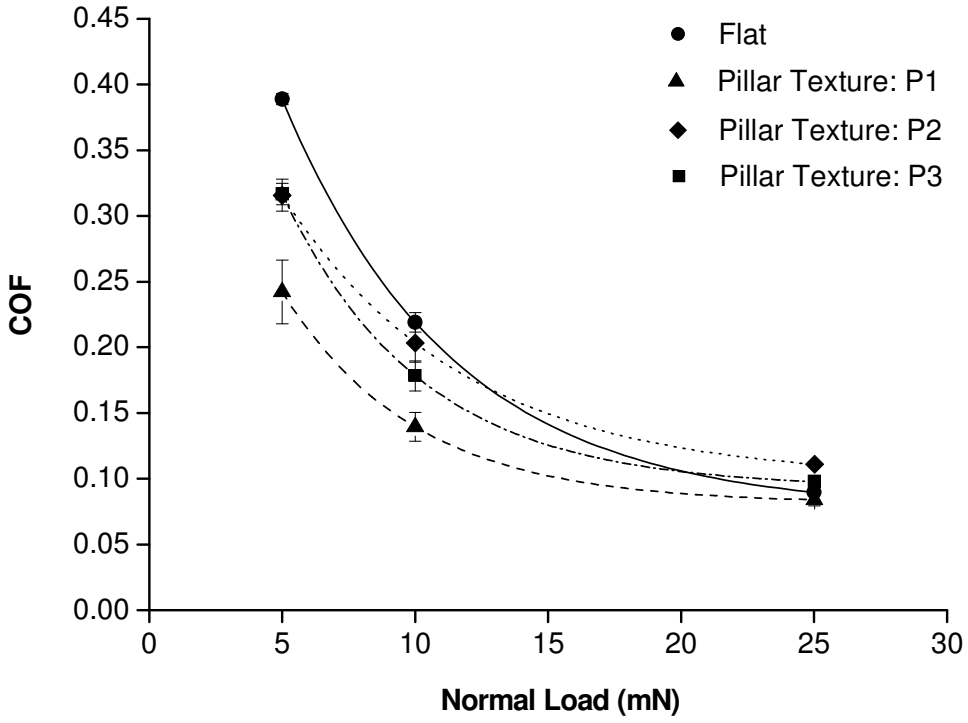

Figure 3.5 COFs for the flat and pillar-textured surfaces obtained from the microscale tests using a Rockwell diamond tip with a scanning speed of 1μm/s

The surface texture effect on friction is less profound at the microscale as compared to the macroscale test results. As discussed before, surface textures can greatly reduce the real contact area at the macroscale, which in turn reduce the friction. While at the microscale, the tip size is comparable to the texture geometry, and it may just follow the shape of the surface textures during sliding. In addition, the contact pressure is much higher at the microscale as compared to that at the macroscale under the same load, which not only facilitates the

displacement of the tip in the vertical direction, but also makes surface adhesion less important (Table 3.2). Surface textures are, therefore, unable to effectively reduce contact area and thus have less effect on friction at the microscale. This argument is especially true for the case under a high normal load (i.e., under 25mN).

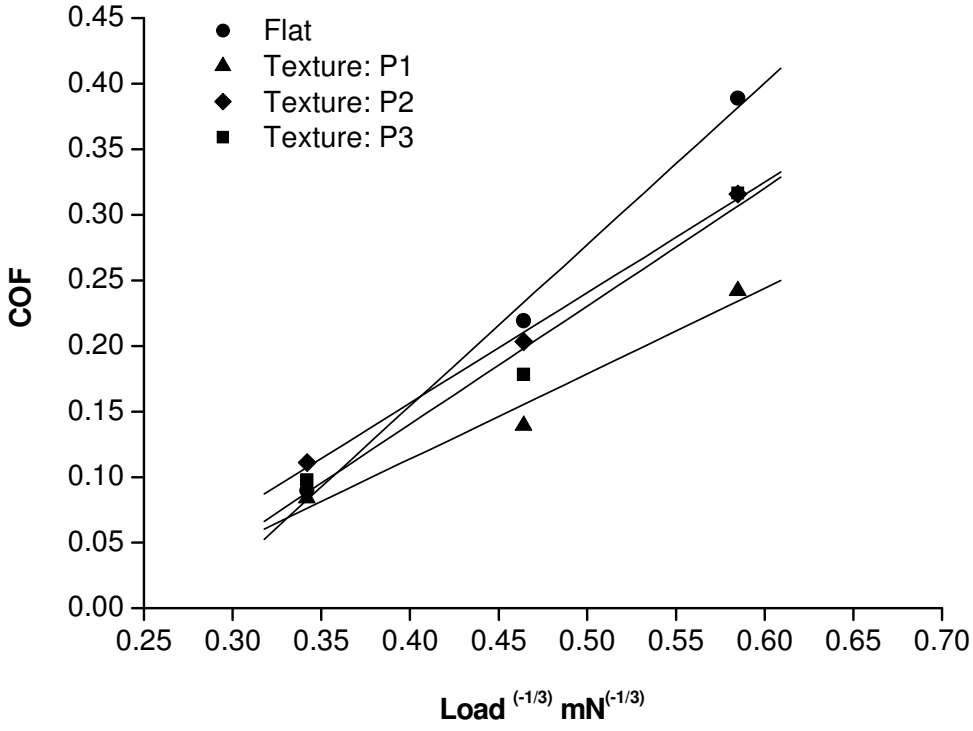

Figure 3.6 COF versus load$^{(-1/3)}$ obtained from the microscale tests

Figure 3.6 shows good linear relationship between COF and load $^{(-1/3)}$ for both the flat and textured surfaces, which suggests that the adhesion effect on friction is less important at the microscale due to the increased contact pressure. The load effect on COF is more uniform at the microscale. The lines in Figure 3.6 all show higher COF at lower normal loads. The contact area at the microscale is not calculated because the contact condition changes during sliding when the Rockwell tip slides down or climbs up pillars. However, it is observed that at the microscale, the COF for the P1 surface is always the lowest under all three normal loads.

It has been noticed that the COF at the macroscale is always higher than that at the microscale. This is likely due to the fact that the real area of contact is much larger at the macroscale comparing to the one at the microscale, as illustrated in Figure 3.7 (a) and (b). At the macroscale, there are multiple pillar structures in contact with the mating ball in the contact area, while at the microscale the diamond tip may only slides against a unit pillar due to their comparable sizes, which leads to less contact area and thus a smaller friction. In addition, surface adhesive force may make extra contribution to the overall contact area at the macroscale although the effect may be less significant for the textured surfaces.

Figure 3.8 also shows an example of the time history of the COFs obtained from the microscale tests. Due to the comparable size to the pillar spacing, the tip can slide into and out from the troughs between the pillars, which results in a lower friction when it slides in (Figure 3.7 (b), position B) and a higher friction when it travels out because an energy barrier needs to be overcome to climb up (deform) the pillar [34-35], as indicated by Figure 3.7 (b), position C. The tip motion yields a COF fluctuation that corrugates the shape of the surface microgeometry, as shown in Figure 3.8 (a). A similar friction behavior is also observed at the macroscale and the period of the pattern is about 70 μm which corresponds to the period of the texture geometry of

the P3 surface (~24 μm pillar and ~46 μm spacing) (Figure 3.8 (b)). Such a corrugation behavior of the microscopic friction, with respect to the step energy barrier, may also explain why COF for the P1 surface is lower than that those for the others: the tip on the P1 surface experienced lower energy barrier due to its smaller gap space.

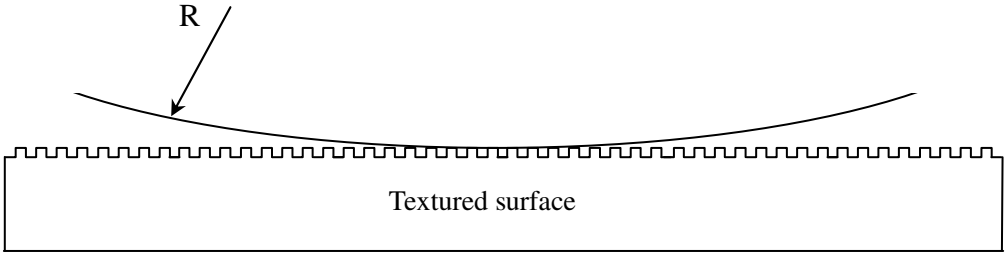

(a) Schematic of the macroscale contact condition using a bearing ball

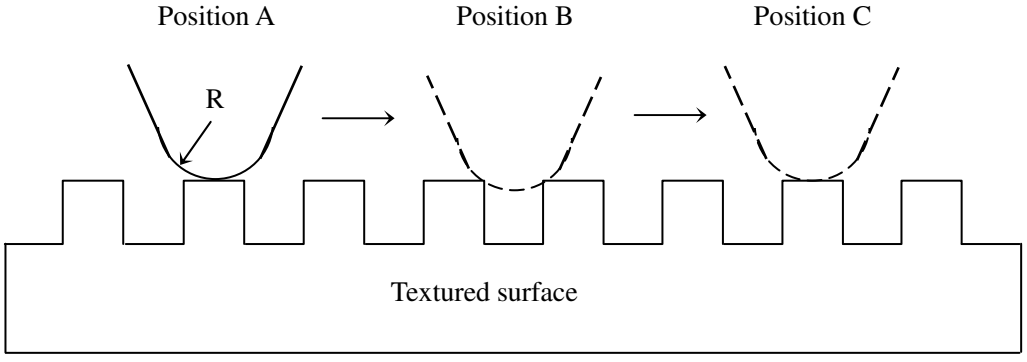

(b) Schematic of the microscale contact condition using a Rockwell diamond tip

Figure 3.7 Schematic of the contact conditions at macro- and microscales

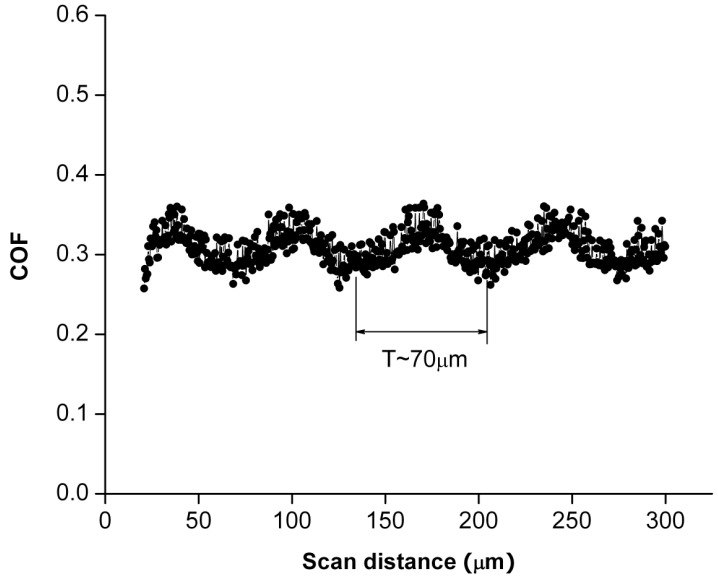

(a) Rockwell tip sliding on the P3 pillar-textured surface

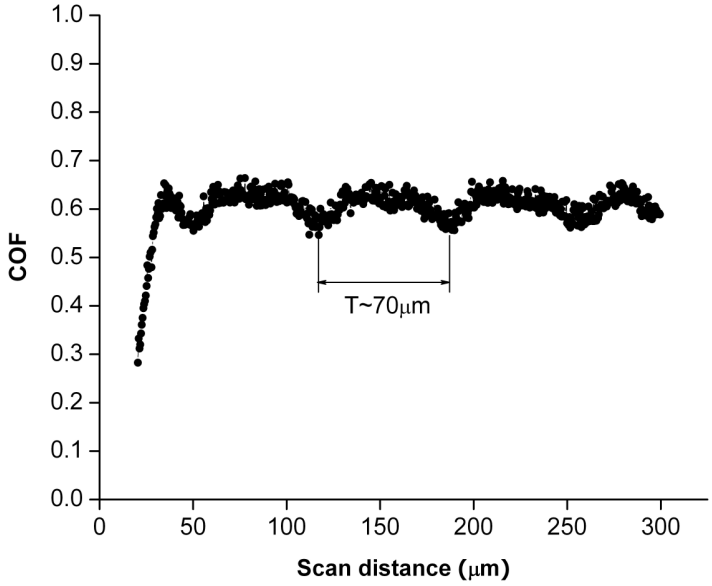

(b) Bearing ball sliding on the P3 pillar-textured surface

Figure 3.8 Time histories of COF under the test conditions of 5mN and 1μm/s on the P3 pillar-textured surfaces using a Rockwell diamond tip and a bearing ball. The period of the pattern, T, is about 70 μm

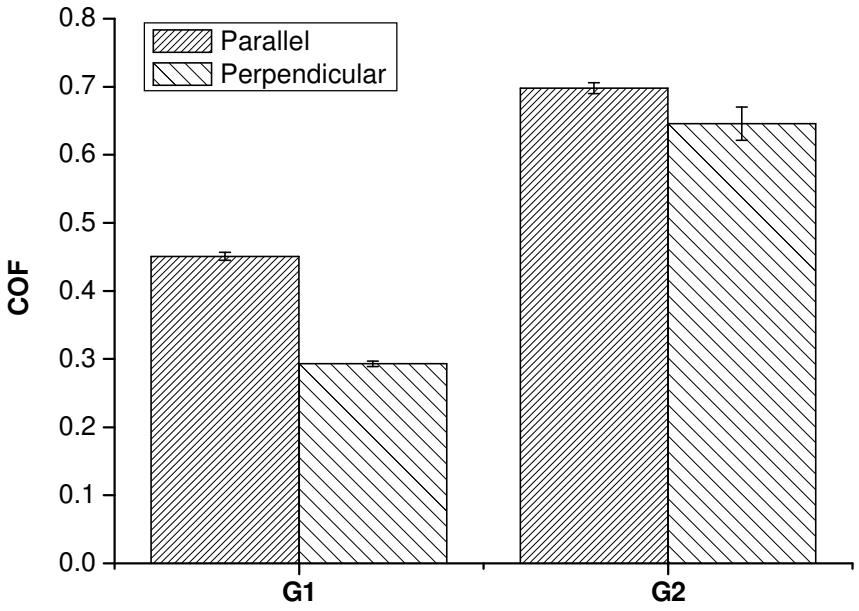

Figure 3.9 COFs for the groove-textured surfaces in the parallel and perpendicular directions obtained from the macroscale tests

3.4 Friction Characterization of Groove-textured Surfaces

3.4.1 Macroscale Friction

Grooves form a texture with completely different features in orthogonal directions. Figure 3.9 shows the friction obtained from the macroscale tests with the bearing ball sliding in the parallel and perpendicular directions on two different groove-textured PDMS surfaces (hereafter referred to as G1 and G2 surfaces) under 10mN normal load and 1μm/s scanning speed. The COFs corresponding to the parallel sliding direction is higher than that to the perpendicular direction for both G1 and G2 surfaces. It has been reported that these two texture

directions are the two extreme cases for the groove-textured surfaces, and the frictions in other directions are expected to lie between these two extreme cases [37-38, 44].

A numerical static friction model of point contact involving rough surfaces, developed by Chen and Wang [107], was used to help understand the friction anisotropic behavior observed in this work. This model is formulated for coupled normal–tangential contact problem with the Boussinesq–Cerruti integral equations, which relate surface tractions to displacements. The upper bound of the normal contact pressure is assumed to be the hardness of the softer material based on the elastic-perfectly-plastic assumption for simplicity. The local shear strength or the upper limit of the shear traction is determined by the hardness of the softer material and local contact pressure. If the shear traction is less than the local shear strength, the local contact area is in stick, otherwise, in slip. The tangential force can then be obtained by summing the shear traction in the entire contact area.

An important factor deserving attention is the maximum stick length. A stick line may be defined as the length of the stick area along the direction of the tendency of motion. The longest stick length may be named as the maximum stick length. Here, the correlation of the maximum stick length with the static friction force should be identified. One may assume that there exists a critical stick length, below which the contact stick area abruptly breaks and full sliding occurs. The static friction force can be defined as the tangential force at the moment when the maximum stick length drops below the critical value. The stick-slip phenomenon is essentially a dynamic process. Considering the fact that the sliding speed used in the experiments is very low (1μm/s), the sliding testing can be treated as a quasi-static process, and a static friction analysis can be applied for a certain period of time. The relationships between the maximum stick length and

tangential force are presented in Figure 3.10, showing that the static friction force along the groove is larger than that cross the groove geometry.

It is also noticed that the COFs for the G1 surface (in both parallel and perpendicular directions) are smaller than those for the G2 surface. This is likely due to the difference in groove dimensions between G1 and G2 surfaces which leads to different contact area when mating with the bearing ball. As shown in Table 3.1, the groove size, a, and spacing, b, of the G1 surface are about 5 and 10μm, while those of the G2 surface are 25 and 25μm, respectively. Therefore, the surface texture density, defined as the ratio of the pattern size over the period, of the G2 surface is about 50%, while that of the G1 surface is only 33%. As a result, G2 surface offers more solid contact within the same contact radius, and this should be one of the reasons for its higher friction.

Figure 3.11 and 3.12 show the time histories of COFs for the G1 and G2 surfaces in the parallel and perpendicular directions obtained from the macroscale tests. The COF curves in the parallel directions for both G1 and G2 surfaces are smooth because there is no topography change along the groove ridge. Friction fluctuation is observed only in the perpendicular direction on the G2 surface and the period of the pattern agrees well with the groove period. The distinct friction behavior in the perpendicular direction between G1 and G2 surfaces is most likely due to the difference of the groove dimensions with respect to the contact dimension.

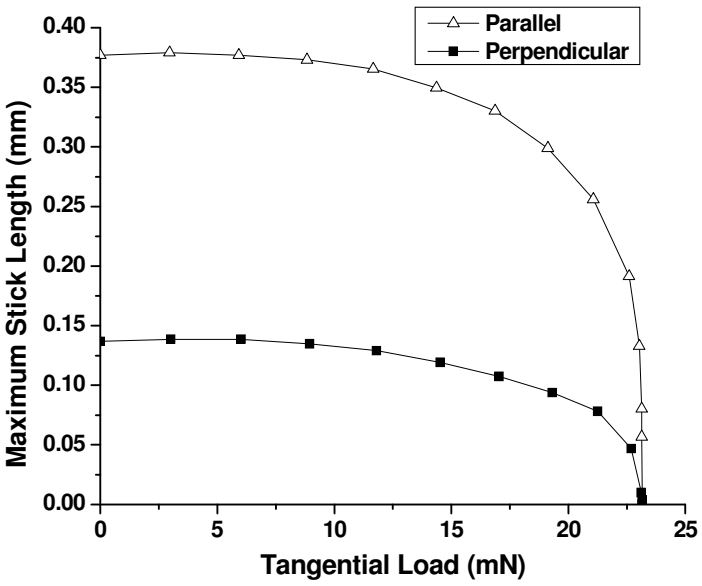

(a) Simulation results of the G1 surface

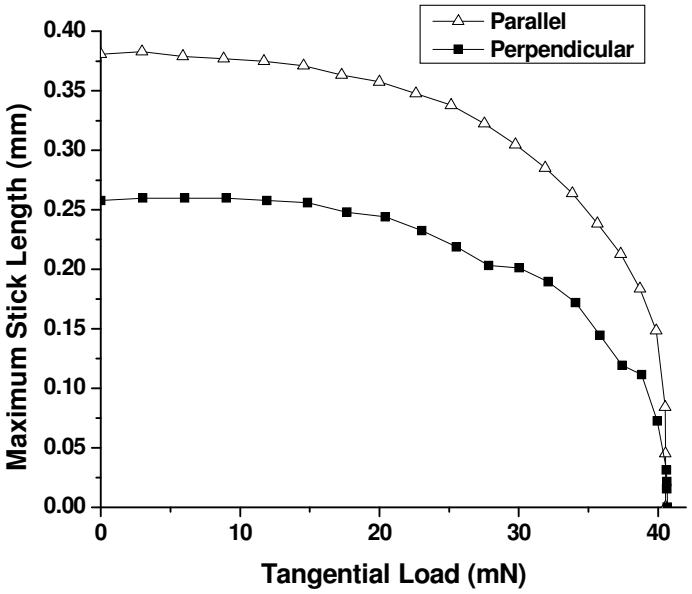

(b) Simulation results of the G2 surface

Figure 3.10 Numerical simulation results of the maximum stick length versus the pre-sliding tangential load in parallel and perpendicular directions of the G1 and G2 surfaces at the macroscale

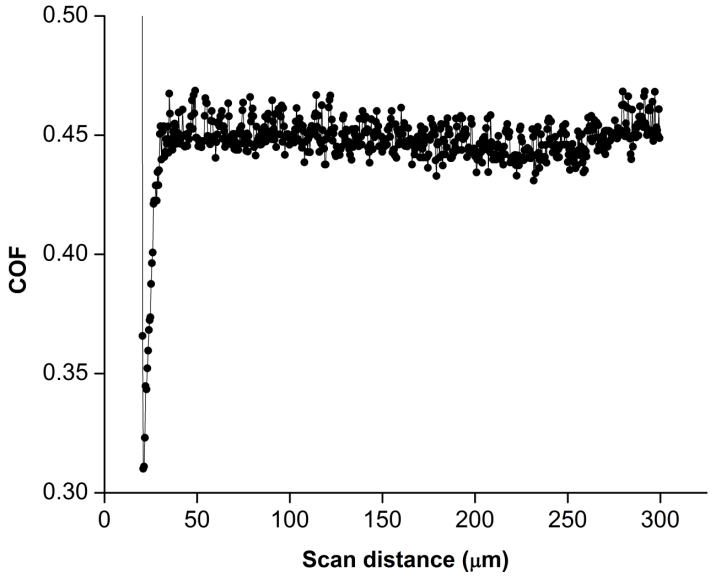

(a) In the parallel direction

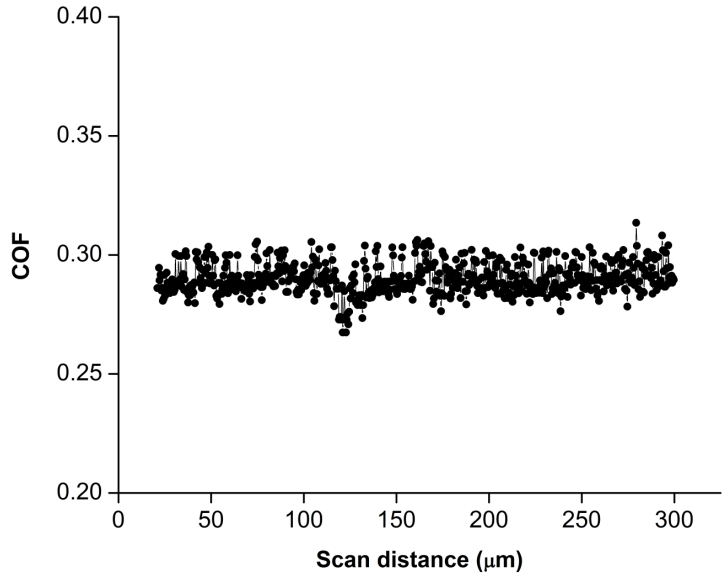

(b) In the perpendicular direction

Figure 3.11 Two examples of the time histories of the COFs for the G1 groove-textured surface in the parallel and perpendicular directions obtained from the macroscale tests under 10mN and 1μm/s

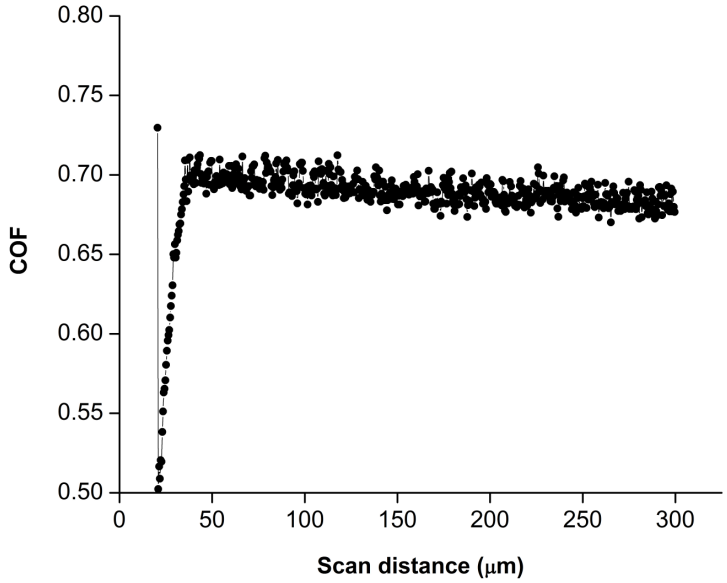

(a) In the parallel direction

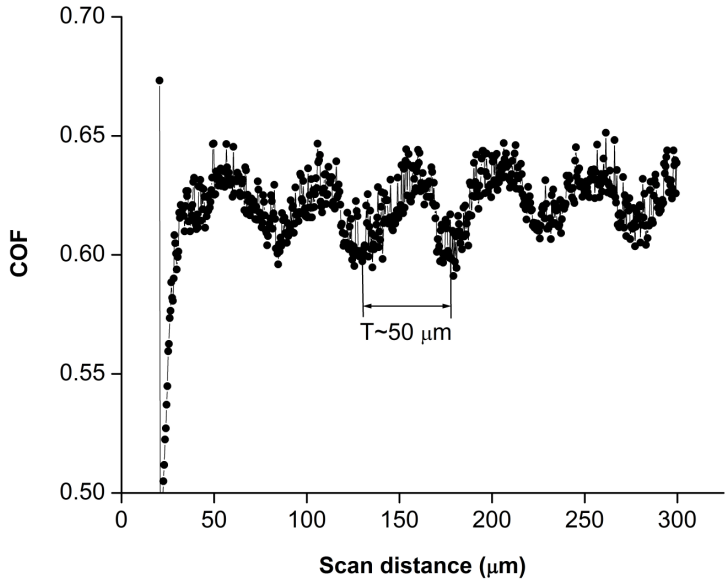

(b) In the perpendicular direction. The period of the pattern, T, is about 50 μm.

Figure 3.12 Two examples of the time histories of the COFs for the G2 groove-textured surface in the parallel and perpendicular directions obtained from the macroscale tests under 10mN and 1μm/s

3.4.2 Microscale Friction

Figure 3.13 shows the friction obtained from the microscale tests with the Rockwell tip sliding in the parallel and perpendicular directions on the G1 and G2 surfaces under the 10mN normal load and 1μm/s scanning speed. Similar friction anisotropy effect can be observed on the G1 surface, that is, the COF in the parallel direction is (slightly) higher than that in the perpendicular direction which is due to the difference in the stick length, as discussed before (see Figure 3.14).

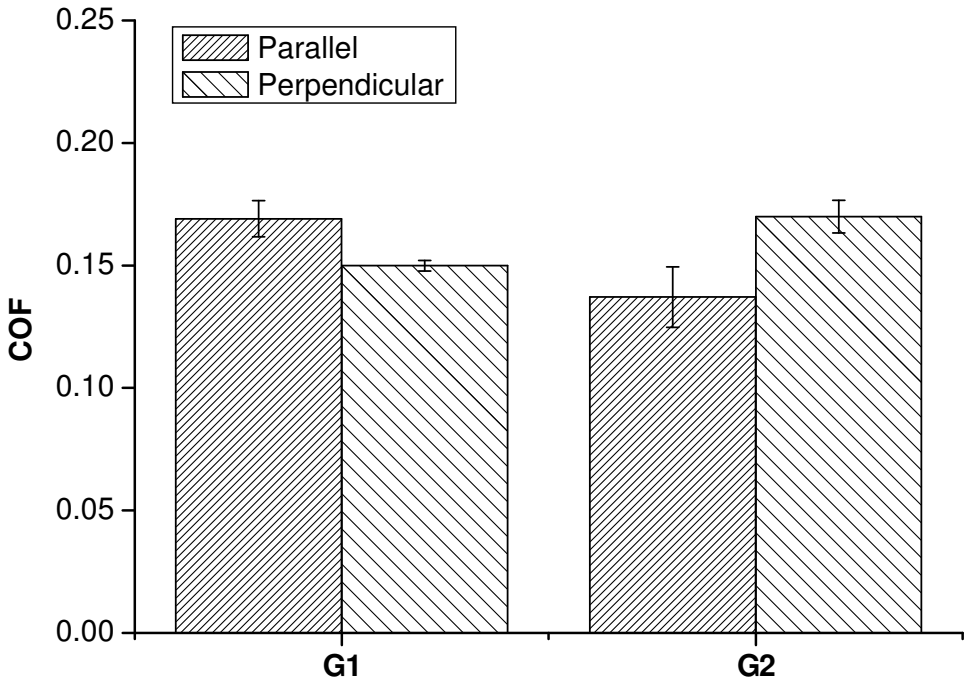

Figure 3.13 COFs for the groove-textured surfaces in the parallel and perpendicular directions obtained from the microscale tests

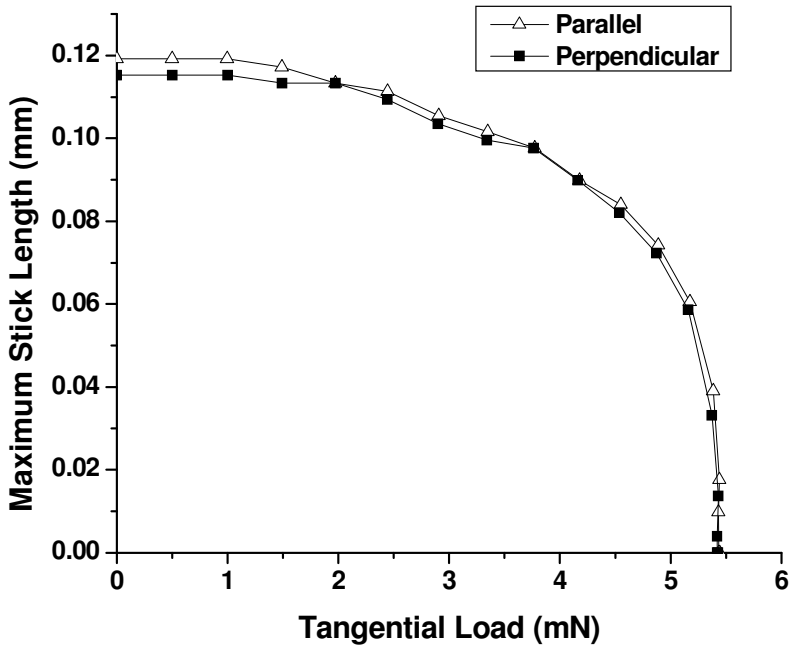

Figure 3.14 Stick length versus the pre-sliding tangential load in parallel and perpendicular directions of the G1 surface at the microscale.

The behavior of the G2 surface is, however, different. The COF in the perpendicular direction is higher than that in the parallel direction. Here the increased corrugation of the surface profile along the direction perpendicular to the groove texture plays a role. It is noted that the tip size is comparable to the texture dimension. Therefore, the increased energy barrier, due to the groove ridges and troughs between them, has to be overcome to initiate sliding, which results in a higher friction. Such friction anisotropy behaviors have been observed on the anisotropic polymer monolayers (diamond-like carbon) where higher nanoscale friction occurs in the more corrugated direction [105]. Molecular dynamic (MD) simulations also predicted that the friction force when sliding parallel to the dimmer row on diamond (001) surfaces (along the

[$\bar{1}$10] direction) yields lower average friction than when sliding perpendicular to the structure (along the [110] direction) [106].

Figure 3.15 and 3.16 show the examples of the time histories of the COFs for the G1 and G2 surfaces in the parallel and perpendicular directions obtained from the microscale tests. Similar trend can be found in both cases. The COF curve is smoother in the parallel direction while more fluctuation is observed in the perpendicular direction, and the periods of the variations correspond to the groove periods.

3.5 Summary

The surface texture effects on friction of PDMS elastomer surfaces were investigated at the macro- and microscales using a nanoindentation-scratching system. It was found that surface textures can significantly reduce COF at the macroscale; however they had less influence on friction at the microscale. The reduction of COF is attributed to reduced contact area for pillar-textured surfaces. Friction anisotropic behavior was observed on the groove-textured surfaces at both macro- and microscales. A numerical model was applied to help understand the friction behavior, and stick length can be correlated to the friction data.

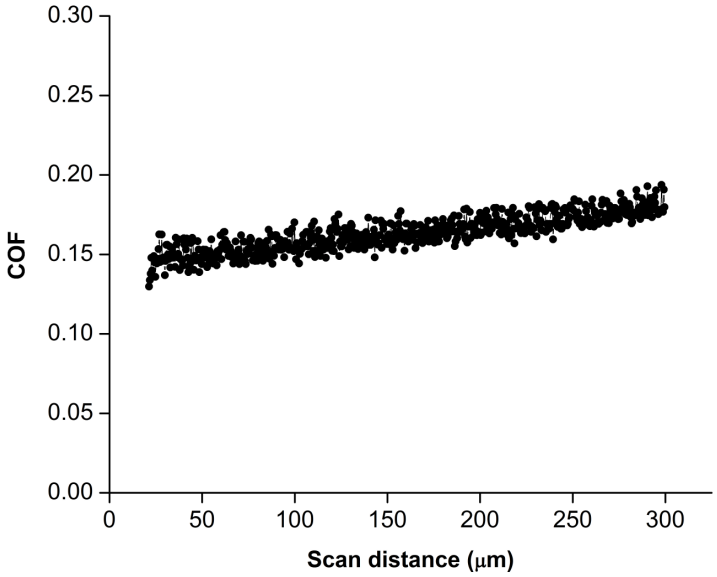

(a) In the parallel direction

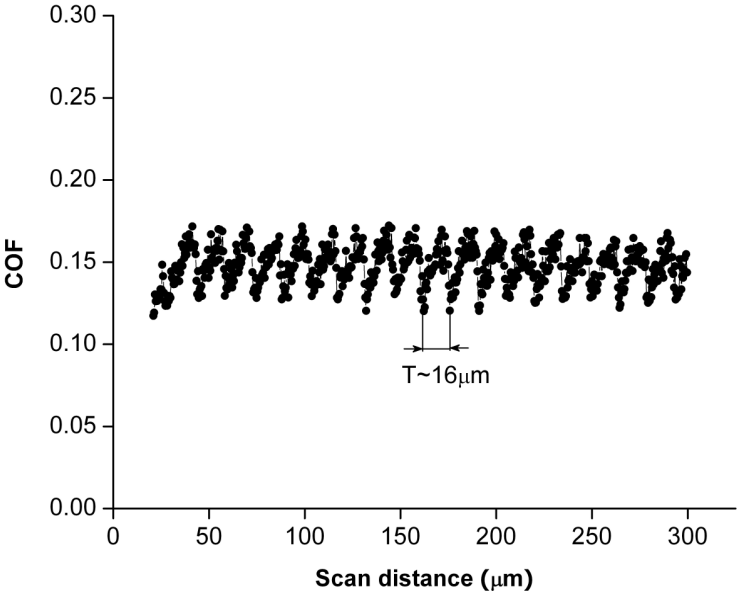

(b) In the perpendicular direction. The period of the pattern, T, is about 16 μm.

Figure 3.15 Two examples of the time histories of the COFs for the G1 groove-textured surface in the parallel and perpendicular directions obtained from the microscale tests under 10mN and 1μm/s

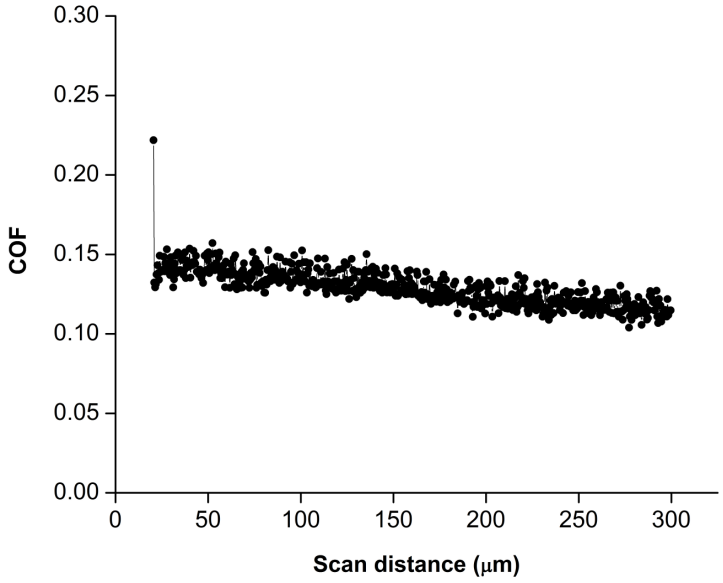

(a) In the parallel direction

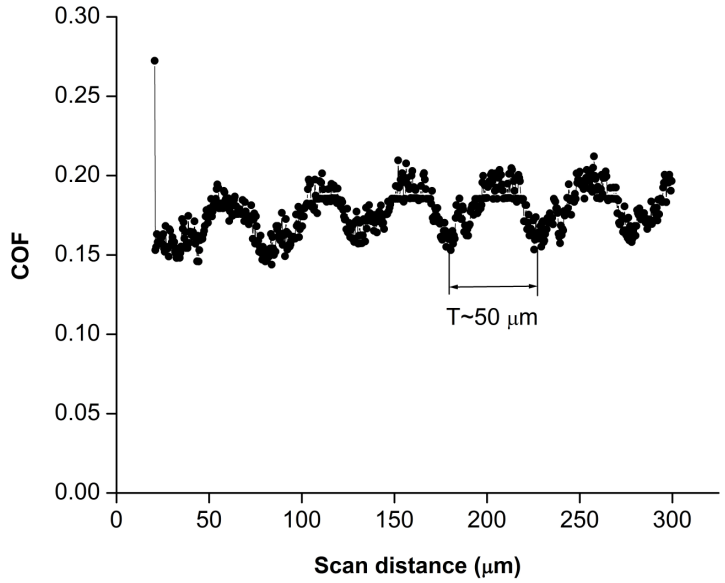

(b) In the perpendicular direction. The period of the pattern, T, is about 50 μm.

Figure 3.16 Two examples of the time histories of the COFs for the G2 groove-textured surface in the parallel and perpendicular directions obtained from the microscale tests under 10mN and 1μm/s

CHAPTER FOUR: MODELING OF HYDROPHOBIC CONTACT ANGLES ON ROUGH SURFACES

4.1 Introduction

Wetting phenomena are essential in a variety of natural and technological processes. Of special interest is the extreme case of superhydrophobic surfaces, on which roughness results in very high water contact angles and very low water roll-off angles. This is usually referred to as the Lotus effect [108], as lotus plant leaves have exhibited this property as a self-cleaning mechanism. There are numerous applications for artificially prepared "self-cleaning" surfaces, such as windows and pained exterior surfaces. In addition, roughness-induced superhydrophobicity is considered a viable option for surface-tension-induced drop motion in microfluidic devices [109].

The above two requirements of superhydrophobic surfaces, namely, very high water contact angles and very low water roll-off angles, are closely related but not necessarily equivalent. In particular, the mechanism of roll-off is not yet fully understood. However, complete understanding of this dynamic process can be achieved only if its starting point, the equilibrium state of a drop on a hydrophobic surface, is well understood. The present research focuses on the conditions for existence of the possible energy states on rough hydrophobic surfaces.

Section 4.2 introduces some earlier modeling work and the major assumptions. Section 4.3 discusses the matching experimental results which indicate the existence of multiple equilibrium drop shapes on a rough substrate. Issues pertaining to different models for advancing

and receding contact angles, which may be the essential factor in the water roll-off phenomenon, will be discussed in Section 4.4, and the wetting behavior on a substrate with anisotropic roughness features will be explained in Section 4.5.

4.2 Theory

When a drop sits on a flat homogenous substrate, a definite angle (θ_e, hereafter referred to as contact angle) is usually formed between the liquid, vapor and solid phases (Figure 4.1). Through force balance, the following relationship can be obtained:

$$\cos\theta_e = \frac{\gamma_{SV} - \gamma_{SL}}{\gamma_{LV}} \tag{4.1}$$

where γ_{SV}, γ_{SL}, and γ_{LV} are the surface tensions of solid-vapor, solid-liquid, and liquid-vapor contacts, respectively [110]. This is knows as Young's equation.

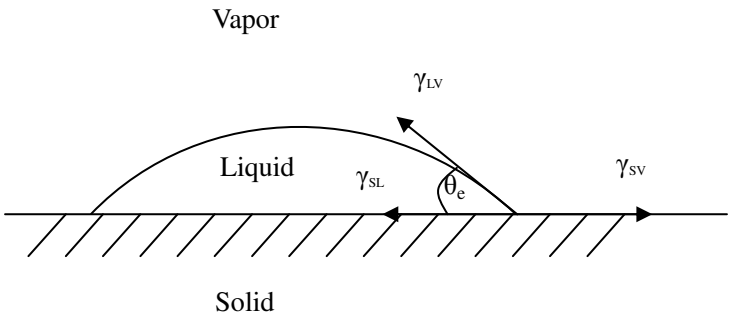

Figure 4.1 Scheme of wetting of a drop on a flat substrate

The problem of determining the equilibrium conditions of a drop on a rough surface is well-known as a problem of minimization of the Gibbs energy of the system, while constraining the drop volume to a fixed value [53, 111]. The energy of the drop of a given volume in equilibrium on a rough substrate is given by

$$\frac{G}{\sqrt[3]{9\pi}V^{2/3}\gamma_{LV}} = \left(1-\cos\theta_r\right)^{2/3}\left(2+\cos\theta_r\right)^{1/3} \tag{4.2}$$

where G is the Gibbs energy of the system, V is the volume of the drop, and θ_r is the contact angle on the rough substrate. The left-hand side denotes the nondimensional energy. It can be easily verified that the right-hand side is a monotonically increasing function of θ_r for $0° < \theta < 180°$. As a result, an equilibrium drop shape with a lower value of the apparent contact angle θ_r will have a lower energy.

The earliest work to model the shape of a stationary drop on a rough substrate can be attributed to Wenzel and Cassie.

In Wenzel's theory, it is assumed that a liquid completely fills the depressions in the region of its contact with a rough substrate (Figure 4.2(a)). This will be referred to as the wetted contact with the rough surface. The apparent contact angle is given by

$$\cos\theta_r^w = r\cos\theta_e \tag{4.3}$$

where θ_r^w represents the apparent contact angle on the wetted surface and r is the ratio of the actual area of the rough surface to the projected area [51].

In Cassie's theory, it is assumed that a composite surface is formed, i.e., liquid is completely lifted up by the roughness features (Figure 4.2(b)). This will be referred to as the composite contact with the rough substrate. In this case

$$\cos\theta_r^c = -1 + \varphi_s(\cos\theta_e + 1) \tag{4.4}$$

where θ_r^c represents the apparent contact angle on the composite surface and φ_s is the area fraction of the solid surface [52].

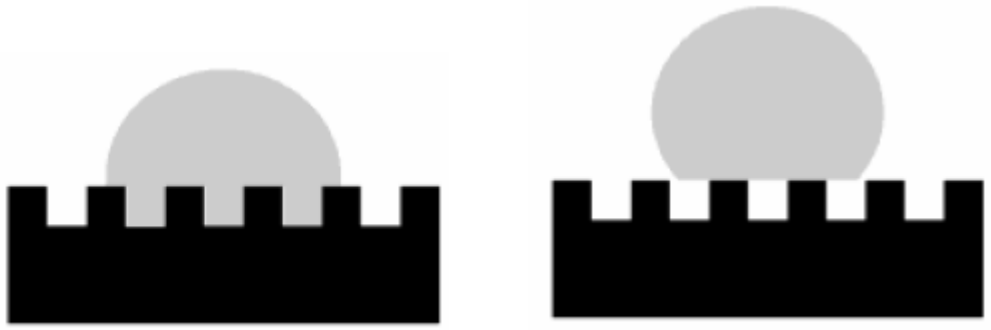

(a) Filled-up grooves (wetted contact) (b) Composite contact

Figure 4.2 (a) A droplet fills the grooves of the rough surface. (b) The drop sits on the rough patterns forming a composite surface

In formulating the detailed expression for Wenzel and Cassie equations through minimization of the Gibbs energy of the system, it is assumed that the drop is sufficiently large compared with the typical scale of roughness. This assumption has two important implications: (a) Gravity does not play a significant role in determining the shape of the drop either in the Wenzel or in the Cassis state; (b) The radius of curvature of the liquid-air interface inside the grooves must equal the radius of the drop everywhere else (that is, very large); therefore, it is assumed that this interface is approximately planar. These are explained in more details in the following.

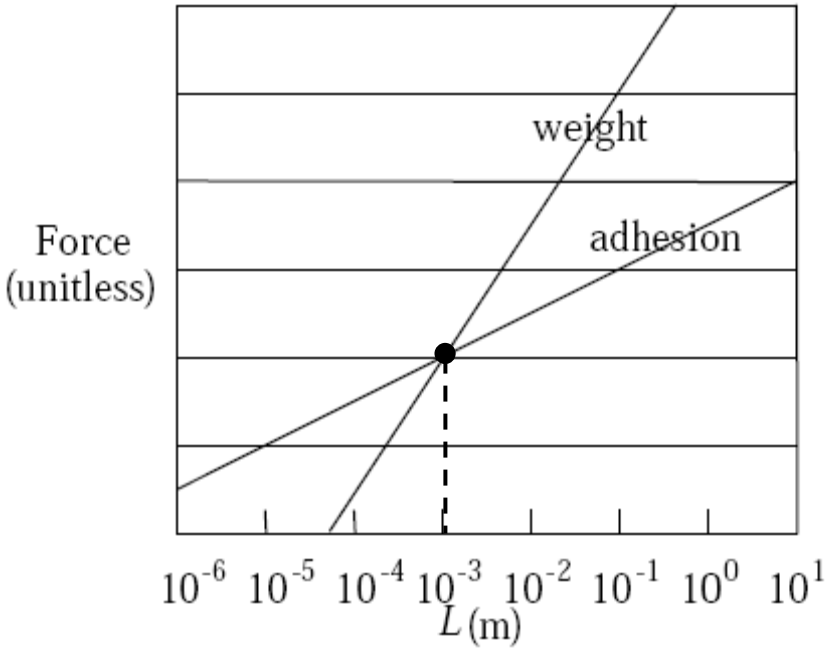

Figure 4.3 Scaling of weight and molecular adhesion (Adapted from [112])

Being a unique type of force scaling directly to length (line force), surface tension becomes dominant over body force when the dimension of interest shrinks down to the micrometer scale. Figure 4.3 [112] shows that once the length scale is smaller than the one corresponding to the intersection point which is on a scale of millimeters, surface tension is higher than body force and becomes more dominant as the dimension shrinks further down. In order to better understand the conditions under which the assumption that gravity is negligible during droplet shape modeling is valid, the following dimension analysis is conducted using a water droplet in spherical shape as an example.

The surface tension force, F_s, of a spherical droplet in air is given by

$$F_s \propto \gamma_{LV} R \tag{4.5}$$

where γ_{LV} is the surface tension of liquid–vapor contact, in this case, water–air contact, R is the radius of the droplet.

The weight of the droplet is given by

$$F_G = mg = \rho V g \propto \rho R^3 g \tag{4.6}$$

where ρ is the density of water, V is the volume of the droplet, and g is the gravitational acceleration.

Equating equation (4.5) and (4.6) results in the known capillary length, a_{cap} [113]

$$a_{cap} = \sqrt{\frac{\gamma_{LV}}{\rho g}} \tag{4.7}$$

When the droplet radius R is much smaller than the capillary length, surface tension is dominant and the gravity effect is negligible. For water, a_{cap} = 2.7mm; a spherical water droplet of radius a_{cap} weights 82mg. Thus, the water drop should be smaller than 82mg for the gravity effects to be of little significance in determining the shape of the Wenzel and Cassie drops. The volume corresponding to the critical mass of a water droplet is 82μL. This number will be compared with the size of the droplet used in this work.

The above condition can also be restated in terms of a nondimensional parameter. The Bond number, B_0, is defined as the ratio of body force to surface tension force [113]. In this case,

$$B_o = \frac{\rho g R^2}{\gamma_{LV}} \tag{4.8}$$

The Bond number is a measure of the importance of surface tension forces compared to body forces. A low number, typically much smaller than one, indicates surface tension dominates, and thus the effect of gravity is negligible in the droplet shape analysis.

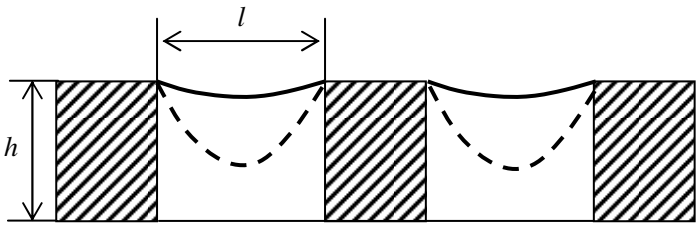

Figure 4.4 Side view of the liquid-vapor interface of a Cassie drop. Solid lines represent the case that the droplet size is much larger than the roughness size. Dashed lines represent the case that the sizes of the droplet and roughness are comparable

Another implication of the assumption is that the liquid–vapor interface inside the grooves underneath the liquid is flat. Consider a microscopic view of the contact between the drop and the rough surface. Since the curvature of the drop must be constant everywhere, for a Cassie drop, the liquid–vapor interface does have a curvature of the order of the radius of the drop (solid line in Figure 4.4) in order to satisfy local equilibrium of the Young-Laplace equation, $\Delta P = \frac{2\gamma_{LV}}{R}$, where ΔP is the Laplace pressure across the liquid–vapor interface, and R is the radius of the drop [110]. It can, however, be ignored when the drop size is much larger than the roughness size. Therefore, the interface can still be considered a planar surface in this case. However, when the sizes of the droplet and roughness feature are comparable, this assumption is no longer valid. The curvature of the liquid–vapor interface increases with reduced drop volume (dashed line in Figure 4.4) and a liquid–solid contact at the bottom of the valley may even be formed (a wetted contact) when the size of the droplet is small enough. Reyssat and Quéré [114]

have demonstrated that such a transition can occur as a drop evaporates. A critical radius R^*, below which the drop will transit from Cassie to Wenzel's state, is related to the geometric parameters of the roughness feature as $R^* \sim l^2 / h$, where l and h are the spacing and height of the texture. Apparently, for smaller texture (small h) and/or larger spacing (large l), the critical radius R^* can become quite large.

4.3 Multiple Equilibrium Energy States on Rough Hydrophobic Surfaces

4.3.1 Introduction

As previously discussed, the contact angle on a rough surface is modeled by either Wenzel or Cassie's formula. However, they predict different contact angles for a droplet on the same rough surface. Neither the aforementioned experiments nor previous literature are conclusive regarding which of the two theories correctly models the contact angle on a rough surface. Some research groups have compared experimental observations with these two theories. Onda *et al.* prepared fractal surfaces and compared the measured contact angles with the predictions from Wenzel's theory. Some agreement with the theory was claimed [115-116]. Bico *et al.* prepared substrates of a specified surface roughness and compared the observed contact angles with Cassie's theory. Good agreement was claimed [58].

Patankar's recent theoretical analysis [53] shows that there can exist two distinct contact angles on the same rough surface. Both are stable equilibrium positions, that is, they offer local minimum energy states, but one has a lower energy than the other. It was shown that a droplet with a lower apparent contact angle has a lower energy overall or is at the global minimum.

Whether a wetted surface or composite surface offers the global minimum energy depends on the geometric parameters of the surface. However, it is not guaranteed that the droplet will always go to the global minimum. It will depend on how the droplet is formed, that is, the droplet may form a composite surface that may be at a local minimum with a higher energy than that of the droplet formed with a wetted surface [53].

To move from one equilibrium position to the other, the interface between the droplet and surface must overcome an energy barrier. In fact, Bico *et al.* reported that they observed the contact angles change from that corresponding to a composite surface to that of a wetted surface when a droplet was physically squeezed [58]. The fundamental understanding of this bistable rough surface is critical in designing a substrate with maximum superhydrophobicity.

Figure 4.5 shows a geometry of square pillars of size a×a, height H, and spacing b, arranged in a regular array. The equilibrium contact angle θ_e on the flat surface is given. Therefore, the contact angle, according to Wenzel's and Cassie's formulas, is a function of the geometric parameters of the surface. The expressions are given by [117]:

$$\cos\theta_r^c = A(1+\cos\theta_e) - 1 \tag{4.9}$$

$$\cos\theta_r^w = \left[1 + \frac{4A}{(a/H)}\right]\cos\theta_e \tag{4.10}$$

where $A = \dfrac{1}{(b/a + 1)^2}$

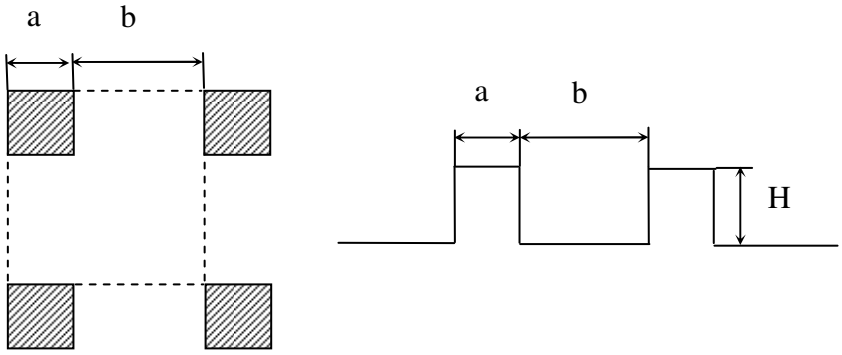

Figure 4.5 Top and cross-sectional views of a roughness geometry of square pillars

Figure 4.6 shows a sketch of a theoretically predicted contact angle as a function of the geometric parameter b/a [117]. The lower energy segments (i.e., the segments with the lower value of the contact angle) of the Wenzel and Cassie curves are marked in Figure 4.6. The intersection point between the Wenzel and the Cassie curves denotes the maximum value of the contact angle (for a given value of a/H and θ_e) among all the possible lower energy states. It is clear from Figure 4.6 that, when the contact angles from the two theories are the same, there is no change in the contact angle even if there is a transition from a composite to a wetted surface or vice versa. This is the critical point that can be used to design a robust superhydrophobic substrate for given values of θ_e and a/H [53]. An equivalent condition for the design point is that the energies of the composite and wetted surfaces are the same:

$$\gamma_{SL}\left|(a+b)^2+4aH\right| = \gamma_{SL}a^2+\gamma_{LV}(b^2+2ab)+\gamma_{SV}(b^2+2ab+4aH) \tag{4.11}$$

The left–hand side is the total surface energy of the wetted (Wenzel) surface, and the right–hand side is that of the composite (Cassie) surface for the same surface area on the projected plane. Substituting Young's equation (4.1) into equation (4.11), the following equation can be obtained:

$$\cos\theta_e = \frac{1}{\left[\frac{4A}{(a/H)(A-1)} - 1\right]} \tag{4.12}$$

This formula gives the relationship between the equilibrium contact angle θ_e and the geometric parameters at the critical point. This section first experimentally verifies the existence of the two distinct contact angles for a droplet on a given rough surface; second, it is confirmed that a robust hydrophobic rough surface can be designed such that the contact angles given by Wenzel's and Cassie's formulas are the same.

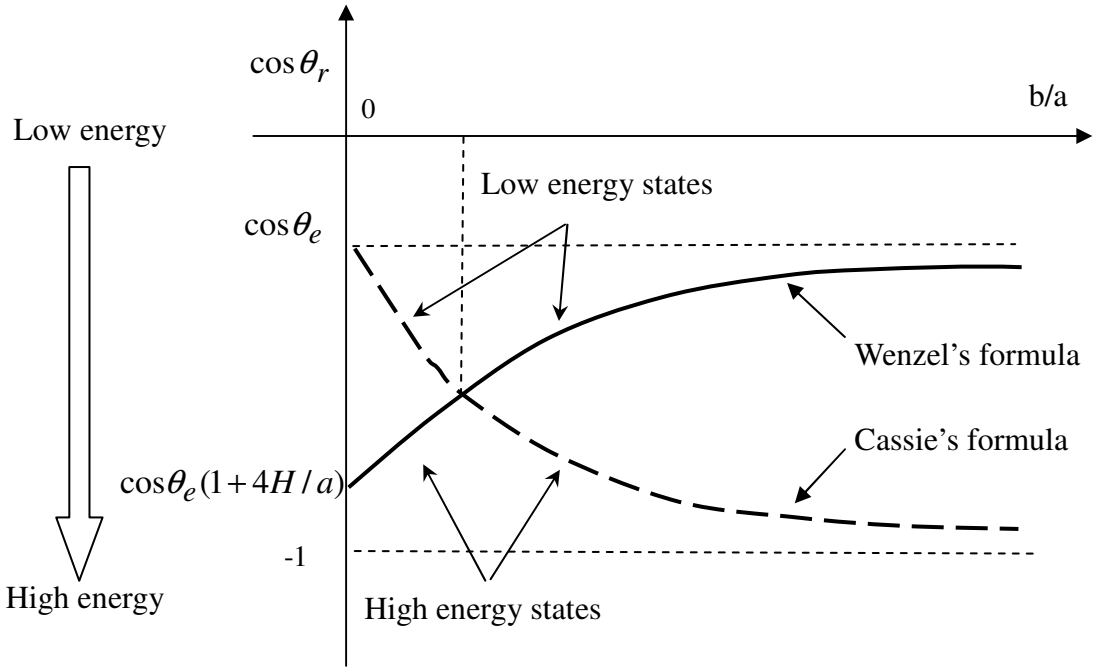

Figure 4.6 Sketch of the theoretically predicated contact angles as a function of the geometric parameter b/a. The values of θ_e and a/H are assumed to be given. The value of θ_r is the contact angle on a rough surface modeled either by either Wenzel's or Cassie's formula

4.3.2 Experiment Details

Rough surfaces with square pillars of different dimensions were fabricated by the micromachining techniques [94]. The fabrication process was illustrated in Figure 3.1 and details

were given in Chapter 3.2. The desired thickness of the SU-8 mold is 30 μm. The processing parameters were tuned to accurately achieve the desired SU-8 layer thickness. After they were made, the PDMS rough surfaces were sputter-coated with gold and imaged by scanning electron microscopy (SEM, Hitachi S-4500).

The contact angle measurement was conducted by a goniometer (AST Products Inc, VCA Optima XE, Boston, MA, USA) that takes and analyzes the image of a stationary droplet on a surface. Two measurements were taken for each rough surface fabricated. In the first measurement, a droplet was gently deposited by a motorized pipet. A higher contact angle (θ_1) was obtained. In the second measurement, a droplet was dropped from some height. In this case, it was observed that a lower contact angle (θ_2) was formed.

4.3.3 Contact Angle Measurements of Wenzel's and Cassie's Drops

Figure 4.7 shows the SEM images of the rough surface made of PDMS. A well-ordered array of pillars is observed. Five kinds of rough surfaces with the pillar structures of different dimensions were fabricated to verify the theoretical prediction. Table 4.1 lists the geometric parameters. Each surface is identified as a data point, numbered one through five, corresponding to the five values of the geometric parameter b/a. Among the five dimensions (for b/a) considered in this experiments, three are on the right side of the critical point where the wetted surface offers the global energy minimum whereas two are on the left side of the critical point where the composite surface offers the global energy minimum (see Figure 4.6) [117].

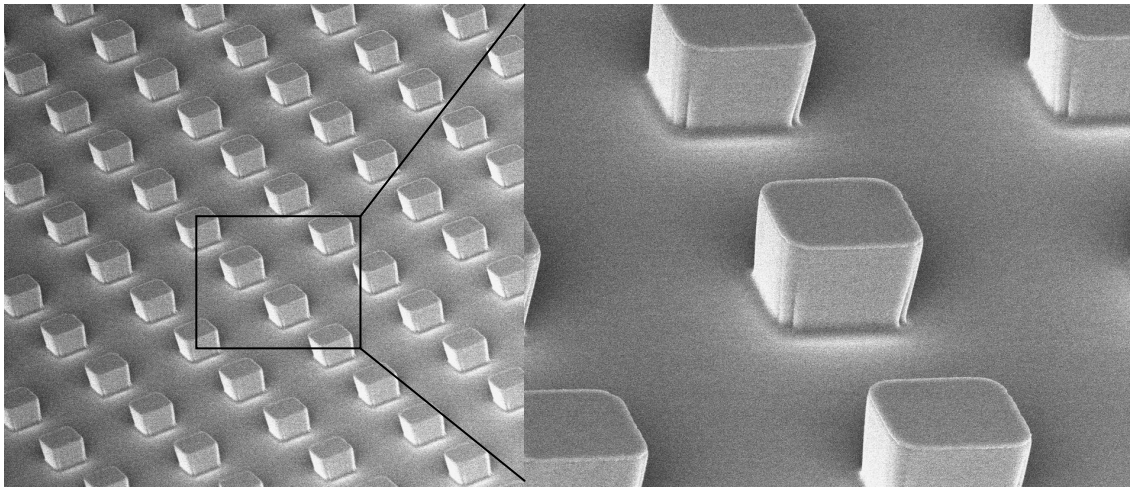

Figure 4.7 SEM images of the pillar structures made of PDMS

Table 4.1 Geometric parameters of five PDMS rough surface with different dimensions (a/H=0.83)

Data point	Original design (μm)	Measurement (μm)
1	a=25, b=80 b/a = 3.2	a=23.7,b=79.8 b/a = 3.37
2	a=25, b=45 b/a = 1.8	a=22.9, b=44.2 b/a = 1.93
3	a=25, b=28 b/a = 1.12	a=22.7, b=28.7 b/a = 1.26
4	a=25, b=16 b/a = 0.64	a=23.4, b=16.8 b/a = 0.72
5	a=25, b=8 b/a = 0.32	a=23.3, b=8.6 b/a = 0.37

Figure 4.8 shows the images of the droplets sitting on the rough surface with the largest b/a ratio (b/a = 3.367; data point 1). In this geometry, the wetted surface is at the lower energy state (i.e., lower contact angle). Figure 4.8(a) shows the case when the water droplet was gently

deposited on the rough surface. It is clearly seen that light can pass through the space in the depressions of the rough surface, which indicates that a composite surface is formed. The measured contact angle, as is seen in Table 4.2, is closer to the value predicted by Cassie's formula, which is based on the hypothesis of a composite surface. Figure 4.8(b) shows the contact angle measurement after the droplet was dropped from some height onto the same surface. Light cannot be seen between the droplet and the rough surface. This indicates that the liquid fully wets the depressions of the rough surface. Again, the measured contact angle is indeed closer to that predicted by Wenzel's formula based on the hypothesis of a wetted surface. The direct observation of the presence of a composite surface or a wetted surface confirms the hypotheses upon which Wenzel's and Cassie's formulas are based. This observation agrees with the expectation for the specified case that a composite drop will be formed if deposited gently on the substrate and a wetted drop will be formed if dropped from a height [117].

It can also be seen in Figure 4.8(a) that the liquid–air interface is approximately flat. As discussed before, when the water droplet volume is less than 82μL, surface tension force is larger than gravity. In the experiments, the volumes of the drops used are all less than 10μL, which suggests that gravity can be ignored, and thus the liquid–air interface can be treated as a planar surface. In addition, the direct observation of the flat liquid–vapor interface also confirms that the drop size is big enough so that the Laplace pressure does not drastically change the curvature of the liquid–air interface. As shown before, the critical drop radius R^* is proportional to l^2/h [114]. The largest l listed in Table 4.1 is data point 1 where l = 80μm (h = 30μm for all five surfaces). This gives a critical radius of $R^* \approx$ 213μm and the corresponding drop volume is about 0.04μL which is much smaller than the volume of the drop used in the experiments.

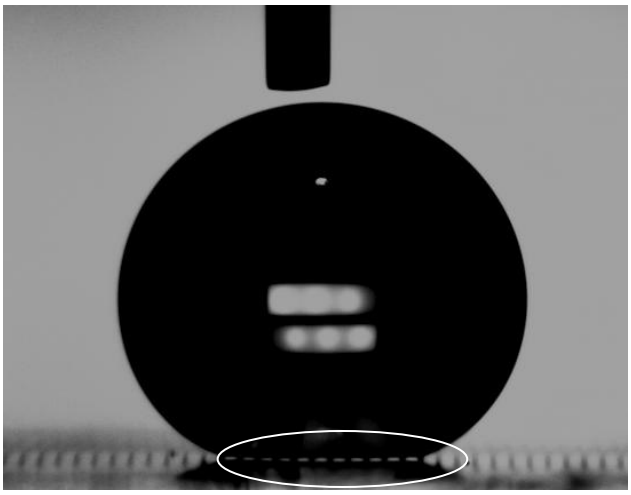

(a) A composite surface, volume=6.002 μL

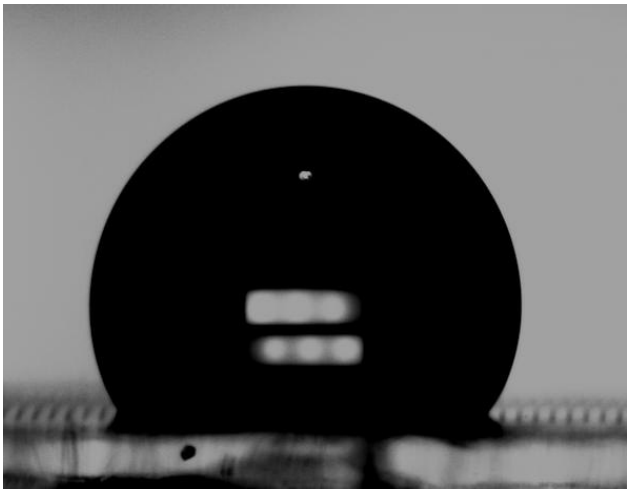

(b) A wetted surface, volume=7.716 μL

Figure 4.8 Direct observations of composite and wetted surfaces

According to the theoretical prediction, the contact angle of the composite drop should be larger than that of the wetted drop for data points 1-3 because in these cases the b/a ratio is such that the wetted drop has a lower energy. Indeed, it is observed that for these cases when the drop

is placed gently (and forming a composite drop) the contact angle is larger than when dropped from some height.

Table 4.2 Comparison of six theoretical predictions with the experimental results

Data points	Theoretical $\cos\theta^c$ (˚)	Theoretical $\cos\theta^w$ (˚)	Experimental (˚)
1	θ^c_{static} : 165.7	θ^w_{static} : 121.0	$\theta_1 = 152.5$ $\theta_2 = 123.4$
	θ^c_{adv} : 166.5	θ^w_{adv} : 126.4	
	θ^c_{rec} : 161.0	θ^w_{rec} : 87.5	
2	θ^c_{static} : 158.6	θ^w_{static} : 130.9	$\theta_1 = 149.5$ $\theta_2 = 136.8$
	θ^c_{adv} : 159.8	θ^w_{adv} : 139.1	
	θ^c_{rec} : 151.6	θ^w_{rec} : 86.8	
3	θ^c_{static} : 152.1	θ^w_{static} : 145.9	$\theta_1 = 148.3$ $\theta_2 = 140.1$
	θ^c_{adv} : 153.7	θ^w_{adv} : 162.8	
	θ^c_{rec} : 142.9	θ^w_{rec} : 85.9	
4	θ^c_{static} : 143.1	θ^w_{static} : 180	$\theta_1 = 147.1$ $\theta_2 = 131.6$
	θ^c_{adv} : 145.2	θ^w_{adv} : 180	
	θ^c_{rec} : 130.6	θ^w_{rec} : 84.5	
5	θ^c_{static} : 133.1	θ^w_{static} : 180	$\theta_1 = 147.2$ $\theta_2 = 125.6$
	θ^c_{adv} : 135.8	θ^w_{adv} : 180	
	θ^c_{rec} : 116.6	θ^w_{rec} : 82.5	

Data points 4 and 5 are on the left side of the theoretically determined critical point, where the composite surface has a lower energy. From Patankar's analysis, a lower contact angle, which corresponds to a composite surface, should be obtained by gentle deposition. A higher contact angle, which corresponds to the wetted surface, should be obtained by dropping a

droplet from some height. However, the experimental measurement showed opposite results. The reason for this contradiction may be due to contact angle hysteresis. Also, it is believed that the two contact angles may both be the ones resulting from a composite surface. This is explained in more detail in the following [117].

There is usually an advancing contact angle θ_e^{adv} and receding contact angle θ_e^{rec} on a flat surface depending on whether a given drop is formed by an advancing front (i.e., a drop formed by increasing its volume) or a receding front (i.e., a drop formed by decreasing its volume), respectively. The value of the difference between the advancing and receding angles is usually called contact angle hysteresis. The static contact angle θ_e, obtained by simply placing a drop of a given volume on a surface, could be a number between the advancing and receding angles. The advancing, receding, and static contact angles on the flat PDMS surface were measured to be 118°, 88° and 114°, respectively. This could influence the observed contact angle on a rough substrate.

Table 4.2 lists the theoretical predictions for the composite and wetted cases by using θ_e, θ_e^{adv} and θ_e^{rec} in place of θ_e in equations (4.3) and (4.4). This leads to six theoretical values for each data point. In Table 4.2, the superscript (c or w) denotes which formula (Cassie's or Wenzel's) is used. The subscript (static, adv, or rec) denotes which contact angle on the flat surface (θ_e, θ_e^{adv} or θ_e^{rec}) is substituted into equations (4.3) and (4.4).

It was found, through comparison of the six theoretical predictions with the experimental measurement results for each case, that for data points 1 and 2, the larger contact angle (θ_1), obtained from gentle deposition, is closer to that predicted by the composite theory and the lower contact angle (θ_2), obtained from deposition from a height, is closer to that predicted by

Wenzel's theory. In addition to the direct evidence showed previously, it can be concluded that, in these cases, the composite surface is formed by gentle deposition of the droplet and the wetted surface is formed when the droplet is dropped from some height. A similar conclusion may be extended to data point 3, although the quantitative agreement is less compelling.

For data points 4 and 5, it was found that both θ_1 (gentle deposition) and θ_2 (deposition from a height) are closer to the angles predicted by the composite theory. The value of θ_1 is closer to the value predicted by substituting the advancing or static contact angle of the flat surface into Cassie's formula. The value of θ_2 is closer to the value predicted by substituting the receding angle of the flat surface into Cassie's theory. This indicates that in both the gentle and the dropped depositions a composite surface is most likely formed. The nature of the drop formation (i.e., gentle or dropped from a height) determines which of the angles of the flat surface (i.e., advancing, receding, or static) become relevant in predicting the angle of the composite drop on the rough surface. It must be noted that for data points 4 and 5 the wetted case has a higher energy. As a result, even if the drop is deposited from some height it may not have a sufficient energy to go to the wetted shape, thus forming a composite surface even when dropped from a height. Instead, the droplet at once spread as a result of the impact when the dropping occurred, would shrink or recede to form the final shape. This explains why the receding contact angle is observed when the droplet is dropped.

Figure 4.9(a) shows $\Delta\theta\left(=\left|\theta^{c}_{static}-\theta^{w}_{static}\right|\right)$ as a function of the geometric parameter b/a based on the theoretical prediction. Figure 4.9(b) depicts the experimental measurement $\Delta\theta$ $(=\left|\theta_1-\theta_2\right|)$ as a function of the geometric parameter b/a for data points 1-3. It is seen that the

same trend of the relationship between Δθ and b/a can be found in these two plots. As b/a decreases from a higher value, Δθ decreases and goes to 0 at the critical point. Although a substrate with Δθ = 0º was not obtained experimentally, the trend clearly indicates that such a rough surface could be designed [117].

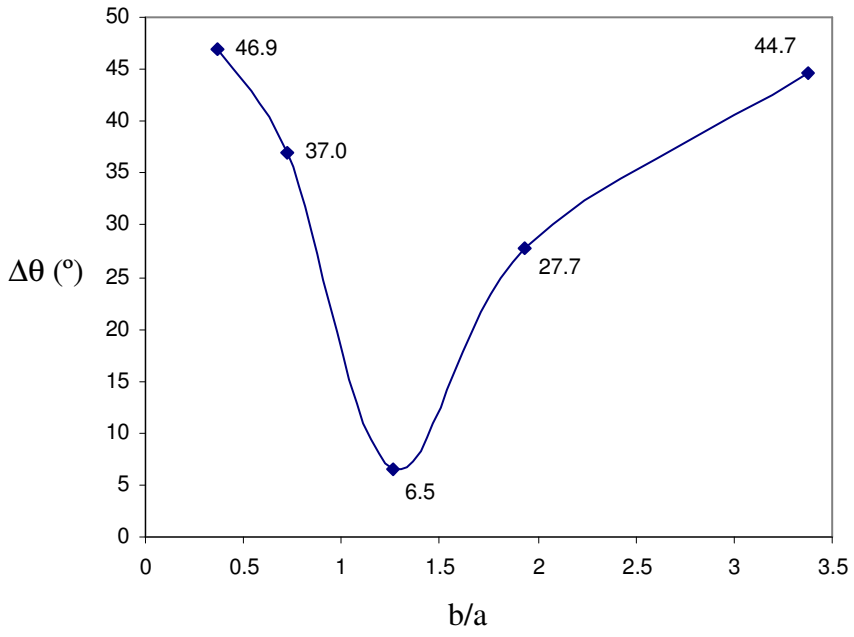

(a) Theoretical prediction

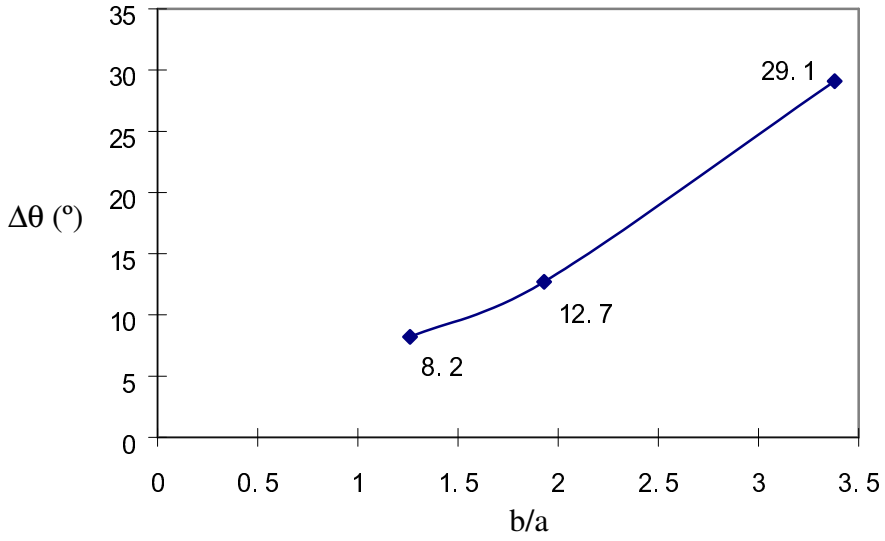

(b) Experimental results

Figure 4.9 Relationship of Δθ as a function of the geometric parameter b/a

The above experimental observations support the design criterion for a robust superhydrophobic surface proposed by Patankar [53]. A well-designed robust superhydrophobic surface should be the one where the contact angle does not change. The above experiments confirm the existence of such a surface. This fact is critical in microfluidic applications, where a rough surface is used for the applications based on wettability amplification. If the contact angle changes as a result of a transition, it can result in different surface characteristics. To avoid a significant contact angle change due to external disturbances, the surface should be designed to fulfill the above criterion. Furthermore, the value of the contact angle should be as close to 180° as possible to achieve maximum superhydrophobicity.

It is noted that the theoretical predictions rely on an assumption that the rough patterns should be infinitesimally small compared to the sizes of the droplet. In this case, there are around 100 pillars (10 in each direction) in the base area of the droplet. Therefore, the contact angle may not be simply predicted by either Wenzel's or Cassie's theory. This size effect may be important to explain the more detailed behavior, for example, the deviation between the theoretical predictions and experimental measurement in Figure 4.9 [117]. Applications of larger drops or smaller roughness features are two viable solutions to this problem. The former is limited by the instrument, where a drop with a volume more than 15μL is too big to image. The latter requires special fabrication techniques which make the process expensive.

Previous researchers reported that the apparent contact angle on the rough surface can be predicted by either Wenzel's or Cassie's theory [58, 115-116]. But it was not conclusively clear about which formula to use and when. In fact, Bico *et al*. [58] proposed that Cassie's formula should be used to predict the apparent contact angle on a given rough hydrophobic surface (see Figure 4.10(a)). The experimental results shown above indicate that such a general conclusion could be misleading. The droplet could have either a composite or a wetted surface, depending on how it is formed [117]. Which state offers a lower energy can be predicted using the theoretical analysis previously discussed. Figure 4.10(b) illustrates the lower energy states for the hydrophobic surfaces with a given roughness geometry. For θ_e values greater than that corresponding to the critical point, the droplet with a composite surface offers a lower energy state, whereas for θ_e values less than the critical value, the droplet with a wetted surface has a lower energy [117].

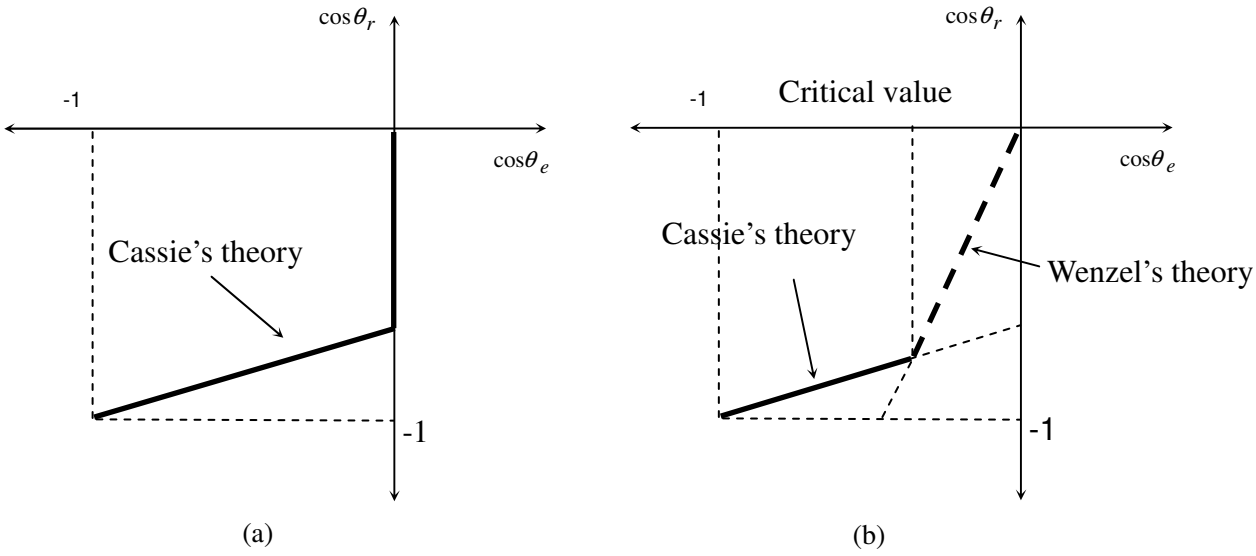

Figure 4.10 Sketch of $\cos\theta_r$ versus $\cos\theta_e$ for the hydrophobic surfaces with a given roughness geometry: (a) model for θ_r recommended by Bico *et al*. based on Cassie's theory and (b) models for θ_r that result in droplets with the lowest energy at a given θ_e

4.4 Contact Angle Hysteresis on Rough Hydrophobic Surfaces

4.4.1 Introduction

The two requirements of superhydrophobic surfaces are very high water contact angles, and very low water roll-off angles. The former topic has been discussed in the last section through the modeling and matching experiments of multiple energy states on rough hydrophobic surfaces. The following section will focus on the contact angle hysteresis of the Cassie and Wenzel drop on a given rough surface.

Current microfabrication technology permits controlled experiments where the roughness of the surface can be quantified in terms of the geometric parameters. Both Cassie and Wenzel

drops can be formed on the same rough surface depending on how a drop is formed [117]. Hence it is of interest to study hysteresis of these drops on the same surface.

In this study, the hysteresis of Cassie and Wenzel drops on a given rough surface is quantified. Experiments are conducted to measure the advancing and receding contact angles on a given rough hydrophobic surface with arrays of square pillars made of PDMS. The experimental measurements are compared with various theoretical models for the contact angles. This shed some light on the microscopic view of the advancing and receding fronts of a drop.

4.4.2 Experiment Details

The rough substrate made of PDMS was fabricated using the soft lithography technique, as detailed in Chapter 3.2. The contact angle measurement was conducted by a goniometer (AST Products Inc, VCA Optima XE, Boston, MA, USA). A droplet with a small volume (2-7 μL) was gently deposited on the substrate to ensure that a Cassie drop is formed. The drop volume was increased in steps using the automatic dispensing syringe. The contact line is an advancing front due to the increase in the drop volume. The advancing contact angle was measured after each volume increment. The drop volume was increased up to about 10 μL. Receding contact angle measurements were then conducted by removing fixed amount water from the droplet in steps. The contact angle was measured after each volume reduction step. The advancing and receding contact angle measurements for the Wenzel drop were carried out in the same way except that a wetted contact was initially formed by dropping the water droplet from some height [118].

4.4.3 Advancing and Receding Contact Angle Measurements

The rough substrate is an ordered array of square pillars. The geometric parameters for the surface used in the experiments were: a = 22.7μm, b = 28.7μm, H = 30μm, where a, b and H are defined in Figure 4.5.

A surface typically has an advancing contact angle corresponding to an advancing front and a receding contact angle corresponding to a receding front. The advancing and receding contact angles of a 'flat' PDMS surface were measured to be 115º and 88º, respectively. Here 'flat' implies that the surface is not roughened by microfabrication. Microscopically (i.e., on length scales much smaller than the 10μm scale of the microfabricated roughness) the PDMS surface may not be perfectly smooth and may have heterogeneities that give rise to its advancing and receding angles.

Figure 4.11 shows the contact angle measurements, of a Cassie drop, for increasing volumes on a rough substrate. When a small drop is deposited on the surface, it typically forms a contact angle between the advancing and receding values of the rough substrate. As the drop volume is increased, the contact angle increases until it reaches the maximum static angle – this is defined as the advancing contact angle of the rough surface. Once the advancing value of the contact angle is reached, further increase in volume does not significantly change the angle of the drop. Microscopically, the increase in the angle with volume could be due to the pinning of the contact line on the substrate. Once the advancing contact angle is reached, the contact line moves (rather than pinning) thus resulting in no significant change in the contact angle of the drop. Thus, Figure 4.11 gives an advancing angle between 152° and 153° for a Cassie drop on the rough substrate [118].

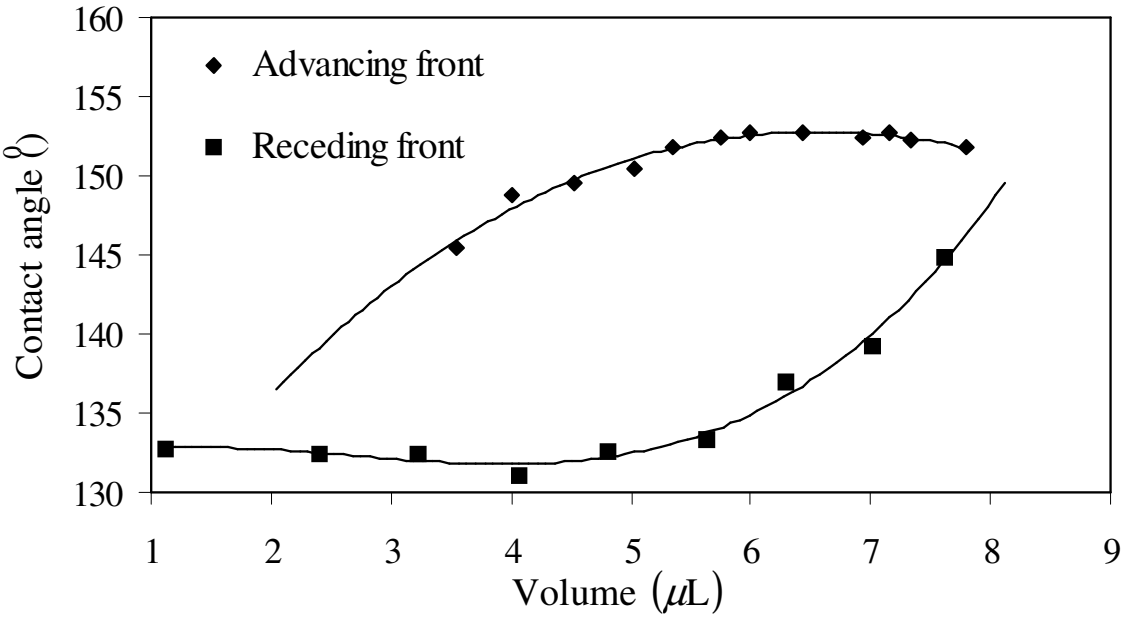

Figure 4.11 Advancing and receding contact angle measurement of a Cassie drop. The plot indicates a hysteresis loop for the contact angle and the drop volume

Figure 4.11 also shows a plot of the receding contact angle measurements for a Cassie drop. The volume reduction was begun from the last drop obtained in the advancing angle measurements. Once again, an initial decrease in the contact angle of the drop with decreasing volume was observed, followed by an almost constant value. The receding contact angle for the Cassie drop was thus found to be about 132°. The difference between the advancing and receding values is a measure of the hysteresis. This is also evident from a hysteresis loop defined by the plots for the advancing and receding angle measurements (Figure 4.11).

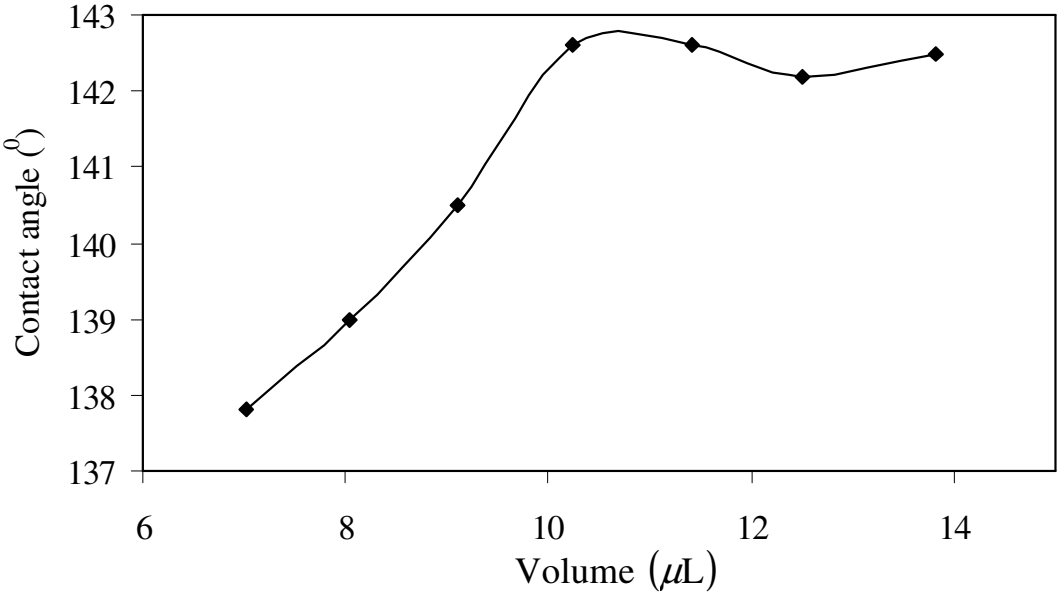

Figure 4.12 Advancing contact angle measurement of a Wenzel drop

Figure 4.12 shows that the advancing contact angle for the Wenzel drop on the same rough surface is between 142° and 143°. No conclusions could be drawn regarding the receding contact angle (Figure 4.13) of a Wenzel drop. The contact angle kept decreasing with decreasing volume up the smallest drop volume that can be imaged. As in Figures 4.13, there is not a constant angle with decrease in the drop volume. The results imply that the Wenzel drop, due to the wetting of the grooves, exhibits very large hysteresis. Therefore, it is undesirable for the applications involving droplet motion. Cassie drops are preferred due to significantly less hysteresis [118].

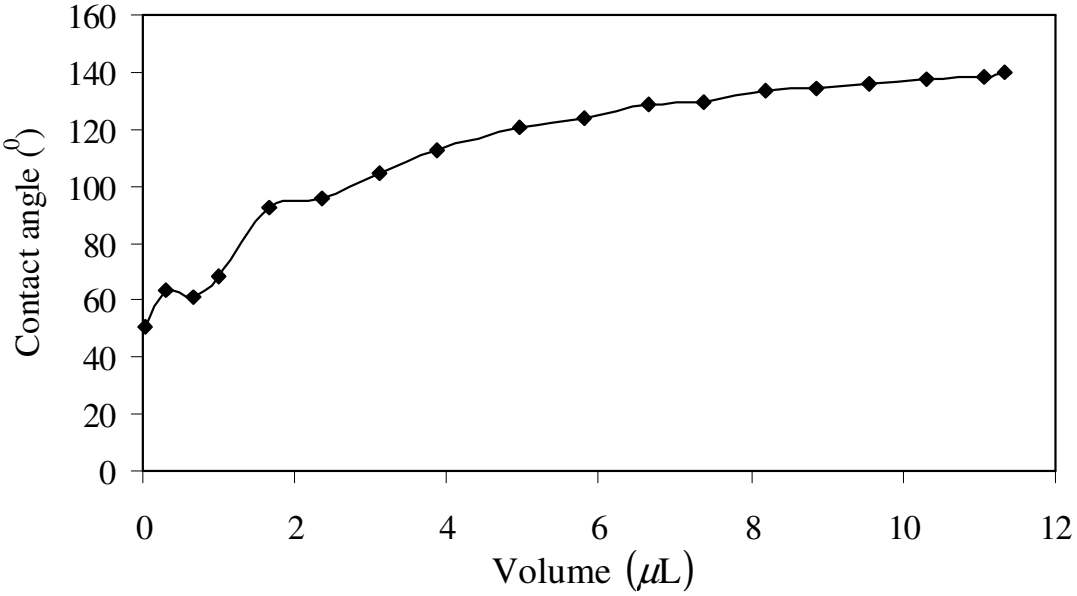

Figure 4.13 Receding contact angle measurement of a Wenzel drop

Next, the models to predict the advancing and receding contact angles of drops on rough surfaces were investigated. The contact angle hysteresis of the roughened surface considered here can be attributed to two aspects – first is the effect of hysteresis at the microscopic scale, i.e., the influence of advancing and receding angles of the PDMS surface itself – and second is the effect of the roughness geometry that gives rise to additional metastable states in which a drop can get trapped thus leading to different advancing and receding angles [119]. The latter was not considered in this work mainly because quantitative models to relate energy barriers to contact angle hysteresis are not well established.

The influence of the first effect can be accounted for by considering the advancing and receding angles of the surface material in the respective Cassie and Wenzel formulas to get the

angles of the artificially roughened surface [118]. The Cassie formula was rewritten in the following form

$$\cos\theta^{c}_{adv} = \varphi_s \cos\theta_{adv} + \varphi_s - 1 \tag{4.13}$$

where φ_s is the area fraction of the peaks of the square pillars on the horizontal surface – $\varphi_s = a^2 / (a+b)^2 = 0.1950$. Subscript *adv* denotes advancing angle and superscripts *c* denotes composite contact. Note that θ_{adv} = 115º for PDMS. Equation (4.13) gives θ^{c}_{adv} = 152.5º, compared to the experimental value between 152º and 153º. Thus, the advancing angle of a Cassie drop is well predicted by the Cassie formula with the advancing angle for the flat surface. This is reasonable since an advancing front is also moving forward microscopically on the surface material. It can be verified that the data from previous experiments [58, 117] are also well represented by equation (4.13).

Modeling of the receding contact angle of the Cassie drop can be done analogous to equation (4.13)

$$\cos\theta^{c}_{rec} = \varphi_s \cos\theta_{rec} + \varphi_s - 1 \tag{4.14}$$

where subscript *rec* denotes receding angle and θ_{rec} = 88º. This gives θ^{c}_{rec} = 143º compared to an experimental value of 132º. Patankar [53] proposed another model to estimate the receding contact angle for Cassie drops. As the contact line recedes, it is assumed that the droplet leaves behind a thin film of liquid on the peaks of the pillars instead of leaving behind a dry surface (as assumed in equation (4.14)). The receding contact angle in this case is given by

$$\cos\theta^{c}_{rec} = 2\varphi_s - 1 \tag{4.15}$$

Equation (4.15) gives θ^{c}_{rec} = 127.6º which is closer to the experimental value. It may be noted that the experiments of Bico *et al.* also agree with equation (4.15) better. It is, therefore, likely that the mechanism implied by equation (4.15) plays some role in the receding contact angle of Cassie drops.

The advancing contact angle of the Wenzel drop can be predicted by Wenzel's formula

$$\cos\theta^{w}_{adv} = r\cos\theta_{adv} \tag{4.16}$$

where superscript *w* denotes a wetted contact and *r* is the solid roughness, defined as the ratio of the actual solid-liquid contact area to the contact area projected on the horizontal plane. Thus, $r = \left((a+b)^2 + 4aH\right) \Big/ (a+b)^2 = 2.0311$ in this case. Equation (4.16) gives θ^{w}_{adv} = 149º, compared to the experimental value of 142º.

Models for the receding contact angle of a Wenzel drop on a rough surface are not evident. Even when a Wenzel drop simply deposited on a rough surface shows hydrophobicity, it is concluded that the hysteresis is significant due to the wetting of the grooves.

Up to this point, the multiple energy states and contact angle hysteresis have been investigated through the contact angle measurements on rough hydrophobic surfaces with arrays of square pillars. The effect of anisotropic roughness to the wetting behavior on rough hydrophobic surfaces will be discussed in the next section.

4.5 Contact Angle Anisotropy on Rough Hydrophobic Surfaces

4.5.1 Introduction

When a drop resides on a rough surface, if the roughness geometry is isotropic then the drop shape is almost spherical and the contact angle of the drop with the rough surface is nearly uniform along the contact line. The apparent contact angle for a 'composite' spherical drop is given by Cassie's formula while that for a 'wetted' spherical drop is given by Wenzel's formula [51-52].

If the roughness geometry is not isotropic, i.e., parallel grooves, then the contact angle is no longer uniform along the contact line. It was reported that the apparent contact angles observed perpendicular and parallel to the direction of the grooves are different [58]. The exact mechanism for anisotropic wetting and the resultant shape of the drop was not discussed [58]. Anisotropic wetting for chemically patterned hydrophilic surfaces has also been observed [120]. Wenzel and Cassie formulas are insufficient to understand this anisotropy in the wetting of rough surfaces. A better understanding of this problem is critical in designing rough superhydrophobic surfaces. In this section, a theoretical and an experimental study of the wetting of surfaces with anisotropic roughness (parallel grooves) are reported. The primary objective of this work is to determine the mechanism of anisotropic wetting and to propose a methodology to quantify the contact angles and the drop shape [121].

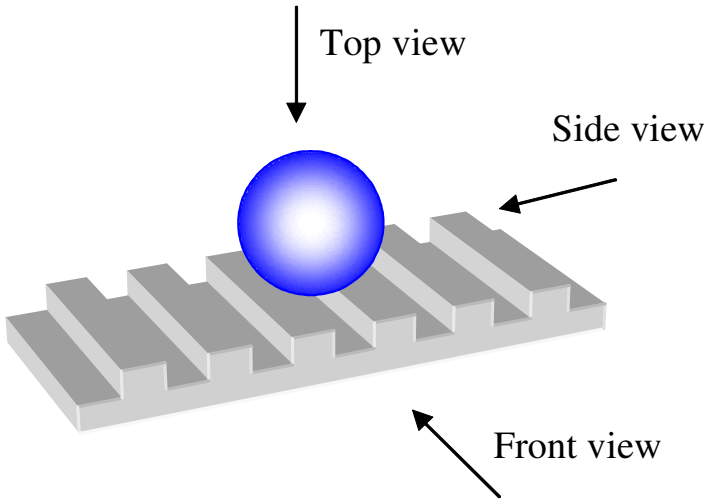

Figure 4.14 Schematic of a drop sitting on a substrate with horizontal grooves. Note the definitions of the different views

4.5.2 Numerical Simulation of the Drop Shape

Numerical simulation results are first presented in order to understand the primary characteristics of the drop shape on anisotropic roughness. Public domain software by Ken Brakke [122] was used to numerically investigate the three-dimensional drop shapes and the apparent contact angles on rough surfaces. Figure 4.14 shows a roughness geometry of horizontal grooves. A similar investigation of drop shapes on chemically heterogeneous surfaces has been reported earlier by Brandon *et al*. [123]. Gravity is neglected, which is a reasonable assumption for small drops.

The numerical procedure is based on minimizing the free energy of the system to obtain the equilibrium drop shape. The free energy G of the system is given by

$$G/\gamma_{LV} = S_{LV} - \iint_{S_{SL}} \cos\theta_e \, dA \tag{4.17}$$

where L denotes the liquid that makes the drop, V denotes the fluid (typically air) surrounding the drop, S denotes the solid surface, S_{LV} and S_{SL} are the liquid–air and the solid–liquid interfacial areas of contact, and γ_{LV} is the liquid–air interfacial tension which is assumed to be constant. The equilibrium contact angle θ_e of the substrate material is defined by Young's equation (4.1). Minimizing the free energy G with respect to the liquid–air interface shape, while constraining the drop volume to a fixed value, gives the equilibrium drop shape. In the solution procedure, G/γ_{LV} is minimized. Hence, for a given problem, the only material parameter that needs to be specified is θ_e.

It can be shown [124], using variational principles, that the constrained minimization procedure is equivalent to solving the Laplace equation for the pressure drop at each point on the liquid-air interface,

$$\frac{2\gamma_{LV}}{R_m} = \Delta p \tag{4.18}$$

along with Young's equation (4.1) on the solid–liquid–air contact line as the boundary condition. R_m is the mean radius of curvature and Δp is the pressure drop at a point on the drop surface. A stationary drop on a substrate, in constant ambient pressure, will have a constant pressure drop at each point on the liquid-air interface (gravity neglected). Hence, it follows directly from equation (4.18) that a stationary drop should have a constant mean curvature surface. In two-dimensions the arc of a circle is the only constant mean curvature curve. In three-dimensions, the spherical surface is one of the many possible constant mean curvature surfaces.

Detailed information about the numerical methodology to solve the constrained minimization problem (equation 4.17) can be found elsewhere [122]. A brief description is given here.

The equilibrium drop shape is obtained iteratively from the initial shape. At each iteration the vertices on the liquid-air interface are moved in order to reduce the energy of the system while adhering to the imposed constraints (i.e., constant volume). Iterations are repeated until the system's energy does not change significantly. Suitable modifications were done to the software to handle a rough substrate.

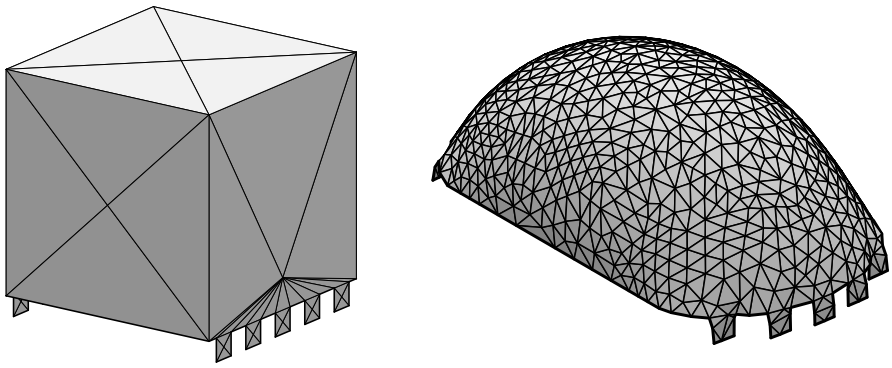

Figure 4.15 Initial and equilibrium configurations of a drop on six pillars. The equilibrium contact angle is 90º

Figure 4.15 shows the initial shape of a drop of a given volume placed on the rough substrate. The grooves underneath the drop are initially filled with liquid. The equilibrium

contact angle of the drop on the solid surface is specified. The Surface Evolver was used to obtain the final equilibrium drop shape from a given initial shape (Figure 4.15).

The objective here is to understand the general qualitative features of the drop shape. A drop of unit volume was considered. The groove was 0.1 unit wide × 0.1 unit deep. The pillar width was also taken as 0.1 unit. Multiple equilibrium shapes can be obtained for the drop depending on the number of pillars on which the drop resides [119]. During a given run, the number of pillars is fixed in order to find the possible equilibrium shape. Note that an equilibrium shape is not possible for any choice of the number of pillars underneath the drop.

Figure 4.15 shows the initial shape (which is arbitrary) and the final equilibrium shape when the drop resides on six pillars. The left and the right edges of the drop are constrained to move on the first and the sixth horizontal pillars, respectively. The equilibrium shape thus obtained is the local minimum of the free energy. The resultant equilibrium shape satisfies the condition that the mean curvature of the surface is constant. The local contact angle along the actual solid-liquid-air contact line is equal to the equilibrium contact angle ($\theta_e = 90^\circ$ in this case).

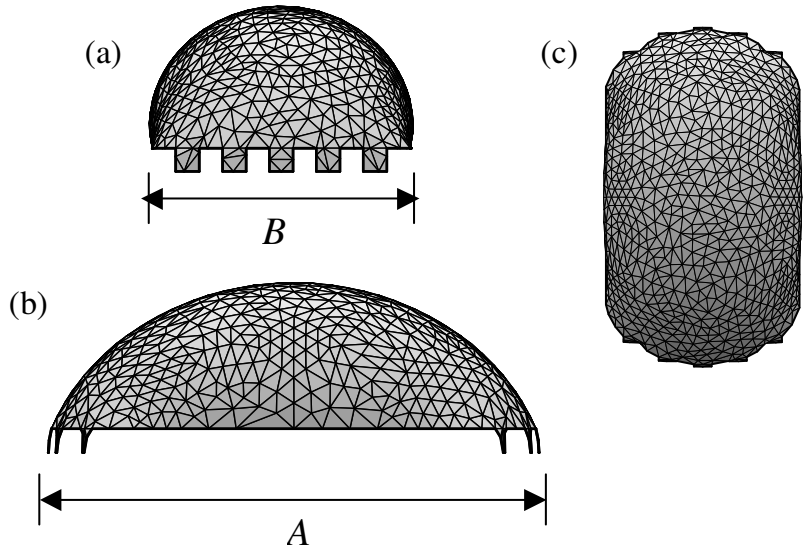

Figure 4.16 (a) Front, (b) side and (c) top views of a drop sitting on six pillars. A and B are the lengths of the base of the drop in the side and front views, respectively

Figure 4.16 shows the various views of the drop in Figure 4.15. It can be seen that the fluid 'pins' on the edge of the horizontal pillars. For an equilibrium contact angle of 90^o, the apparent contact angle on the edge can vary between 90^o and 180^o (see Oliver *et al.* [125]). The apparent contact angles in the front and side are different (Figure 4.16), in qualitative agreement with the previous experiments [58]. Note that the apparent contact angles are not equal to the equilibrium contact angle of 90º.

Figure 4.17 shows the effect of the number of pillars on which the drop resides. All the other parameters, i.e., the drop volume, the liquid-air surface tension and the equilibrium contact angle are the same as the case in Figure 4.15. The shape of the drop becomes longer as the number of pillars is reduced. The apparent contact angle increases in the front view as the

number of pillars is reduced. In each case, the left and the right edges are pinned on the edge of the horizontal pillars. Of the three cases considered here, the free energy of the drop sitting on six pillars (Figure 4.16) is minimum. The drop can acquire any of the configurations above depending on how it is formed. Cases with more pillars were not considered in view of the computational cost.

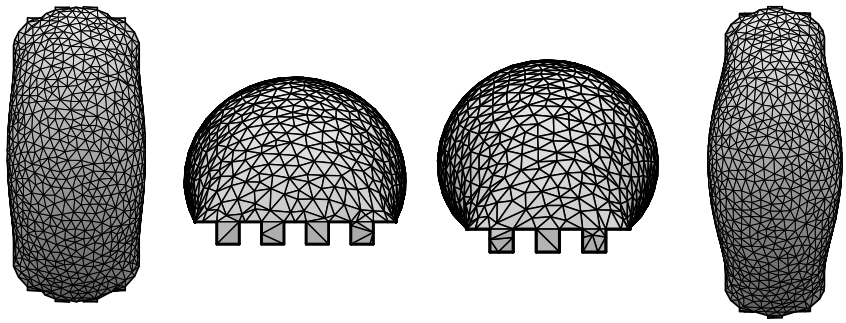

Figure 4.17 Equilibrium drop shapes as a function of the number of pillars on which it settles. Two figures on the left are for five pillars and the two on the right are for four pillars (figures for the two cases are not drawn to the same scale)

In Figures 4.15–4.17, wetted contacts were considered, i.e., the grooves are filled with liquid. The qualitative features presented above remain typically unaltered for hydrophobic cases (i.e. $\theta_e > 90^\circ$) if a wetted contact is formed (Figure 4.18)

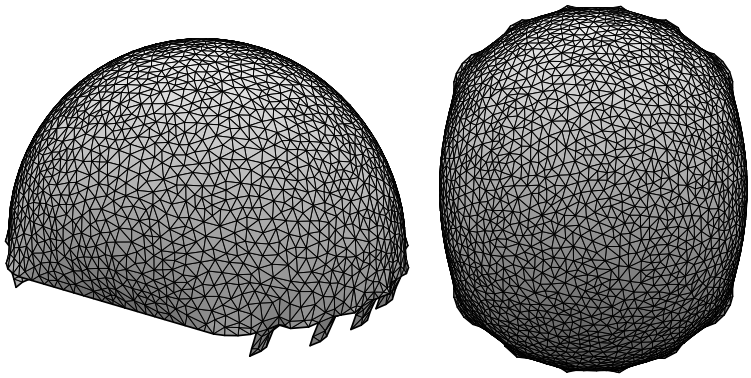

Figure 4.18 Equilibrium drop shape for $\theta_a = 105°$. All other parameters are the same as the case in Figure 4.15

The main interest of this work is in the hydrophobic drops with composite contacts with the substrate [121]. The experimental results for the composite contact case will be shown next. The composite contact case can be set up for numerical simulations as depicted in Figure 4.19.

Figure 4.19 shows a cartoon of the front view of a drop on six pillars with a composite contact with the rough substrate. The assumptions involved are that the liquid–air interface on top of the empty grooves is almost flat. This is reasonable when the drop size is large so that the mean radius of curvature is large compared to the size of the roughness features. The problem is then equivalent to a drop on a heterogeneous (i.e., equilibrium contact angle changes) flat surface. On the horizontal pillars the equilibrium contact angle is the same as that of the substrate material and at the location of the grooves the effective equilibrium contact angle is 180º (Figure 4.19).

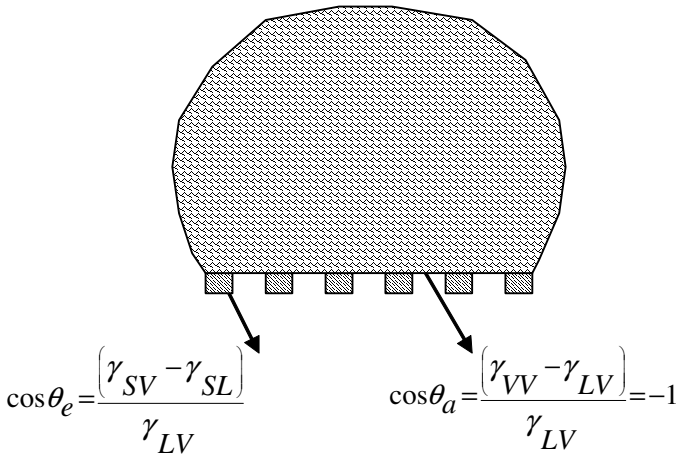

Figure 4.19 A cartoon of the front view of a drop with a composite contact with a rough substrate with horizontal grooves

Surface Evolver was also used to solve the composite drop case. The equilibrium contact angle of the substrate material was taken to be 120º. The pillar and groove widths and the drop volume were the same as the cases depicted in Figure 4.15–4.17. Similar to the wetted drop case, there are multiple equilibrium shapes depending on the number of pillars on which the drop resides. Figure 4.20 shows the drop shape for the case when there are six pillars underneath the drop. Once again, pinning of the liquid at the edge of the pillars was observed. The apparent contact angles in the front and side views are different and greater than 120º.

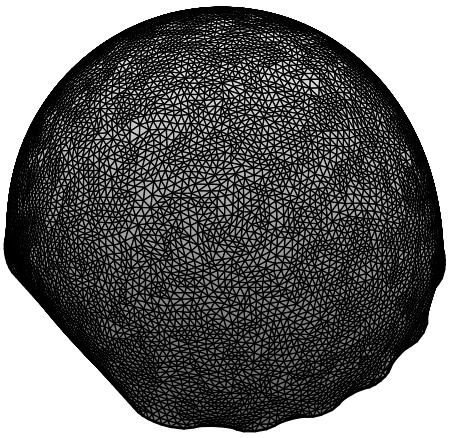

Figure 4.20 The drop shape on a rough substrate for the composite contact case

A few comments are in order. The pinning of the fluid at the edge of the pillars was observed for the cases presented above. There is no guarantee that all the possible cases have been exhausted. Thus, pinning may not exist for all possible equilibrium shapes. However, the Surface Evolver simulations of Brandon *et al.* [123] for chemically patterned surfaces do show similar characteristics.

Based on the above, it can be concluded that there are multiple equilibrium shapes for a drop on a rough surface with parallel grooves. A particular equilibrium shape can be typically obtained by fixing the number of pillars on which the drop resides. For the case of a composite contact of a hydrophobic drop, the apparent contact angles in the front and side views are different and both are usually larger than the equilibrium contact angle of the substrate material. In addition, the apparent angle in the front view is usually larger than the apparent angle in the side view (also see the experimental results in the next section). This is a consequence of the

squeezing and pinning of the drop in the front view and stretching of the drop in the side view. The experimental results will be discussed in the next section.

4.5.3 Experimental Observations

A rough substrate with a parallel groove geometry was fabricated. The fabrication method was discussed in Chapter 3. The substrate material was made of PDMS (θ_e = 114º). The pillar width was 23 μm, the groove width was 25.6 μm and the pillar height (i.e., also the groove depth) was 30 μm. A droplet of specified volume was gently deposited on the substrate by an automatic pipette. This resulted in a composite contact [121]. The contact angles were then measured in the front and side views. The length of the base of the drop in the front and side views were also measured (see definitions in Figure 4.16). The data are given in Table 4.3. Each case was measured after depositing a new drop.

In all cases, the contact angles in the two views are unequal and both are greater than the equilibrium contact angle of PDMS (θ_e = 114º). The angle in the front view is larger than the angle in the side view; correspondingly the base length B in the front view is smaller than the base length A in the side view (Figure 4.21).

Table 4.3 Experimental data for drops of different volumes V on a rough surface of parallel groove geometry. θ_F is the contact angle in the front view, θ_S is the contact angle in the side view and $\Delta\theta = \theta_F - \theta_S$. The number of pillars are estimated based on B and the pillar and groove dimensions

V (mm^3)	θ_F (^{0})	θ_S (^{0})	$\Delta\theta$ (^{0})	A (mm)	B (mm)	Pillars	D_{sp} (mm)
0.59	140.4	125.4	15	0.898	0.698	15	0.736
1.432	143.7	125	18.7	1.215	0.898	19	0.989
2.077	144.1	125.5	18.6	1.376	1.008	21	1.12
4.818	148.1	128	20.1	1.764	1.267	26	1.48
5.151	149.5	126.5	23	1.855	1.247	26	1.52
5.679	150.7	127.2	23.5	1.887	1.267	26	1.566

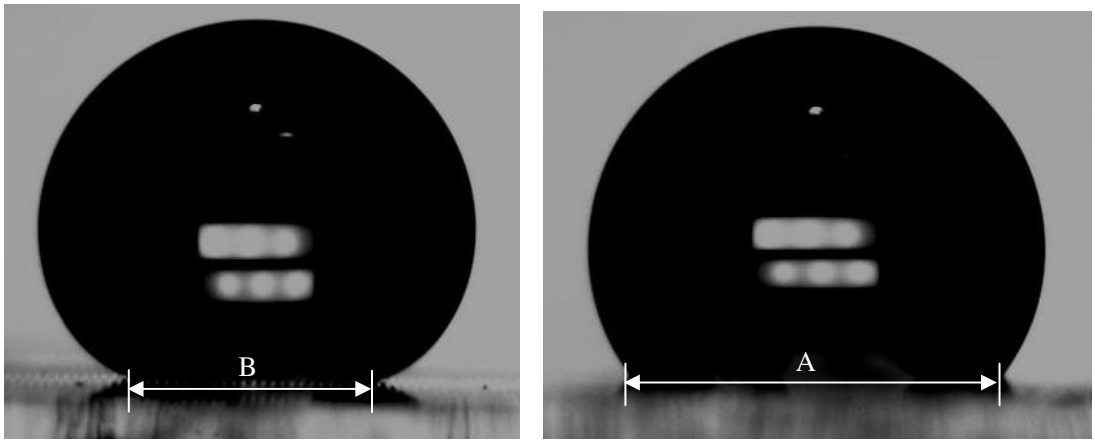

Figure 4.21 Front (left figure) and side (right figure) views of a drop sitting on a rough surface with parallel groove geometry. It is evident from the front view that the drop is sitting on top of the pillars. The drop volume is 5.15 mm^3, θ_F = 149.5º, θ_S = 126.5º and B < A

The apparent contact angle θ_c for a spherical composite drop on this substrate can be calculated by Cassie formula [52-53]. θ_c = 136º for the geometric parameters given above. This value is between θ_F and θ_S. The Cassie formula assumes a spherical drop with a circular contact line so that the contact angle is uniform as seen from all directions. This is not the case here. The average shape of the contact line in this case is not circular since $A \neq B$. Thus, Cassie formula does not fully explain the observed behavior in Table 4.3.

Consider a spherical composite drop on the rough substrate. The diameter D_{sp} of the circular contact line at the base of the spherical drop is given by

$$D_{sp} = 2\left(\frac{3V}{\pi(1-\cos\theta_c)^2(2+\cos\theta_c)}\right)^{1/3}\sin\theta_c \qquad (4.19)$$

where V is the drop volume. Table 4.3 lists the values of D_{sp} for different drop volumes in the experiment. It is noted that D_{sp} is a good estimate (within 7%) of the mean diameter, $D = (A + B)/2$, of the base of the drop [121].

It is seen from Table 4.3, that D_{sp} is always greater than B while it is always less than A. This implies that the experimentally observed drop is such that it resides on fewer pillars compared to a spherical composite drop on the same substrate. Thus the base of the drop is 'squeezed' (Figure 4.21) in the front view compared to a spherical composite drop on the same substrate ($B < D_{sp}$). The 'squeezing' is possible because the drop pins on the edge of the pillars as seen in the front view. Due to squeezing and pinning, the angle θ_F in the front view is larger than θ_c = 136º (which is itself larger than the equilibrium contact angle θ_e = 114º of the substrate material because of the presence of air in the grooves).

Since the drop is 'trapped' on fewer pillars, i.e., squeezed as seen in the front view, it leads to 'stretching' (Figure 4.21) in the side view compared to a spherical composite drop on the same substrate ($A > D_{sp}$). This results in an elongated drop as indicated in the numerical simulation section. Stretching causes the angle θ_S in the side view to be smaller than θ_c. Note that θ_S is still larger than the equilibrium contact angle of the substrate due to the presence of air.

The above two paragraphs qualitatively explain why θ_F and θ_S are greater than the equilibrium contact angle of the substrate material. The fact that $\theta_F > \theta_S$ is because the drop sits on fewer pillars compared to the number of pillars on which a spherical composite drop would sit on the same substrate. It is possible that θ_F would be less than θ_S if the drop somehow got trapped on more number of pillars compared to the number of pillars on which a spherical composite drop would sit on the same substrate.

In numerical simulation section, it was shown that different equilibrium drop shapes are obtained depending on the number of pillars on which a drop resides. It was also observed that the fewer the pillars on which the drop resides, the greater is the apparent angle in the front view. The experimental observations are consistent with the simulation results. The discussion here, although qualitative, highlights the mechanism of anisotropy in wetting.

Next, the quantitative information regarding the apparent contact angles and the drop shape is obtained. One option is to perform simulations for a composite drop on the substrate. The number of pillars on which the drops reside ranges from 15 to 26. It is computationally very expensive to resolve the drop shape in such detail. Therefore, a different approach was considered as discussed below [121].

At the microscopic scale, the actual contact line of a drop on a rough substrate is not smooth. However, the actual contact line can be approximated, i.e., by an equivalent smooth circular contact line in the case of a spherical composite drop. This particular drop shape can be regarded as the one with the lowest energy among all the constant mean curvature surfaces of a spherical shape [126]. This approximation works well for isotropic rough surfaces. For anisotropic rough surfaces, the drop can form a different mean curvature surface that is not spherical. In order to approximate such a shape, an equivalent smooth non-circular contact line along the base of the drop is assumed, instead of resolving the details of the actual contact line. A constant mean curvature surface can be found that has this specified non-circular contact line. The resultant shape will give the contact angles in the front and side views.

It is hypothesized that different shapes for the equivalent contact line matches the values A and B in the two views. An ellipse is one choice but it was found that a cubic equation resulted in better agreement with the experimental data. The equation for the cubic contact line is

$$\left(\frac{2|x|}{A}\right)^3 + \left(\frac{2|y|}{B}\right)^3 = 1 \tag{4.19}$$

where $|\ |$ denotes the positive value of the variable. The experimental values of A and B in the cubic equation above were used for each of the experimental cases. This gives the equivalent contact line of the drop. Surface Evolver was then used to find a constant mean curvature surface that has the specified contact line and the specified (experimental value) volume. The contact angles in the side and front views were then calculated from the simulated drop shapes. Figure 4.22 shows a comparison of the experimental and numerical values of θ_F and θ_S. The agreement is fairly good (within 10-15%) and consistent in terms of the trend. It is noted that a correct trend

is obtained even with an elliptic contact line but the quantitative agreement with the experimental data is not very good. This indicates that the cubic curve for the equivalent contact line is a good approximation of the average shape of the actual contact line of the drop, at least for the parameter considered in this study.

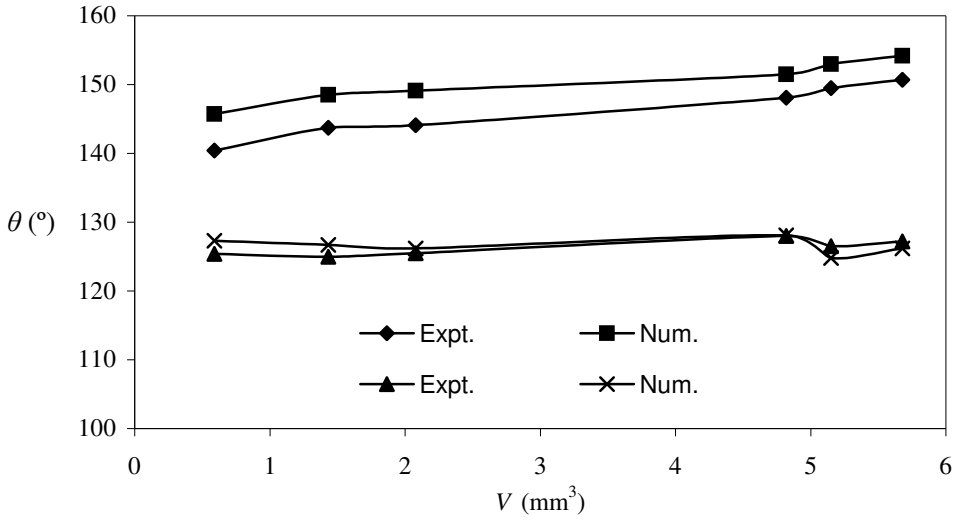

Figure 4.22 Comparison of the experimental and numerical values of θ_F and θ_S

4.5.4 Summary

It is concluded that there are multiple equilibrium shapes for a drop on a rough surface with parallel grooves. A particular equilibrium shape can be typically obtained by fixing the number of pillars on which the drop resides.

A hydrophobic composite drop on the rough surface is studied theoretically and experimentally. The contact angles in the front and side views are different and both are larger than the equilibrium contact angle of the substrate material. The drop is typically trapped in a state where it resides on fewer pillars compared to a spherical composite drop on the rough surface. As a result, the angle in the front view is larger than the angle in the side view. This is a consequence of the squeezing and pinning of the drop in the front view and stretching of the drop in the side view.

It is found that the experimental data is reproduced well numerically if an equivalent smooth non-circular contact line along the base of the drop is assumed. The resultant drop shape is not spherical. The contact angles in the front and side views are in good agreement with the experimental data.

Anisotropic wetting can affect the sliding behavior of drops such as those considered in this work. Yoshimitsu *et al*. [127] showed that drops slide better when the grooves are parallel to the slope. This appears consistent with the conclusions of this work. Pinning of the fluid on the edge of the pillars will cause greater resistance to sliding when the grooves are perpendicular to the slope.

CHAPTER FIVE: A ROUGHNESS BASED WETTABILITY SWITCHABLE MEMBRANE DEVICE FOR HYDROPHOBIC SURFACES

5.1 Introduction

A lab-on-a-chip (LOC) is a device that integrates one or several laboratory functions on a single chip only millimeters to a few square centimeters in size. LOC devices are commonly used in biotechnology, drug discovery and chemistry. They have many advantages over conventional technologies, some of which are low fluid volume consumption, and thus less cost and waste; faster analysis and response time due to shorter diffusion distance; cost-effectiveness due to the smaller amount of reagent required for diagnostics, and low fabrication costs due to mass production; and potential as a safe platform for chemical, radioactive, and biological studies [128].

Recently, much attention has been paid to the development of droplet-based LOC because it can deal with the handling of fluid volume as small as nanoliters. The key component in LOC is on-chip microfluid manipulation, including separation, transport, and mixing.

As discussed before, when the length scale shrinks down to the millimeter range, body force such as mass can be ignored and surface tension is more dominant. Therefore, the ability to control surface tension force promises a powerful actuation mechanism for microfluid handling device. Electrostatic force, thermal gradient and light have been used to control surface tension and many novel devices are reported [47-48, 59]. However, the applications of the above mechanisms are limited because they either consume too much power (thermal gradient and

light) or will affect the particles in the solution (electrostatic force). Therefore, a new type of surface tension actuation mechanism is in demand.

It is known that surface wettability is a function of surface roughness. The latest experimental results confirm that wettability can be tuned by surface geometry [58, 115-116]. Figure 5.1 shows an example of the wettability shift due to microfabricated surface roughness. The geometry of the square pillars is 2 μm × 2 μm in size, 4 μm in spacing, and 1 μm in height. A thin layer of gold (1000Å) was e-beam evaporated on the surface, followed by vapor phase coating of a self-assembled-monolayer (SAM), 1-hexadecanethiol (HDT). A 46° contact angle difference was observed for a droplet sitting on the flat versus the roughened surface [109]. When a drop is sitting on the boundary of different wettability regions, a net force is generated that can drive the droplet to move [110]. Figure 5.2 shows proof of this concept [109], where a micro-droplet (volume ~7μL) was moved across the boundary from the roughened (superhydrophobic) to the flat (medium hydrophobic) surface.

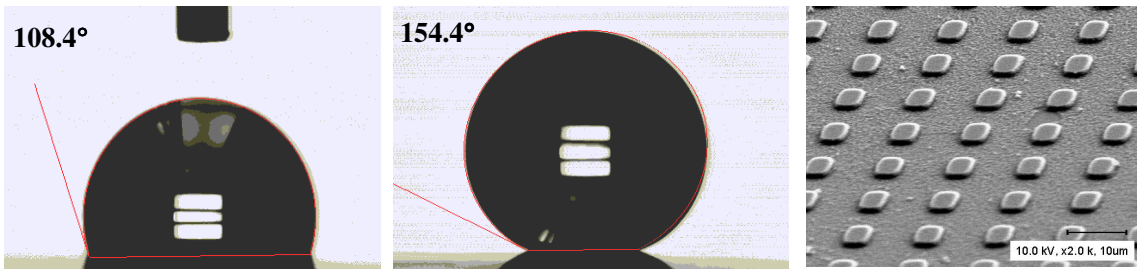

(a) Flat surface (b) Roughened surface

Figure 5.1 Wettability (contact angle) shift due to microfabricated surface roughness

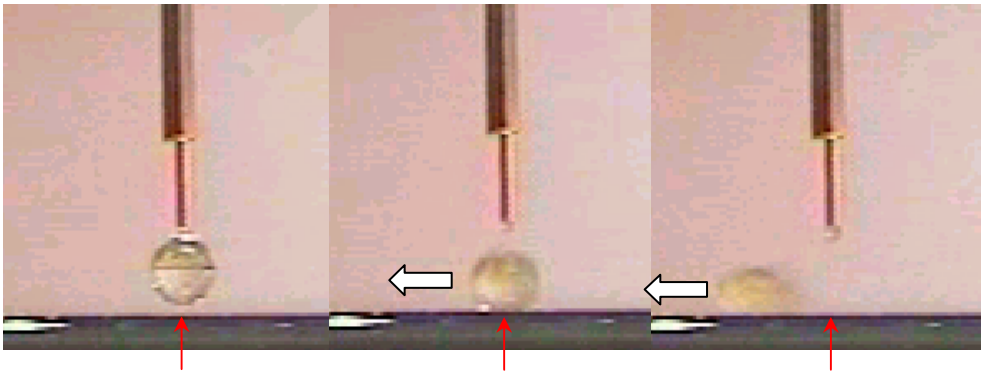

Figure 5.2 Droplet motion across different wettability areas

This chapter describes the development process of a surface tension actuation mechanism that uses purely mechanical means to control surface wettability. The mechanism can potentially be used to achieve continuous droplet motion. The proposed method has an advantage over the other existing methods in many applications, such as biological ones, since there are no thermal or electrical effects on the content of the solution.

Figure 5.3 shows the schematic of the device [109]. A micro droplet is squeezed between a top glass coated with a hydrophobic film and a bottom microfabricated rough substrate with a suspended hydrophobic membrane on top. When the membrane is deflected, the left side of the droplet is in contact with roughened surface which is superhydrophobic and the right side is on the flat surface which is medium hydrophobic. The contact angle difference at two sides of the

drop leads to an internal pressure gradient which can move the droplet to the right direction in this configuration.

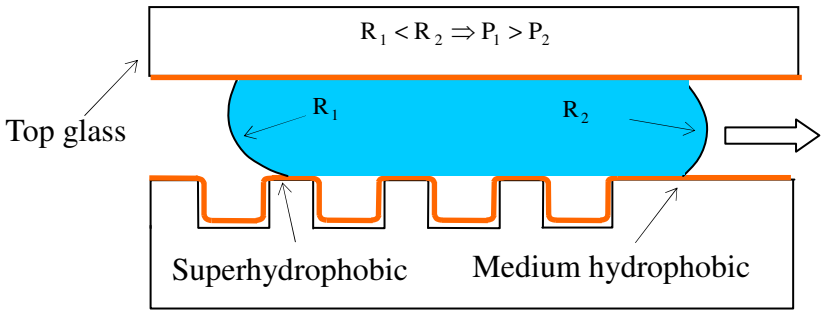

Figure 5.3 Schematic of the cross section view of the transport mechanism

5.2 Fabrication Process of a Wettability Switchable Membrane Device

The fabrication process of a roughness switchable membrane device will be discussed in this section. Based on the analysis presented in Chapter 4, the rough substrate was designed in such that the apparent contact angles given by Wenzel's and Cassie's formula are the same (intersection point in Figure 4.6), therefore the contact angle will not change when external disturbances occur. The geometric parameters of square pillars were a = 26 μm, b = 24 μm, and H = 25 μm. The equilibrium contact angle, θ_e, on the flat PDMS surface was measured to be 114˚. The calculated Cassie's and Wenzel's contact angles using equation (4.3) and (4.4) were

147.1° and 146.1°, respectively. Thus, the geometry is such that it is close to the critical point [109, 117].

The wettability switchable membrane device consists of a thin PDMS membrane (less than 2 μm) suspended on top of a PDMS rough substrate with the pillar geometry given above. Major fabrication steps for the thin membrane device are illustrated in Figure 5.4. The rough substrates with square pillars were fabricated through steps (a)-(c) (Details can be found in Chapter 3). The suspended PDMS membrane was prepared through steps (d)-(f). First, another PDMS prepolymer was prepared and then diluted with hexane with a 1:5 (PDMS to hexane) weight ratio. The mixture was kept for several hours to remove air bubbles. Then the diluted solution was spin-coated on a silicon wafer on which a thin photoresist (PR) layer was pre-coated (d). The thickness of the thin PDMS membrane is mainly controlled by the dilution ratio, speed and time of spin coating. The pre-coated PR works as a lubrication layer to prevent the spin-on thin PDMS membrane sticking onto the silicon substrate. Next, the PDMS rough substrate and thin PDMS membrane coated silicon wafer were treated by oxygen plasma for one minute, and brought into contact to form an irreversible bond (e) [129]. No external force is needed to perform the bonding. Finally, the PDMS substrate can be easily peeled off from the PR coated silicon wafer. The resulting device is a thin PDMS membrane bonded on top of a PDMS rough substrate (f). Figure 5.4(g) shows the schematic of the deflected membrane, which is actuated by suction through an air path at the corner of the patterned area, as shown in Figure 5.5.

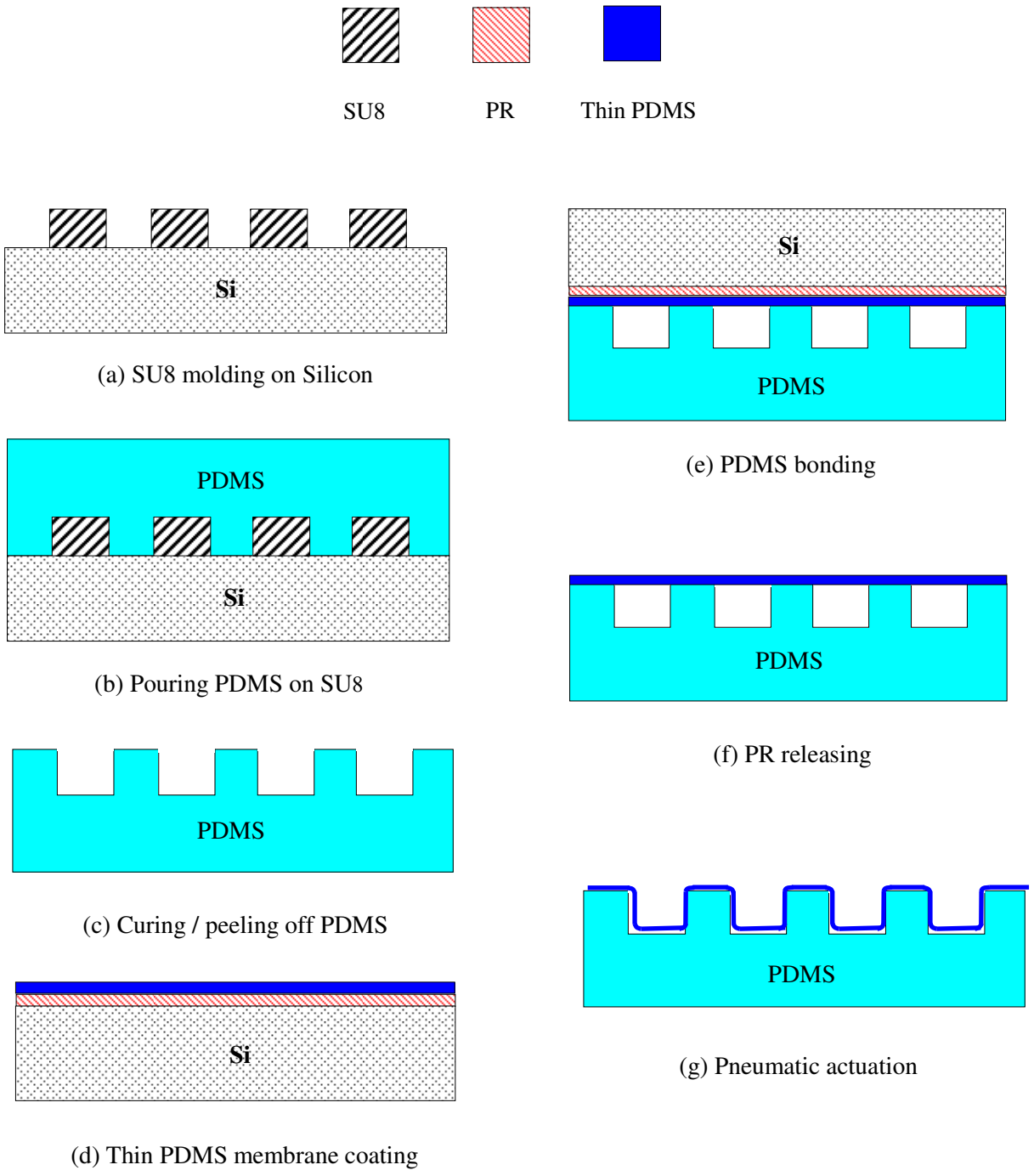

Figure 5.4 Major fabrication processes of the thin membrane device

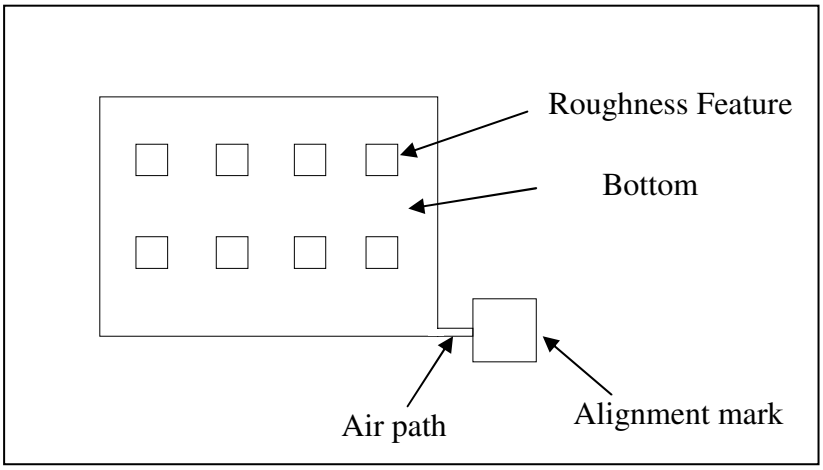

(a) Device top view (w/o membrane)

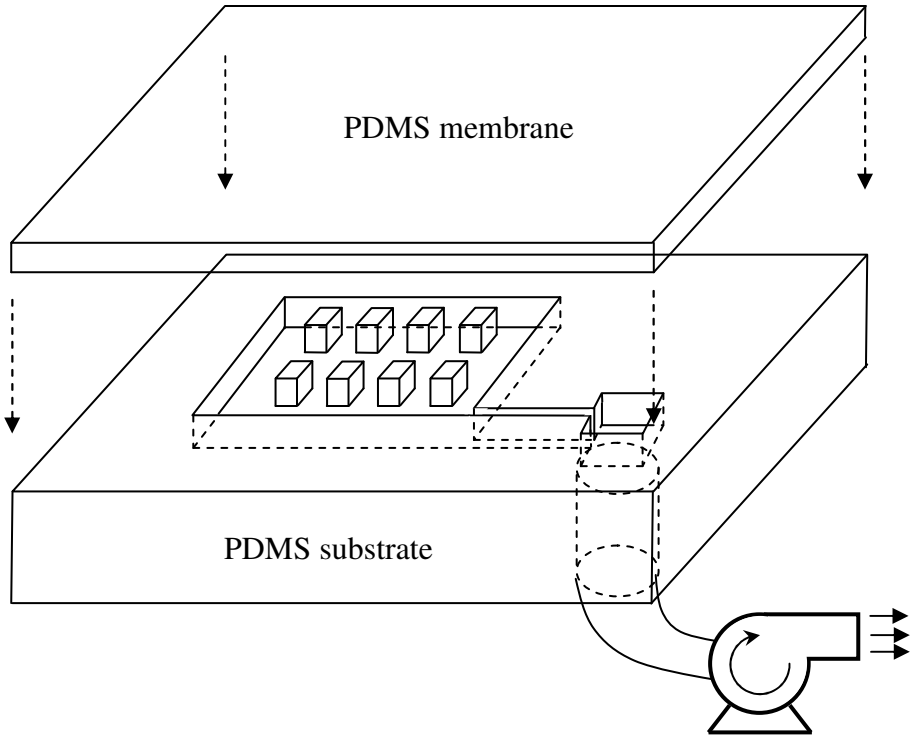

(b) Device side view (with membrane)

Figure 5.5 Top and side views of the device assembly

The experimental setup for the actuation test is as follows: a through hole was made using a small cylindrical pin in the square box next to the air path, which serves as the alignment mark. It was covered on top with a small piece of PDMS stamp and sealed with super glue. The membrane device was then placed on top of a slide glass with the through hole aligned with a small opening prepared in the glass substrate. Super glue was used to seal the device to avoid air leaking between the device and glass substrate. On the other side of the slide glass, a tube connected the small opening to an external pump. One thing noteworthy is that the width of the air path was designed to be thinner than the spacing of the pillar structures on the rough substrate. Otherwise, the pressure difference created by air suction can first fully deflect the membrane on top of the air path, resulting in the close of the air path and no more air can be pumped out after that.

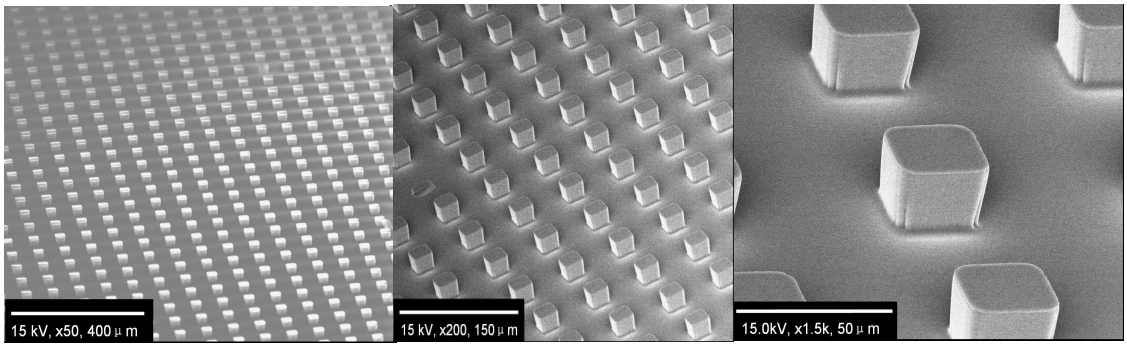

Figure 5.6 SEM images of the rough substrate with pillar structures made of PDMS

5.3 Testing Results of the Membrane Device

The PDMS rough substrate was sputter-coated with a thin layer of gold (30 Å) and imaged by scanning electron microscopy (SEM, Hitachi S-4500), as shown in Figure 5.6. A well-ordered array of pillars can be clearly observed.

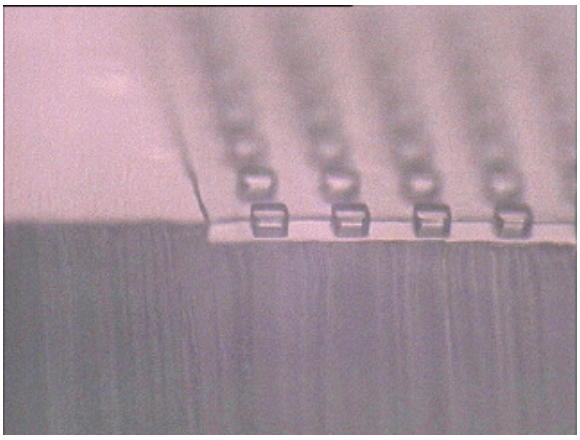

A suspended PDMS membrane (optical microscopy)

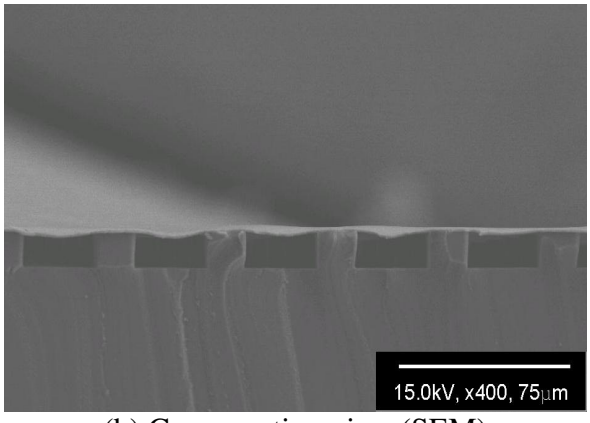

(b) Cross-section view (SEM)

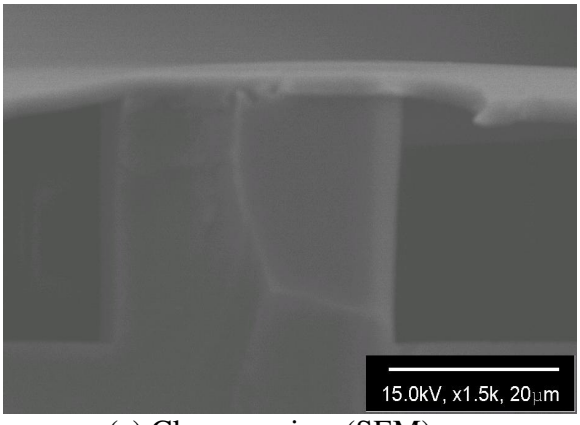

(c) Close-up view (SEM)

Figure 5.7 Images of the suspended thin (~1.25µm) PDMS membrane

Table 5.1 Thickness variation of PDMS membrane according to the dilution ratio

Dilution ratio (Hexane to PDMS)	Thickness (μm)
5:1	1.25
10:1	0.8
15:1	0.5

The fabrication of a thin suspended membrane is the most critical step in the entire process since a thinner membrane can offer less structure dimension variation after being deflected. Also, a thin membrane is easier to deflect. Figure 5.7 shows the suspended thin PDMS membrane imaged by optical microscopy and SEM. The membrane thickness was measured at several locations. The mean value was about 1.25 μm, which was achieved by diluting the PDMS mixture with hexane with a weight ratio 5:1 (hexane to PDMS) and then spin-coating on the silicon wafer at 6000rpm for 3 minutes. To our knowledge, this is the first demonstration of a thin PDMS membrane with a thickness less than 2 μm. It was also verified that even thinner, i.e., sub-micron, membrane is possible with adjusted processing parameters such as the dilution ratio and spinning time. Table 5.1 lists the average thickness of the thin PDMS membrane according to the dilution ratio. The maximum difference between individual thickness measurements, for a given dilution ratio, is 0.5 μm. It should be noted that the fabricated membranes (less than 2 μm thick) are nearly one order of magnitude thinner than those reported in the literature [130]. Therefore, it is expected that this technology will have large impacts in other applications where a thin PDMS membrane based device is required.

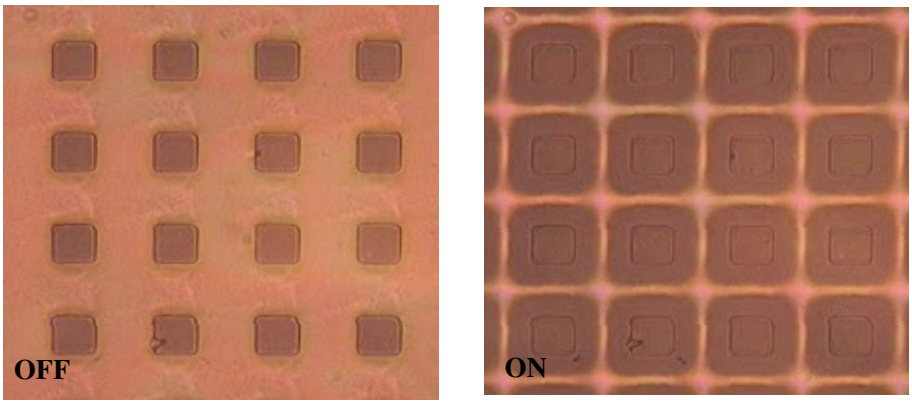

Figure 5.8 Actuation of the membrane device with pillar structures (optical microscopy)

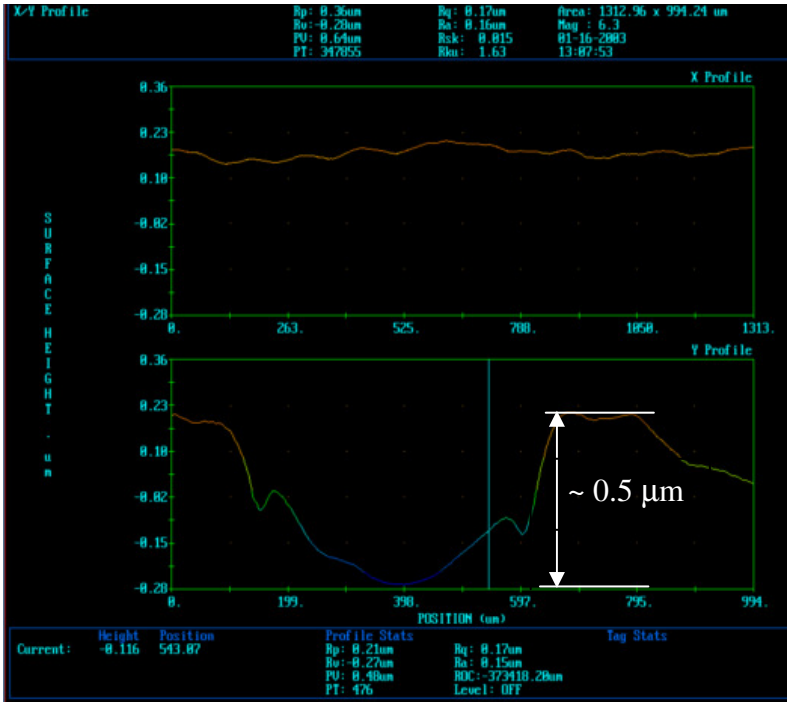

Figure 5.9 Surface flatness measurements after thin PDMS membrane bonding

Figure 5.8 shows the membrane device under testing. “ON” and “OFF” denote actuation and release of the membrane, respectively. A color difference can be clearly observed when the membrane was actuated (deflected) by an applied suction. Then contact angle measurements were conducted using a goniometer (AST Products Inc., VCA Optima XE, Boston, MA, USA) that takes and analyzes the image of a stationary droplet on a surface. The contact angles listed in this work were typically obtained by averaging over several (up to 10) measurements. The variation between individual measurements is up to 5^{o}. Figure 5.9 shows the surface flatness after thin PDMS membrane bonding and before actuation. The observed maximum height variation was less than 0.5 μm, which indicates that the assumption that the suspended membrane after bonding is flat is valid. As a result of the membrane deflection, the contact angle change was observed as shown in Figure 5.10. First, the contact angles on the rough and flat PDMS surfaces (without membrane) were measured as reference values, shown in Figure 5.10(a). Then the contact angles on the membrane device were measured with and without actuation as shown in Figure 5.10(b). The following steps were used for measurement. The membrane was actuated first and then a droplet was gently deposited on it. Both measurement results, (a) and (b), were compared with each other and to the theoretical predictions. The contact angles on the flat and rough PDMS substrates (without membrane) were 113.2^{o} and 144.5^{o}, respectively. The contact angles on the PDMS membrane device without and with actuation were 114.6^{o} and 144.7^{o}, respectively. The contact angle values were obtained by averaging about 10 measurements. The calculated Cassie’s and Wenzel’s contact angles using equation (4.3) and (4.4) were 147.1^{o} and 146.1^{o}, respectively. Based on the discussion in Chapter 4, it is evident that a Cassie drop is formed when water is gently deposited. It was also confirmed

that the droplet can move across the boundary of the patterned area when it was gently deposited after actuating the membrane. The reported mechanism is the first demonstration of a wettability switchable mechanism using surface roughness modification [109].

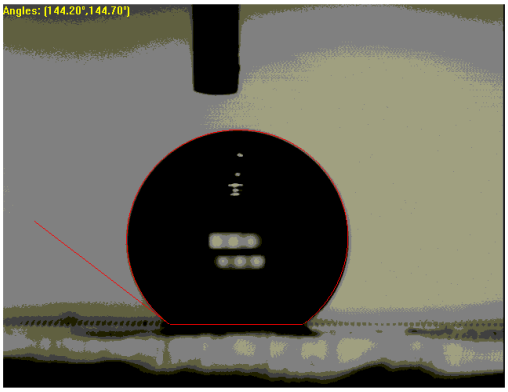

Rough surface: 144.5°

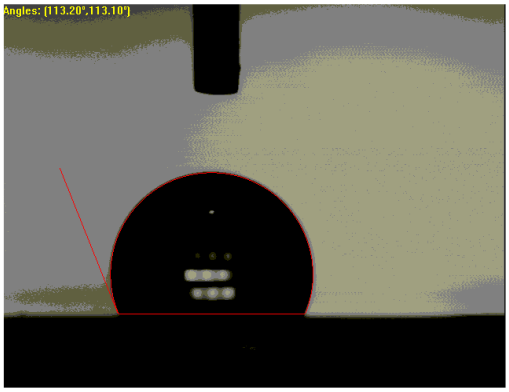

Flat surface: 113.2°

(a) Contact angle measurement on the rough and flat PDMS surfaces

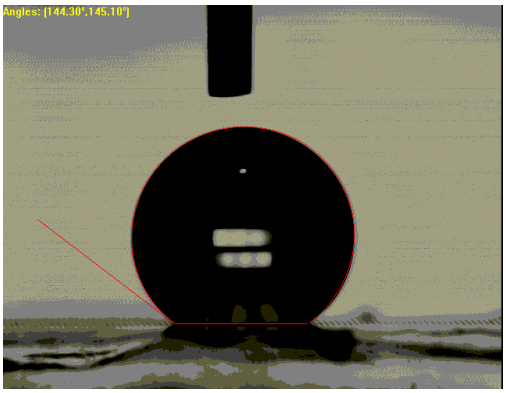

Actuated: 144.7°

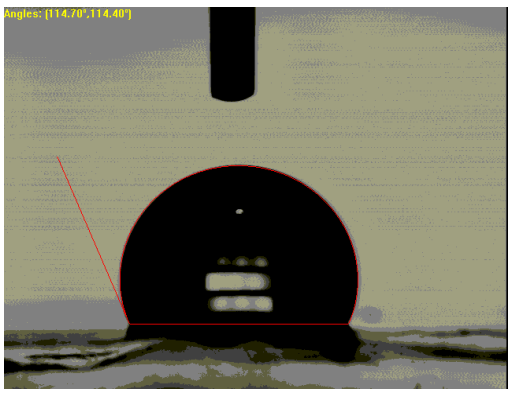

Without actuation: 114.6°

(b) Contact angle measurement of the membrane device with and without actuation

Figure 5.10 Contact angle measurement results before and after membrane actuation

However, if the operation sequence is reversed, that is, depositing the droplet on the membrane device and then actuating half of the area under the droplet, the droplet did not move, which may be due to the formation of a wetted contact [109]. This is explained in more detail in the following section.

5.4 Theoretical Analysis

5.4.1 Formation of A Wetted Contact

When a drop is deposited on a flat surface and then the membrane is actuated, it should be noted that the water is already in contact with the surface material. Hence, it can naturally fill up the grooves and form a wetted contact when the membrane is actuated. To confirm that this occurs, a drop was deposited on a flat surface (the observed contact angle was 114^{o}) and then the membrane was actuated everywhere below the drop. The contact angle hardly changed. In a different measurement, a drop was also deposited on an already actuated membrane but from some height (not gently). The observed contact angle was close to 115^{o}. In both the cases, a wetted contact and therefore a Wenzel drop was expected. Hence, the observed contact angle was expected to be 146.1^{o} (equation 4.10), not 115^{o}.

The reason for the above observation is that the membrane deflection was such that the underlying roughness geometry was not reproduced. The grooves of the deflected membrane were not very deep compared to the underlying roughness geometry. The surface profile after actuation was imaged by an optical profilometer (ADE Phase Shift Inc., MicroXAM, Tucson, AZ, USA) as shown in Figure 5.11. About 4 μm deflection was observed, which is much less

than the full deflection height 25 μm of the underlying roughness. To achieve full deflection, considerable suction is required that significantly stretches the membrane and tears it. Within the current fabrication capabilities, the ability to achieve such large deflections remains a challenge.

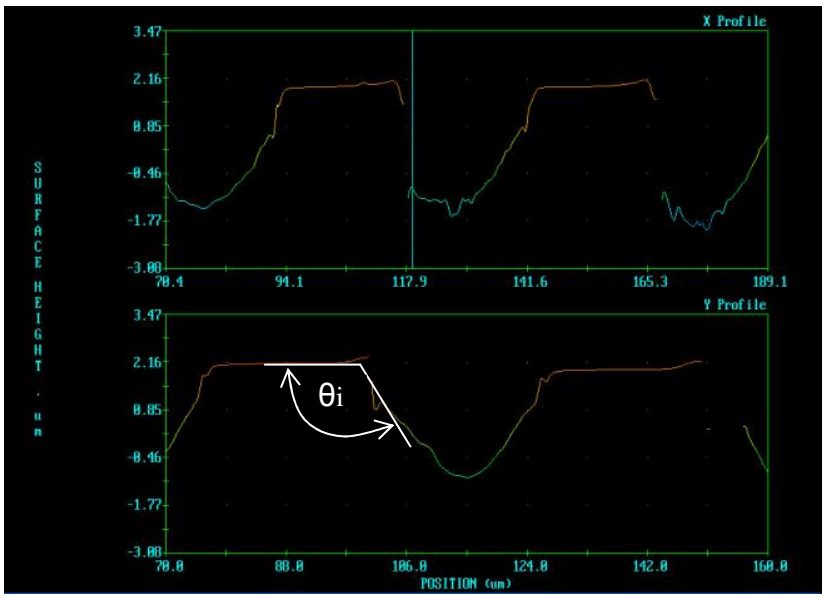

Figure 5.11 Surface profile in X and Y directions of the membrane device (with pillar structures) after actuation, imaged by an optical profilometer. The maximum deflection is ~ 4 μm

Since the deflected membrane had only 4 μm deep grooves, the calculated Wenzel's contact angle for this geometry was 118.3^{o}. This is only slightly larger than the equilibrium contact angle on the flat surface ($\theta_e = 114^{o}$). This is consistent with our observations above that

the contact angle for the Wenzel drop is close to the equilibrium value of the flat surface. Note that the difference in the angles (118.3^o and 114^o) is within the margin of the experimental error.

The formation of shallow grooves, however, does not affect the Cassie contact angle since it depends only on the spacing between the pillars (see Figure 4.6). This is once again consistent with our observation that a contact angle of 144.7^o was measured (compared to the Cassie value of 147.1^o) when the drop was deposited gently after the membrane is actuated. The transition of the gently deposited Cassie drop to a Wenzel state is hindered by an energy barrier [113].

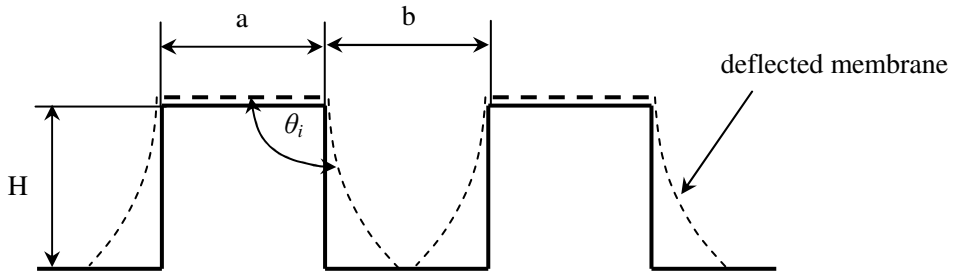

Figure 5.12 The cross section view of the pillar structures and the membrane profile after deflection

The shape of the deflected membrane is another important factor that determines the readiness to form a wetted contact. Patankar [113] argued that a rough surface made of

horizontal grooves with an inclined sidewall can form a composite contact only if $\theta_i \le \theta_e \le 180^o$, where θ_i is the inclination angle of the roughness feature as shown in Figure 5.12. A wetted contact is readily formed when this condition is not satisfied. This condition cannot be directly applied to the pillar geometry in this problem; however, it will still be considered here to estimate the readiness of the liquid to wet the grooves. It was found in Figure 5.11 that the inclination angle in the Y direction is larger than that in the X direction. The inclination angle in Y direction was measured to be $\theta_a = 135^o$, which is larger than the equilibrium contact angle on the flat surface θ_e ($\theta_e = 114^o$). Thus, the condition for the composite contact formation is not satisfied and consequently implies the tendency to wet the grooves. It should, however, be noted that the composite contact condition is satisfied according to the profile in the X direction. The net effect is for the liquid to readily wet the grooves as indicated by the experiments of actuation after deposition.

Consider now the situation where a drop was deposited and then the membrane under half of the drop was actuated. No motion was observed. This can now be explained by the formation of the wetted contact in the actuated region. A larger contact angle on the rough surface, compared to that on the flat surface (θ_e), is necessary to guarantee that sufficient driving force can be generated on the liquid droplet to cause its motion. Since the wetted contact leads to a contact angle close to that on the flat surface, as discussed above, the driving force is not enough to cause droplet motion.

5.4.2 Hysteresis

Another effect that the wetted contact leads to is larger contact angle hysteresis. It is now known that contact angle hysteresis becomes much more when a wetted contact is formed. Figure 5.13 shows the schematic of the mechanism of roughness-induced droplet motion. It should be noted that the receding angle on the rough surface has to be larger than the advancing angle on the flat surface in order to generate sufficient driving force (pressure) to cause droplet motion. Table 5.2 lists the measurement results for the advancing and receding contact angles on the flat, composite and wetted surfaces [118]. It is clearly seen that, when a wetted contact is formed, the receding angle on the rough surface is not larger than the advancing angle on the flat surface, thus the droplet cannot move. However, when a composite contact is formed, the receding angle on the rough surface is greater by 17° than the advancing angle on the flat surface. This contact angle difference can generate enough driving force that causes the droplet motion. This confirms the observation that a droplet can move across the boundary of the patterned area when it was gently deposited after actuating the membrane.

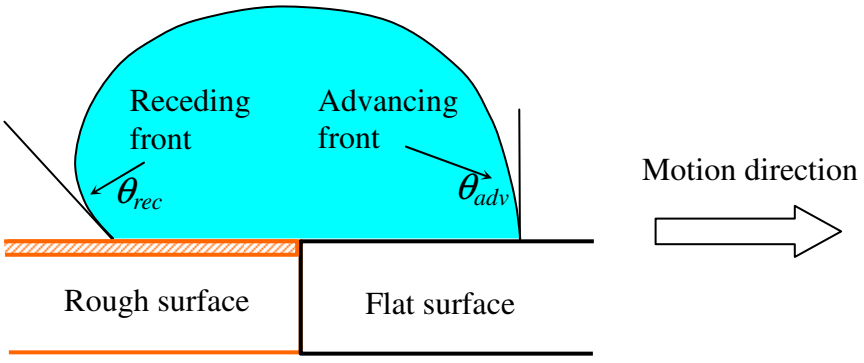

Figure 5.13 Schematic of the cross section view of the mechanism of roughness induced droplet motion

Table 5.2 Advancing and receding contact angles on the flat, composite and wetted surfaces

	Advancing angle (°)	Receding angle (°)
Flat	115	88
Composite contact	152	132
Wetted contact	142	< 60

From the above analysis, it can be concluded that a composite contact is needed for roughness induced droplet motion. To ensure its formation, the rough surface, after actuation, should ideally be such that the wetted contact is physically unrealizable, i.e., $\cos\theta_r^w < -1$. This is possible for rough surfaces with high aspect ratios (i.e., deep grooves) or double roughness structures [54]. It is challenging to actuate large aspect ratio geometry. However, the concept of double roughness could be realistic. The key idea here is to mimic the microstructure of superhydrophobic leaves (such as lotus) as shown in Figure 5.14 [54]. The leaf contains double structured surface roughness – a fine scale (200 nm – 1 μm) and a coarse scale (~ 20 μm). It is experimentally observed (Figure 5.14(b)) that the liquid droplet forms a composite contact on this double roughness structure. A way to design such a surface was discussed by Patankar [108]. A membrane device using such a double structured roughness may be envisaged on which a composite contact is formed even if the membrane is not fully deflected. In this case, the membrane itself should have a smaller scale roughness. Based on this principle, a lab-on-a-chip

device could be developed for biomolecular mixing and amplification. The membrane fabrication and actuation techniques presented in this work can be directly applied to the development of a double roughness based membrane device. However, the development of such a device is not within the scope of this work and is relegated to future studies.

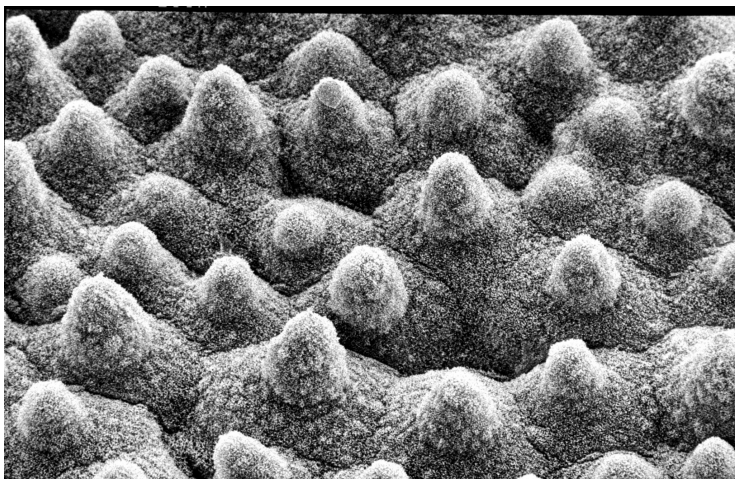

(a)

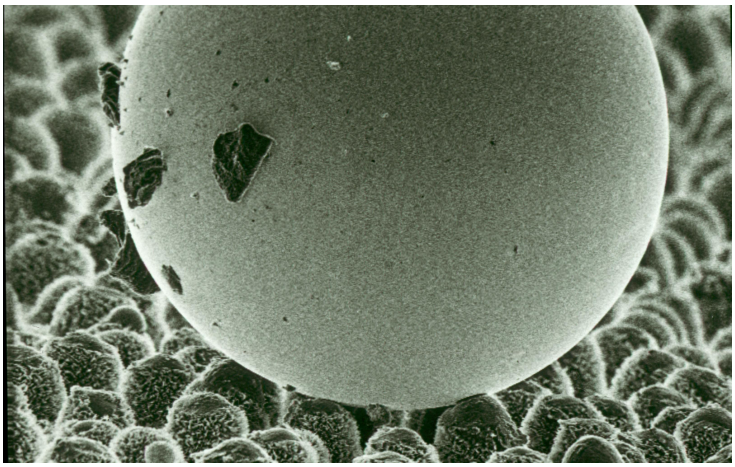

(b)

Figure 5.14 (a) Microscopic image of the surface of Lotus depicting the "double" rough structure, (b) A composite mercury drop on top of the leaf. Figures courtesy Prof. W. Barthlott

5.5 Summary

In this chapter, a technique to fabricate thin PDMS membranes was reported. A novel wettability switchable mechanism using surface roughness effect was designed and fabricated. In this device, a thin PDMS membrane was bonded on top of a rough PDMS substrate. The membrane device was tested and it was found that the surface wettability can be switched from medium hydrophobic to superhydrophobic by deflecting the membrane with pneumatic means. Theoretical analysis was used to explain experimental results.

CHAPTER SIX: CONCLUSIONS

The goal of this study is two-fold: first, to investigate the effect of nano/microscale melting on friction in a silver-bismuth alloy system, and the microscale surface texture effect on friction for PDMS surface; and second, to develop a better understanding of the surface wetting behavior on rough hydrophobic surfaces, and to design and fabricate micro-electro-mechanical systems (MEMS) device for microfluidic applications using the surface roughness effect.

In Chapter Two, the effect of melting on the silver-bismuth alloy nano/microscale friction is investigated by means of high temperature nanoindentation and scratching. Ramping temperature tests for transient friction behaviors and constant temperature tests for friction-temperature correlation have been conducted. High-temperature nanoindentation hardness of these alloys is also measured. The constant temperature results indicate that friction slightly increases as temperature approaches the melting point. The transient results reveal different friction transition phenomena for the alloys with different bismuth concentrations when temperature climbs above the melting points. The molten material does not always reduce the nano/microscale friction of the silver-bismuth alloys, and the friction characteristic depends on the alloy composition. The existence of a critical bismuth concentration is identified, above which the molten material can help reduce the nano/microscale friction at the scratching interface formed with the silver-bismuth alloy.

In Chapter Three, surface texture effect on friction of a PDMS elastomer surface is investigated at the macro- and microscales using a nanoindentation-scratching system. It is found that surface texturing can significantly reduce the COF at the macroscale, while it has less effect

on friction at the microscale. The reduction of COF is attributed to reduced contact area. JKR theory is used to explain the experimental results. Friction anisotropy is observed on groove textured surfaces which may be due to the stick-slip effect. A numerical model is developed to help understand the friction behavior and the simulation results agree with the experimental findings.

In Chapter Four, it is experimentally verified that there can be two contact angles, corresponding to Wenzel's and Cassie's theories, on the same rough surface. One has lower energy than the other. The one that offers the global minimum energy depends on the geometric parameters of the surface. The theoretical predictions are compared to systematic matching experiments. The design criterion for a robust superhydrophobic surface proposed by Patankar is experimentally confirmed. The contact angle of a surface designed according to this criterion will not change as a result of external disturbances.

The hysteresis effect is also studied by measuring the advancing and receding contact angles of Cassie and Wenzel drops on a given rough surface. The Cassie drop shows much less hysteresis compared to a Wenzel drop. The uniqueness of this work is a quantitative study of the hysteresis of Cassie and Wenzel drops on a given rough surface. The advancing and receding angles are defined based on the 'plateau' values as shown in Figures 4.11 and 4.12. In case of the Cassie drop, a hysteresis loop is observed in the plot of the contact angle versus the droplet volume. For the Wenzel drop, such a loop is not observed primarily because no receding contact angle could be defined for this case.

The anisotropy wetting mechanism is investigated by measuring the contact angles in two orthogonal directions on a surface with roughness geometry of parallel grooves. The contact angles observed perpendicular and parallel to the direction of the grooves are different. Based on

the theoretical and experimental studies, methodologies are proposed to quantify the contact angles and drop shapes on the surface with anisotropic roughness.

In Chapter Five, the development of a wettability switchable membrane device using the surface roughness effect is presented. A roughness switchable membrane device, consisting of a thin PDMS membrane bonded on the top of a rough PDMS substrate, is designed and fabricated. A thin (less than 2μm) PDMS membrane fabrication technique is developed. The membrane device is tested and it is found that the surface wettability can be switched from medium hydrophobic to superhydrophobic by deflecting the membrane with a pneumatic method. The reported mechanism is the first demonstration of a wettability switchable mechanism using surface roughness modification. Theoretical analysis is used to explain experimental results and future directions are recommended.

References

1. Oliver, W. C., and Pharr, G. M., "An improved technique for determining hardness and elastic modulus using load and displacement sensing indentation experiments," Journal of Materials Research 17 (6), 1564-1583 (1992)

2. Bellemare, S. C., Dao, M. and Suresh, S., "Effects of mechanical properties and surface friction on elasto-plastic sliding contact," Mechanics of Materials 40 (4-5): 206-219 (2008)

3. Matthews, D. T. A., Ocelik, V., and de Hosson, J. Th. M., "Tribological and mechanical properties of high power laser surface-treated metallic glasses," Materials Science and Engineering A-Structural Materials Properties Microstructure and Processing 471 (1-2): 155-164 (2007)

4. Rodriguez, J., Rico, A., and Soria, V., "Tribological properties of commercial optical disks estimated from nanoindentation and scratch techniques," Wear 263: 1545-1550 (2007)

5. Huang, L., Lu, J., and Troyon, M., "Nanomechanical properties of nanostructured titanium prepared by SMAT," Surface & Coating Technology 201 (1-2): 208-213 (2006)

6. Beaker, B. D., and Lau, S. P., "Nanotribological and nanomechanical properties of 5-80 nm tetrahedral amorphous carbon films on silicon," Diamond and Related Materials 14 (9): 1535-1542 (2005)

7. Hodge, A. M., and Nieh, T. G., "Evaluating abrasive wear of amorphous alloys using nanoscratch technique," Intermetallics 12 (7-9): 741-748 (2004)

8. Wei, G., Weaver, M. L., and Barnard, J. A., "Nanotribological studies of chromium thin films," Tribology Letters 13 (4): 255-261 (2002)

9. Bhushan, B., "Nano- to microscale wear and mechanical characterization using scanning probe microscopy," Wear 250: 1105-1123 (2001)

10. Lawes, S. D. A., Fitzpatrick, M. E., and Hainsworth, S. V., "Evaluation of the tribological properties of DLC for engine application," Journal of Physics D – Applied Physics 40 (18): 5427-5437 (2007)

11. Bec, S., Tonck, A., and Fontaine, J., "Nanoindentation and nanofriction on DLC films," Philosophical Magazine 86 (33-35): 5465-5476 (2006)

12. McCook, N. L., Burris, D. L., Bourne, G. R., Steffens, J., Hanrahan, J. R., and Sawyer, W. G., "Wear resistant solid lubricant coating made from PTFE and epoxy", Tribology Letters 18 (1): 119-124 (2005)

13. Porada, O. K., Ivashenko, V. I., Ivashchenko, L. A., Rusakov, G., Dub, S. N., and Stegnij, A. I., "a-SiC: H films as perspective wear-resistant coatings," Surface & Coatings Technology 180: 122-126 (2004)

14. Ma, L. W., Cairney, J. M., Hoffman, M. J., and Munroe, P. R., "Characterization of TiN thin films subjected to nanoindentation using focused ion beam milling," Applied Surface Science 237 (1-4): 631-635 (2004)

15. Keulen, N. M., "Indentation creep of hydrated soda-lime silicate glass determined by nanoindentation," Journal of the American Ceramic Society 76 (4): 904-912 (1993)

16. Wang, F., and Xu, K. W., "An investigation of nanoindentation creep in polycrystalline Cu thin film," Materials Letters 58 (19): 2345-2349 (2004)

17. Cao, Z. Q., and Zhang, X., "Size-dependent creep behavior of plasma-enhanced chemical vapor deposited silicon oxide films," Journal of Physics D–Applied Physics 39 (23): 5054-5063 (2006)

18. Ye, D. Y., Matsuoka, S., and Nagashima, N., "Determination of fatigue mesoscopic mechanical properties of an austenitic stainless steel using depth-sensing indentation (DSI) technique," Materials Science and Engineering A–Structural Materials Properties Microstructure and Processing 456 (1-2): 120-129 (2007)

19. Xu, B. X., Wang, X. M., and Yue, Z. F., "Indentation behavior of polycrystalline copper under fatigue-peak overloading," Journal of Materials Research 22 (6): 1585-1592 (2007)

20. Matsuoka, S., and Nagashima, N., "Nano-meso-macro strength analysis of fine- and coarse-grain low-carbon steels subjected to low-cycle fatigue," Journal of the Japan Institute of Metals 70 (8): 700-708 (2006)

21. Liu, S. B., and Wang, Q., "A three-dimensional thermomechanical model of contact between non-conforming rough surfaces," Journal of Tribology 123 (1): 17-26 (2001)

22. Liu, G., Wang, Q., and Liu, S. B., "A Three-dimensional thermal-mechanical asperity contact model for two nominally flat surfaces in contact," Journal of Tribology 123 (3): 595-602 (2001)

23. Erdemir, A., "Review of engineered tribological interfaces for improved boundary lubrication," Tribology International 38: 249-256 (2005)

24. Etsion, I., "State of the art in laser surface texturing," Journal of Tribology 127 (1): 248-253 (2005)

25. Etsion, I., Kligerman, Y., and Halperin, G., "Analytical and experimental investigation of laser-textured mechanical sear faces," Tribology Transactions 42: 511-516 (1999)

26. Etsion, I., "Improving tribological performance of mechanical seals by laser surface texturing," Proceedings of the 17th International Pump Users Symposium, 17-22 (2000)

27. Pettersson, U., and Jacobson, S., "Friction and wear properties of micro textured DLC coated surfaces in boundary lubricated sliding," Tribology Letters, 17 (3): 553-559 (2004)

28. Suh, A. Y., Lee, S. –C., and Polycarpou, A. A., "Adhesion and friction evaluation of textured slider surfaces in ultra-low flying head-disk interfaces," Tribology Letters 17 (4): 739-749 (2004)

29. Pettersson, U., and Jacobson, S., "Influence of surface texture on boundary lubricated sliding contact," Tribology International 36: 857-864 (2003)

30. Nanbu, T., Yasuda, Y., Ushijima, K., Watanabe, J., and Zhu, D., "Increase of traction coefficient due to surface microtexture," Tribology Letters 29 (2): 105-118 (2008)

31. Pettersson, U., and Jacobson, S., "Textured surfaces for improved lubrication at high pressure and low sliding speed of roller/piston in hydraulic motors," Tribology International 40: 355-359 (2007)

32. Wakuda, M., Yamauchi, Y., Kanzaki, S., and Yasuda, Y., "Effect of surface texturing on friction reduction between ceramic and steel materials under lubricated sliding contact," Wear 254: 356-363 (2003)

33. Wang, Q., and Zhu, D., "Virtual texturing: modeling the performance of lubricated contacts of engineered surfaces," Journal of Tribology 127: 722-728 (2005)

34. Nosonvsky, M., and Bhushan, B., "Multiscale friction mechanisms and hierarchical surfaces in nano- and bio-tribology," Material Science & Engineering R-Reports 58 (3-5): 162-193 (2007)

35. Bowden, F. P., and Tabor, D., "The friction and lubrication of solids", Clarendon Press, Oxford (1986)

36. Zou, M., Cai, L., and Wang, H., "Adhesion and friction studies of a nano-textured surface produced by spin coating of colloidal silica nanoparticle solution," Tribology Letters 21 (1): 25-30 (2006)

37. Singh, R., Melkote, S. N., and Hashimoto, F., "Frictional response of precision finished surfaces in pure sliding," Wear 258 (10): 1500-1509 (2005)

38. Menezes, P. L., Kishore, and Kailas, S. V., "Effect of roughness parameter and grinding angle on coefficient of friction when sliding of Al-Mg alloy over EN8 steel," Journal of Tribology 128 (4): 697-704 (2006)

39. Hirano, M., Shinjo, K., Kaneko, R., and Murata, Y., "Anisotropy of friction forces in muscovite mica," Physical Review Letter 67: 2642-2645 (1991)

40. Sheehan, P. E., and Lieber, C. M., "Nanotribology and nanofabrication of MoO3 structures by atomic force microscopy," Science 272: 1158-1161 (1996)

41. He, G., Muser, M. H., and Robbins, M. O., "Adsorbed layers and the origin of static friction," Science 284: 1650-1652 (1999)

42. Ko, J. S., and Gellman, A. J., "Friction anisotropy at Ni(100)/Ni(100) interfaces," Langmuir 16 (22): 8343-8351 (2000)

43. Mancinelli, C. M., and Gellman, A. J., "Friction anisotropy at Pd(100)/Pd(100) interfaces," Langmuir 20 (5): 1680-1687 (2004)

44. Carpick, R. W., Sasaki, D. Y., and Burns, A. R., "Large friction anisotropy of a polydiacetylene monolayer," Tribology Letters 7: 79-85 (1999)

45. Carpick, R. W., and Eriksson, M. A., "Measurements of in-plane material properties with scanning probe microscopy," MRS Bulletin, 472-477 (2004)

46. Tilton, R. D., Roberston, C. R., and Gast, A. P., "Manipulation of hydrophobic interactions in protein adsorption," Langmuir 7 (171): 2710-2718 (1991)

47. Lee, J., and Kim, C. –J., "Surface tension driven microactuation based on continuous electrowetting," Journal of Microelectromechanical System 9 (2): 171-180 (2000)

48. Lee, J., Moon, H., Fowler, J., Kim, C. –J., and Schoellhammer, T., "Electrowetting on dielectric for microscale liquid handling," Sensors & Actuators A: Physical 95: 259-268 (2002)

49. Kim, J., and Kim, C. –J., "Nanostructured surfaces for dramatic reduction of flow resistance in droplet-based microfluidics," Proceedings of IEEE MEMS, 479-482 (2002)

50. McCarthy, J. T., and Oner, D., "Ultrahydrophobic surfaces. effects of topography length scales on wettability," Langmuir 16 (20): 7777-7782 (2000)

51. Wenzel, R. N., "Resistance of solid surfaces to wetting by water," Industrial and Engineering Chemistry 28: 988-994 (1936)

52. Cassie, A. B. D., and Baxter, S., "Wettability on porous surfaces," Transactions Faraday Society 40: 546-551 (1944)

53. Patankar, N. A., "On the modeling of hydrophobic contact angles on rough surfaces," Langmuir 19 (4): 1249-1253 (2003)

54. Barthlott, W., and Neinhuis, C., "Purity of the sacred lotus, or escape from contamination in biological surfaces," Planta 202: 1-8 (1997)

55. Lafuma, A., and Quéré, D., "Superhydrophobic states," Nature Materials, 2:457-460 (2003)

56. Miwa, M., Nakajima, A., Fujishima, A., Hashimoto, K., and Watanabe, T., "Effects of the surface roughness on sliding angles of water droplets on droplets on superhydrophobic surfaces," Langmuir 16 (13): 5754-5760 (2000)

57. Johnson, R. E., and Dettre, R. H., "Contact Angle Hysteresis I. Study of an Idealized Rough Surface," Advances in Chemistry Series, 43: 112-135 (1964)

58. Bico, J., Marzolin, C., and Quere, D., "Pearl drops," Europhysics Letters 47 (2): 220-226 (1999)

59. Togo, H., Sato, M., and Shimokawa, F., "Multi-element thermo-capillary optical switch and sub-nanometer oil injection for its fabrication," Proceedings of IEEE MEMS, 418-423 (1999)

60. Kogoh, S., Sakai, T., and Asami, K., "Temperature dependence of tensile-strength and hardness for nodular cast-iron and their mutual correlation," Journal of Materials Science 27 (16): 4323-4328 (1992)

61. Xia, J., Dong, H. S., and Bell, T., "Surface properties of a γ-based titanium aluminide at elevated temperatures," Intermetallics 10: 723-729 (2002)

62. Michel, M. D., Mikowski, A., Lepienski, C. M., Foerster, C. E., and Serbena, F. C., "High temperature microhardness of soda-lime glass," Journal of Non-crystalline Solid 348: 131-138 (2004)

63. Yonenaga, I., "Hardness, yield strength, and dislocation velocity in elemental and compound semiconductors," Materials Transactions 46 (9): 1979-1985 (2005)

64. Chwa, S. O., Klein, D., Liao, H. L., Dembinski, L., and Coddet, C., "Temperature dependence of microstructure and hardness of vacuum plasma sprayed Cu-Mo composite coatings," Surface & Coatings Technology 200 (20-21): 5682-5686 (2006)

65. Hutchison, M. M., and Louat, N., "Temperature dependence of yield strength in iron," Acta Metallurgica 10: 255-& (1962)

66. Weidner, D. J., Wang, Y. B., and Vaughan, M. T., "Yield strength at high-pressure and temperature," Geophysical Research Letters 21 (9): 753-756 (1994)

67. Peng, J. X., Jing, F. Q., Li, D. H., and Wang, L. L., "Pressure and temperature dependence of shear modulus and yield strength for aluminum, copper, and tungsten under shock compression," Journal of Applied Physics 98 (1): Art. No.013508 (2005)

68. Fisher-Cripps, A. C., "Nanoindentation," second edition, Springer, New York (1006)

69. Smith, J. F., and Zhang, S., "High temperature nanoscale mechanical property measurements," Surface Engineering 16 (2): 143-146 (2000)

70. Beaker, B. D., and Smith, J. F., "High-temperature nanoindentation testing of fused silica and other materials," Philosophical Magazine A 82 (10): 2179-2186 (2002)

71. Drobyshevski, E. M., Kolesnikova, E. N., and Yuferev, V. S., "Calculating the liquid film effect on solid armature rail-gun launching," IEEE Transactions on Magnetics 35 (1): 53-58 (1999)

72. Crawford, R., Taylor, J., and Keefer, D., "Solid ring armature experiments in a transaugmented railgun," IEEE Transactions on Magnetics 31 (1): 138-143 (1995)

73. Wu, J., and Pecht, M. G., "Contact resistance and fretting corrosion of lead-free alloy coated electrical contacts," IEEE Transactions on Components and Packaging Technologies 29 (2): 402-410 (2006)

74. Wable, G. S., Chu, Q. Y., Damodaran, P., and Srihari, K., "A systematic procedure for the selection of a lead-free solder paste in an electronics manufacturing environment," Soldering & Surface Mount Technology 17 (2): 32-39 (2005)

75. Suraski, D., and Seelig, K., "The current status of lead-free solder alloys," IEEE Transactions on Electronics Packaging Manufacturing 24 (4): 244-248 (2001)

76. Glavatskih, S. B., "Evaluating thermal performance of a PTFE-faced tilting pad thrust bearing," Journal of Tribology 125 (2): 319-324 (2003)

77. Lehmann, D., Hupfer, B., Lappan, U., Pompe, G., Haussler, L., Jehnichen, D., Janke, A., Geissler, U., Reinhardt, R., Lunkwitz, K., Franke, R., and Kunze, K., "New PTFE-polyamide compounds," Designed Monomers and Polymers 5 (2-3): 317-324 (2002)

78. Samyn, P., De, B. P., Schouken, G., and Van, P. A., "Large-scale tests on friction and wear of engineering polymers for material selection in highly loaded sliding systems," Materials & Design 27 (7): 535-555 (2006)

79. Kawachi, T., Takayanagi, S., Asakura, H., and Ishikawa, H., "Development of lead free overlay for three layer bearings of highly loaded engines," SAE Technical Papers, Document number: 2005-01-1863 (2005)

80. Okamoto, H., "Desk Handbook: Phase Diagram for Binary Alloys," ASM International (2000)

81. Greenwood, N. N., and Earnshaw, A., "Chemistry of the elements," 2nd Edition, Oxford: Butterworth-Heinemann (1997)

82. Hall, E. O., "The deformation and ageing of mild steel: III discussion of results," Proceedings of the Physical Society of London Section B 64: 747-753 (1951)

83. Petch, N. J., "The cleavage strength of polycrystals," Journal of The Iron and Steel Institute 174: 25 (1953)

84. Nix, W. D., and Gao, H., "Indentation size effect in crystalline materials: a law for strain gradient plasticity," Journal of the Mechanics and Physics of Solids 46 (3): 411-426 (1998)

85. Huang, Y., Xue, Z., Gao, H., Nix, W. D., Xia, Z. C., "A study of microindentation hardness tests by mechanism-based strain gradient plasticity," Journal of Materials Research 15 (8): 1786-1796 (2000)

86. Goddard, J., Wailman, H., "A theory of friction and wear during the abrasion of metals," Wear 5: 114-135 (1962)

87. Jr. Callister, W. D., "Materials science and engineering: an introduction," Wiley, 6th edition (2002)

88. Zou, M., Cai, L., and Yang, D., "Nanotribology of a silica nanoparticle-textured surface," Tribology Transactions 49 (1), 66-71 (2006)

89. Wakuda, M., Yamauchi, Y., Kanzaki, S., and Yasuda, Y., "Effect of surface texturing on friction reduction on ceramics and steel materials under lubricated sliding contact," Wear 254: 356-363 (2003)

90. Bulatov, V. P., Krasny, V. A., and Schneider, Y. G., "Basis of machining methods to yield wear- and fretting-resistive surfaces, having regular roughness patterns," Wear 208:132-137 (1997)

91. Jackman, R., Wilbur, J., and Whitesides, G. M., "Fabrication of submicron features on curved substrates by microcontact printing," Science 269: 664-666 (1995)

92. Zhao, X. –M., Stoddart, A., Smith, S. P., Kim, E., Xia, Y., Prentiss, M., and Whitesides, G. M., "Fabrication of single-mode polymeric waveguides using micromolding in capillaries," Advanced Materials 8: 420-424 (1996)

93. Lee, J., He, B., and Patankar, N. A., "A roughness based wettability switching membrane device for hydrophobic surface," Journal of Micromechanics and Microengineering 15: 591-600 (2005)

94. Madou, M. J., "Fundamentals of Microfabrication," CRC Press:, Chapter 1 (1997)

95. Johnson, K. L., Kendall, K., and Roberts, A. B., "Surface energy and the contact of elastic solids," Proceedings of the Royal Society London. Series A, Mathematical and Physical Sciences 324 (1558): 301-313 (1971)

96. Derjaguin, B. V., Muller, V. M., and Toporov, Y. P., "Effect of contact deformations on the adhesion of particles," Journal of Colloid and Interface Science 67: 314-326 (1975)

97. Tabor, D., "Surface forces and surface interactions," Journal of Colloid and Interface Science 58: 1-13 (1976)

98. Chin, P., McCullough, R. L., and Wu, W. L., "An improved procedure for determining the work of adhesion for polymer-solid contact," Journal of Adhesion 64: 145-160 (1997)

99. Lotters, J. C., Olthuis, W., Veltink, P. H., and Bergveld, P., "The mechanical properties of the rubber elastic polymer polydimethylsiloxane for sensor applications," Journal of Micromechanics and Microengineering 7:145-147 (1997)

100. Armani, D., and Liu, C., "Re-configurable fluid circuits by PDMS elastomer micromachining," 12th International Conference on MEMS, 222-227 (1998)

101. Bistac, S., and Galliano, A., "Nano and macro tribology of elastomers," Tribology Letters 18 (1): 21-25 (2005)

102. Elzein, T., Galliano, A., and Bistac, S., "Chains anisotropy in PDMS networks due to friction on gold surfaces," Journal of Polymer Science Part B: Polymer Physics 42 (12): 2348-2353 (2004)

103. Yoshizawa, H., and Israelachvili, J. N., "Relation between adhesion and friction forces across thin films," Thin Solid Films 246: 71-76 (1994)

104. Heuberger, M., Luengo, G., Israelachvili, J. N., "Tribology of shearing polymer surfaces. 1. Mica sliding on polymer (PnBMA)," Journal of Physical Chemistry B 103 (46): 10127-10135 (1999)

105. Moseler, M., Gumbsch, P., Casiraghi, C., Ferrari, A. C., and Robertson, J., "The ultrasmoothness of diamond-like carbon surfaces," Science 309 (2), 1545-1548 (2005)

106. Gao, G., Cannara, R. J., Carpick, R. W., and Harrison, J. A., "Atomic-scale friction on diamond: a comparison of different sliding directions on (001) and (111) surfaces using MD and AFM," Langmuir 23 (10), 5394-5405 (2007)

107. Chen, W. W., and Wang, Q., "A numerical static friction model for spherical contacts of rough surfaces, influence of load, material, and roughness," Journal of Tribology, under review

108. Patankar, N. A., "Mimicking the superhydrophobicity of Lotus leaves," Langmuir 20 (19): 8209-8213 (2004)

109. Lee, J., He, B., and Patankar, N. A., "A roughness-based wettability switching membrane device for hydrophobic surfaces," Journal of Micromechanics and Microengineering 15: 591-600 (2005)

110. Adamson, A. W., "Physical Chemistry of Surfaces," 6th edition, John Wiley & Sons: New York, Chapter X, Section 5 (1997)

111. Marmur, A., "Wetting on hydrophobic rough surfaces: to be heterogeneous or not to be," Langmuir 19 (20): 8343-8348 (2003)

112. McMahon, T. A., and Bonner, J. T., "On Size and Life," Scientific American Books, New York (1983)

113. Patankar, N. A., "Transition between superhydrophobic states on rough surfaces," Langmuir 20: 7097-7102 (2004)

114. Reyssat, M., Yeomans, J. M., and Quéré, D., "Impalement of fakir drops," European Physics Letter 81: 26006 (2008)

115. Onda, T., Shibuichi, S., Satoh, N., and Tsujii, K., "Super-water-repellent fractal surfaces," Langmuir 12 (9): 2125-2127 (1996)

116. Shibuichi, S., Onda, T., Satoh, N., and Tsujii, K., "Super water-repellent surfaces resulting from fractal structure," Journal Physical Chemistry 100: 19512-19517 (1996)

117. He, B., Patankar, N. A., and Lee, J., "Multiple equilibrium droplet shapes and design criterion for rough hydrophobic surfaces," Langmuir 19 (12): 4999-5003 (2003)

118. He, B., Lee, J., and Patankar, N. A., "Contact angle hysteresis on rough hydrophobic surfaces," Colloid and Surface A: Physicochemical and Engineering Aspects 248: 101-104 (2004)

119. Dettre, R. H., and Johnson, R. E., "Contact angle hysteresis. II. contact angle measurements on rough surfaces," Advanced Chemistry Series, 43: 136-157 (1964)

120. Gau, H., Herminghaus, S., Lenz, P., and Lipowsky, R., "Liquid morphologies on structured surfaces: from microchannels to microchips," Science 283: 46-49 (1999)

121. Chen, Y., He, B., Patankar, N. A., and Lee, J., "Anisotropy in the wetting of rough surfaces," Journal of Colloid & Interface Science 281: 458-464 (2004)

122. Brakke, K. A., "The surface evolver," Experimental Mathematics 1: 141-165 (1992)

123. Brandon, S., Haimovich, N., Yeger, E., and Maumur, A., "Partial wetting of chemically patterned surfaces: the effect of drop size," Journal of Colloid and Interface Science 263 (1): 237-243 (2003)

124. Finn, R., "Equilibrium Capillary Surfaces," Springer-Verlag, 4-10 (1986)

125. Oliver, J. F., Huh, D., Mason, S. G., "Resistance to spreading of liquids by sharp edges," Journal of Colloid and Interface Science 59 (3): 568-581 (1977)

126. Wolanski G., and Marmur A., "Apparent contact angles on rough surfaces: the Wenzel equation revisited," Colloids and Surfaces A: Physicochemical and Engineering Aspects 156: 381-388 (1999)

127. Yoshimitsu, Z., Nakajima, A., Watanabe, T., and Hashimoto, K., "Effect of surface structure on the hydrophobicity and sliding behavior of water droplets," Langmuir 18: 5818-5822 (2002)

128. Oosterbroek, E., van den Berg, A., "Lab-on-a-chip: miniaturized systems for (bio)chemical analysis and synthesis," Elsevier Science, 2nd edition (2003)

129. Jo, B.-H., Van Lerberghe, L. M., Motsegood, K. M., and Beebe, D. J., "Three-dimensional micro-channel fabrication in Polydimethylsiloxane (PDMS) elastomer," Journal of Microelectromechanical Systems 9 (1): 76-81 (2000)

130. Khoo, M., and Liu, C., "Micro magnetic silicone elastomer membrane actuator," Sensor and Actuators, Physics A 89 (3): 259-266 (2001)

VITA

July 30, 1976	Born in Tianjin, P. R. China
1999	Bachelor of Engineering, Department of Precision Instrument and Mechanology, Tsinghua University, Beijing, P. R. China
2001	Master of Science, Department of Mechanical and Aerospace Engineering, University of Missouri-Columbia, Columbia, USA
2008	Doctor of Philosophy, Department of Mechanical Engineering, Northwestern University, Evanston, USA

JOURNAL PUBLICATIONS

He, B., Chung, Y. W., Ghosh, G., and Wang, Q., "Effect of surface melting on the nano/micro scale friction of Ag-Bi alloys," in preparation

He, B., Chen, W. W., and Wang, Q., "Surface texture effect on friction of a Microtextured Poly(dimethylsiloxane) (PDMS)," to appear in Tribology Letters

Lee, J., **He, B**., and Patankar, N. A., "A roughness based wettability switching membrane device for hydrophobic surfaces," Journal of Micromechanics & Microengineering 15, 591-600 (2005)

He, B., Patankar, N. A., and Lee, J., "Contact angles hysteresis on rough hydrophobic surfaces," Colloid & Surfaces A: Physicochemical & Engineering Aspects 248, 101-104 (2004)

Chen, Y., **He, B**., and Patankar, N. A., "Anisotropy in the wetting of rough surfaces," Journal of Colloid & Interface Science 281, 458-464 (2005)

He, B., Patankar, N. A., and Lee, J., "Multiple equilibrium shapes of droplets and design criterion for rough hydrophobic surfaces," Langmuir 19(12), 4999-5003 (2003)

Feng, Z., **He, B**., and Lombardo, S. J., "Stress distribution in porous ceramic bodies during binder burnout," Journal of Applied Mechanics 69, 497-501 (2002)

CONFERENCE PROCEEDINGS AND PRESENTATIONS

He, B., Chung, Y. W., Ghosh, G., and Wang, Q., "Effect of surface melting on the nano/micro scale friction of Ag-Bi alloys," STLE Annual Meeting, Cleveland, USA (2008)

He, B., Chen, W. W., and Wang, Q., "Friction and wettability of a micro-textured elastomer: Poly(dimethylsiloxane) (PDMS)," STLE/ASME International Joint Tribology Conference, San Antonio, TX, USA (2006)

He, B., and Wang, Q., "Study of high temperature friction and the effect of melting," Golden Research Conference on Tribology, Waterville, ME, USA (2006)

He, B., Chung, Y. W., and Wang, Q., "Study of small-scale friction at elevated Temperatures," World Tribology Congress III, Washington, D.C., USA (2005)

Chung, Y. W., **He, B**., and Wang, Q., "Simulation of tribological phenomena: modeling of scuffing Failure," World Congress on Computational Mechanics IV, Beijing, China (2004)

He, B., and Lee, J., "Bistable nature of the hydrophobic contact angle on rough surfaces," Proceeding of ASME MEMS (2003)

He, B., and Lee, J., "Dynamic wettability switching by surface roughness effect," Proceeding of IEEE MEMS, 120-123 (2003)

HONORS AND AWARDS

Society of Tribology and Lubrication Engineering Annual Scholarship, Chicago Section, 2006
Smith Terminal Year Fellowship, Northwestern University, 2006
Graduate Research Assistantship, Northwestern University, 2001-2006
Graduate Teaching Assistantship, Northwestern University, 2003, 2004, 2006
Graduate Research Assistantship, University of Missouri-Columbia, 2000-2001

ACADEMIC SERVICES

Session Vice Chair, Nanotribology, STLE/ASME International Joint Tribology Conference, October 23-25, 2006, San Antonio, Texas, USA
Technical Paper Reviewer, 7th World Congress on Computational Mechanics, 2006, Los Angeles, CA, USA
Session Vice Chair, Surface Engineering Session I, STLE Annual Meeting 2006, Calgary, Alberta, Canada
Vice Paper Soliciting Chair, Surface Engineering Technical Committee of Society of Tribologists and Lubrication Engineering (STLE), 2005
Technical Paper Reviewer, ASME Journal of Tribology, 2005
Technical Paper Reviewer, Wear of Material, 2004
Member of Organization Committee of Student Poster Program in World Tribology Congress III 2005
Student Poster Paper Reviewer, World Tribology Congress III, 2005
Facility Manager, Center for Surface Engineering and Tribology (CSET), 2003-present
Student Assistant and Attendee of the 2004-2005 NSF Summer Institute on Nano Mechanics and Materials, Northwestern University, 2005
Student Coordinator, Northwestern University, Mechanical Engineering Graduate Student Society (MEGSS), 2004
MEGSS team member on new ME graduate student recruitment

PROFESSIONAL SOCIETY AFFILIATIONS

American Society of Mechanical Engineers (ASME)
Institute of Electrical and Electronics Engineers (IEEE)
Society of Tribologists and Lubrication Engineers (STLE)
Materials Research Society (MRS)
Society of Photo-Optical Instrumentation Engineers (SPIE)